



NAVAL POSTGRADUATE SCHOOL

MONTEREY, CALIFORNIA

THESIS

**CLIMATE ANALYSIS AND LONG RANGE FORECASTING
OF RADAR PERFORMANCE IN THE WESTERN NORTH
PACIFIC**

by

David Ramsaur

June 2009

Thesis Co-Advisors:

Tom Murphree
Paul A. Frederickson

Approved for public release; distribution is unlimited

THIS PAGE INTENTIONALLY LEFT BLANK

REPORT DOCUMENTATION PAGE			<i>Form Approved OMB No. 0704-0188</i>	
Public reporting burden for this collection of information is estimated to average 1 hour per response, including the time for reviewing instruction, searching existing data sources, gathering and maintaining the data needed, and completing and reviewing the collection of information. Send comments regarding this burden estimate or any other aspect of this collection of information, including suggestions for reducing this burden, to Washington headquarters Services, Directorate for Information Operations and Reports, 1215 Jefferson Davis Highway, Suite 1204, Arlington, VA 22202-4302, and to the Office of Management and Budget, Paperwork Reduction Project (0704-0188) Washington DC 20503.				
1. AGENCY USE ONLY (Leave blank)		2. REPORT DATE June 2009	3. REPORT TYPE AND DATES COVERED Master's Thesis	
4. TITLE AND SUBTITLE Climate Analysis and Long Range Forecasting of Radar Performance in the Western North Pacific			5. FUNDING NUMBERS	
6. AUTHOR(S) David C. Ramsaur				
7. PERFORMING ORGANIZATION NAME(S) AND ADDRESS(ES) Naval Postgraduate School Monterey, CA 93943-5000			8. PERFORMING ORGANIZATION REPORT NUMBER	
9. SPONSORING /MONITORING AGENCY NAME(S) AND ADDRESS(ES) N/A			10. SPONSORING/MONITORING AGENCY REPORT NUMBER	
11. SUPPLEMENTARY NOTES The views expressed in this thesis are those of the author and do not reflect the official policy or position of the Department of Defense or the U.S. Government.				
12a. DISTRIBUTION / AVAILABILITY STATEMENT Approved for public release; distribution is unlimited			12b. DISTRIBUTION CODE	
13. ABSTRACT (maximum 200 words) <p>The ability to predict the evaporation duct has important applications for naval activities, such as electronic counter-measures, surveillance, communications, and radar detection and tracking of submarine periscopes, low-flying missiles, aircraft, and surface combatants. This study addresses two major research questions:</p> <ol style="list-style-type: none"> 1. Can state-of-the-science data sets, models, and methods be used to create more accurate and useful climatologies of atmospheric radar propagation? 2. Can skillful long range forecasts (LRFs) of evaporation duct heights and radar detection ranges be developed for mission planning purposes? <p>To answer these questions, we applied modern climate data sets and methods to investigate climate scale variations in evaporation duct height (EDH) and radar detection range (RDR) in the western North Pacific (WNP). We also conducted multi-decadal hindcasts of winds, EDH, and RDR in the WNP to assess the potential for producing skillful LRFs of these variables. We identified significant variations that have the potential to be predicted at leads times of one to four months. Climate scale analyses of these and similar variations have the potential to significantly improve electromagnetic (EM) propagation climatologies by providing a more complete description of the range of possible environmental conditions for which military planners need to prepare. LRFs of these and similar variations have the potential to provide planners with predictions of which variation is most probable for a given time and location. The combination of such climate analyses and LRFs can provide environmental guidance, for example, guidance for use in planning antisubmarine warfare operators in the WNP.</p>				
14. SUBJECT TERMS Climatology, Smart Climatology, Evaporation Duct Height, Radar Detection Ranges, Western North Pacific, East China Sea, Radar Propagation, Sensor Performance, Performance Surface, Climate Variations, U. S. Navy, El Nino, La Nina, NPS ED Model, AREPS			15. NUMBER OF PAGES 115	
			16. PRICE CODE	
17. SECURITY CLASSIFICATION OF REPORT Unclassified	18. SECURITY CLASSIFICATION OF THIS PAGE Unclassified	19. SECURITY CLASSIFICATION OF ABSTRACT Unclassified	20. LIMITATION OF ABSTRACT UU	

NSN 7540-01-280-5500

Standard Form 298 (Rev. 2-89)
Prescribed by ANSI Std. Z39-18

THIS PAGE INTENTIONALLY LEFT BLANK

Approved for public release; distribution is unlimited

**CLIMATE ANALYSIS AND LONG RANGE FORECASTING OF RADAR
PERFORMANCE IN THE WESTERN NORTH PACIFIC**

David C. Ramsaur
Civilian, United States Navy
B.S., University of North Carolina at Asheville, 2008

Submitted in partial fulfillment of the
requirements for the degree of

MASTER OF SCIENCE IN METEOROLOGY

from the

**NAVAL POSTGRADUATE SCHOOL
June 2009**

Author: David C. Ramsaur

Approved by: Dr. Tom Murphree
Co-Advisor

Mr. Paul A. Frederickson
Co-Advisor

Dr. Philip A. Durkee
Chairman, Department of Meteorology

THIS PAGE INTENTIONALLY LEFT BLANK

ABSTRACT

The ability to predict the evaporation duct has important applications for naval activities, such as electronic counter-measures, surveillance, communications, and radar detection and tracking of submarine periscopes, low-flying missiles, aircraft, and surface combatants. This study addresses two major research questions:

1. Can state-of-the-science data sets, models, and methods be used to create more accurate and useful climatologies of atmospheric radar propagation?
2. Can skillful long range forecasts (LRFs) of evaporation duct heights and radar detection ranges be developed for mission planning purposes?

To answer these questions, we applied modern climate data sets and methods to investigate climate scale variations in evaporation duct height (EDH) and radar detection range (RDR) in the western North Pacific (WNP). We also conducted multi-decadal hindcasts of winds, EDH, and RDR in the WNP to assess the potential for producing skillful LRFs of these variables. We identified significant variations that have the potential to be predicted at leads times of one to four months. Climate scale analyses of these and similar variations have the potential to significantly improve electromagnetic (EM) propagation climatologies by providing a more complete description of the range of possible environmental conditions for which military planners need to prepare. LRFs of these and similar variations have the potential to provide planners with predictions of which variation is most probable for a given time and location. The combination of such climate analyses and LRFs can provide environmental guidance, for example, guidance for use in planning antisubmarine warfare operators in the WNP.

THIS PAGE INTENTIONALLY LEFT BLANK

TABLE OF CONTENTS

I.	INTRODUCTION.....	1
A.	MOTIVATION.....	1
B.	DEFINITIONS.....	2
	1. Smart Climatology	2
	2. Traditional Climatology	3
	3. Smart Climatology Processes	3
	4. Smart Climatology Elements and Gaps in Military Support.....	4
	5. Smart Climatology and Battlespace on Demand (BonD)	5
C.	RADAR TACTICAL DECISION AIDS.....	7
	1. Definitions	7
	a. <i>Propagation Loss</i>	7
	b. <i>Radar Detection Range</i>	7
	2. Use of Climatology in Tactical Decision Aids	8
	a. <i>Traditional Climatology</i>	8
	b. <i>State-of-the-Science Atmospheric Reanalysis</i>	8
	3. Naval Postgraduate School Bulk Model	9
	4. Advanced Propagation Model	11
	5. Advanced Refractive Effects Prediction System	12
D.	REFRACTION, DUCTING, AND RADAR DETECTION RANGES	12
	1. Modified Refractivity and Ducting Layers	13
	2. Environmental Factors Affecting the Evaporation Duct.....	15
	3. Electromagnetic Propagation and Detection Ranges	16
	4. Current Radar Detection Range Products	16
E.	OVERVIEW OF THIS STUDY	17
II.	DATA AND METHODS.....	19
A.	DATA	19
B.	METHODS	21
	1. Evaporation Duct Height and Radar Detection Range Calculations	21
	2. Climate Analyses	22
	3. Forecasting	24
	4. Verification Metrics.....	26
	a. <i>Contingency Tables</i>	26
	b. <i>Percent Correct</i>	26
	c. <i>Probability of Detection</i>	27
	d. <i>False Alarm Rate</i>	27
	e. <i>Threat Score</i>	27
	f. <i>Heidke Skill Score</i>	28
C.	SUMMARY	28
III.	RESULTS	29

A.	LONG TERM MEAN SEASONAL CYCLES: LARGE SCALE FEATURES AND PROCESSES	29
1.	Winter	29
2.	Spring	33
3.	Summer	36
4.	Fall	38
B.	LONG TERM MEAN SEASONAL CYCLES: EDH AND FACTORS THAT DETERMINE EDH	41
1.	January	41
2.	April	44
3.	July	46
4.	October	48
C.	LONG TERM MEAN SEASONAL CYCLES: RADAR DETECTION RANGES	51
D.	OCTOBER CONDITIONAL COMPOSITES.....	54
1.	Conditional Composites Based on Winds.....	54
E.	DEVELOPMENT OF LONG RANGE FORECAST PROCESS.....	58
F.	HINDCASTS AND HINDCAST VERIFICATION METRICS	64
G.	SMART CLIMATOLOGY VERSUS TRADITIONAL U. S. MILITARY CLIMATOLOGY	67
H.	LONG RANGE FORECASTS OF EDH AND RDR	70
IV.	SUMMARY, CONCLUSIONS, AND RECOMMENDATIONS	71
A.	SUMMARY AND CONCLUSIONS.....	71
B.	RECOMMENDATIONS FOR FUTURE RESEARCH	72
	APPENDIX	75
	LIST OF REFERENCES.....	89
	INITIAL DISTRIBUTION LIST	93

LIST OF FIGURES

Figure 1	Evaporation duct height (EDH, in m) for September from: (a) NPS smart EDH climatology and (b) existing Navy climatology. NPS smart climatology developed from existing civilian multi-decadal atmospheric and oceanic reanalysis data sets. From Twigg (2007)....	2
Figure 2.	The smart climatology process. From LaJoie (2006).....	4
Figure 3.	A comparison of the status of routine, readily available, operational climate support from operational civilian and military centers.in terms of the seven major elements of climate support. From Murphree (2008a).....	5
Figure 4.	Schematic depiction of the Battlespace on Demand (BonD) including descriptions of smart climatology support products for each of the four BonD tiers. From Murphree (2008a).....	6
Figure 5.	Sea surface temperature (SST; C°) in the East China Sea for July - September of 1968-2006. Traditional climatology describes the long term mean SST and related quantities (e.g., the long term mean high and low SST) shown by the solid and dashed blue lines. But traditional climatology does not describe interannual variations (identified by red ovals), long term trends (identified by red line), and other deviations from long trm mean conditions.	9
Figure 6.	Comparison of the propagation loss (dB) for a 19 day period in 2001 as determined by measurements (red), NPS model (blue), P-J model (green), standard atmosphere, (brown) and free space measurements (black). From Frederickson (2008).....	10
Figure 7.	Plots of modified refractivity (M) versus altitude: (a) sub-refractive layer denoted by dashed line; (b) normal refraction; (c) elevated duct denoted by dashed line; (d) surface duct denoted by dashed line; (e) surface-based duct denoted by dashed line, (due to an elevated layer with a strongly negative vertical M gradient); (f) evaporation duct denoted by dashed line. From: Babin et al. (1997).....	14
Figure 8.	A vertical M profile for a surface duct and its associated height versus range ray trace plot of X-band waves emitted from an antenna at 25 m height propagating through an atmosphere with an EDH of 20 m. From Frederickson et al. (2000).....	15
Figure 9.	Western North Pacific study region. The red box encompassing 20-28°N and 122-126°E was a focus area for developing our long range forecasting methods.	18
Figure 10.	Western North Pacific study area with mesh showing locations of reanalysis data grid points used in our calculations of evaporation duct heights and radar detection ranges.	20
Figure 11.	Summary of the long range forecasting process developed and applied in our study.	25

Figure 12.	Two by two contingency table used in our study to categorize and assess our hindcast and forecast results.....	26
Figure 13.	January LTM air temperature (°C) at 1000 hPa. Relatively cool (warm) air can be seen over the northern (southern portion) of the WNP AOI (boxed region) for this study. The cool air is associated with the southward outflow of cold dry air along the eastern flank of the Siberian high (see Figures 14-15). Basic figure created at ESRL web site (http://www.cdc.noaa.gov , accessed May 2009).	30
Figure 14.	January LTM 1000 hPa geopotential height (m). The WNP AOI (boxed region) for our study occurs on the eastern flank of the Asian High (H) and near the western flank of the Aleutian Low (L) and North Pacific High (centered between Hawaii and California). Climate scale variations in these three height centers can lead to variations in the WNP AOI. Basic figure created at ESRL web site (http://www.cdc.noaa.gov , accessed May 2009).	31
Figure 15.	January LTM 850 hPa vector wind (m/s). The northern (southern) portion of the WNP AOI (boxed region) for our study experiences predominantly southward (westward) low level winds. Northerly winds can be seen over the Korean peninsula as a result of the tightened gradient between the Siberian high and the Aleutian low while warm moist air is coming from the easterlies. Basic figure created at ESRL web site (http://www.cdc.noaa.gov , accessed May 2009).	32
Figure 16.	January LTM sea surface temperature (SST; °C). The northern (southern) portion of the WNP AOI (boxed region) for our study experiences relatively warm (cool) SSTs, with strong SST gradients near the Korean peninsula. Basic figure created at ESRL web site (http://www.cdc.noaa.gov , accessed May 2009).	33
Figure 17.	April LTM air temperature (°C) at 1000 hPa. When compared to January, April air temperature is greater over the entire WNP AOI (boxed region), with the largest change being over the Sea of Japan and the northern portion of the East China Sea. Basic figure created at ESRL web site (http://www.cdc.noaa.gov , accessed May 2009).	34
Figure 18.	April LTM 1000 hPa geopotential height (m). Winter to spring changes in the WNP AOI (boxed region) are strongly influenced by the weakening of the Asian High and the strengthening of the North Pacific High from January to April. Basic figure created at ESRL web site (http://www.cdc.noaa.gov , accessed May 2009).	34
Figure 19.	April LTM 850 hPa vector wind (m/s). Note the shift from predominantly northerly winds over much of the WNP AOI (boxed region) in January to westerly and southerly winds in April. Basic figure created at ESRL web site (http://www.cdc.noaa.gov , accessed May 2009).	35

Figure 20.	April LTM sea surface temperature (SST; °C). Note the increase in SSTs throughout the entire WNP AOI (boxed region) from January to April. Basic figure created at ESRL web site (http://www.cdc.noaa.gov , accessed May 2009).	35
Figure 21.	July LTM air temperature (°C) at 1000 hPa. The WNP AOI (boxed region) is dominated by warm, moist air and weaker temperature gradients than in January and April. Basic figure created at ESRL web site (http://www.cdc.noaa.gov , accessed May 2009).	36
Figure 22.	July LTM 1000 hPa geopotential height (m). The dominant geopotential height patterns for the WNP AOI (boxed region) are the Asian Low and North Pacific High which cause mainly southerly flow over most of the AOI. Basic figure created at ESRL web site (http://www.cdc.noaa.gov , accessed May 2009).	37
Figure 23.	July LTM 850 hPa vector wind (m/s). Winds are predominantly southerly over most of the WNP AOI (boxed region) consistent with advection of warm, moist air into the AOI from the tropics. LTM wind speeds in the AOI during summer tend to be weaker than in the other seasons. Basic figure created at ESRL web site (http://www.cdc.noaa.gov , accessed May 2009).	37
Figure 24.	July LTM sea surface temperature (SST; °C). SSTs in the WNP AOI (boxed region) during summer are warmer and warmer than in the other seasons. Basic figure created at ESRL web site (http://www.cdc.noaa.gov , accessed May 2009).	38
Figure 25.	October LTM air temperature (°C) at 1000 hPa. Cool low level air temperatures and SSTs develop during fall over East Asia and most of the WNP AOI (boxed region). Basic figure created at ESRL web site (http://www.cdc.noaa.gov , accessed May 2009).	39
Figure 26.	October LTM 1000 hPa geopotential height (m). During fall, the WNP AOI (boxed region) is strongly affected by the development of the Asian High, the southward shift and strengthening of the Aleutian Low, and the weakening and eastward shift of the North Pacific High. Basic figure created at ESRL web site (http://www.cdc.noaa.gov , accessed May 2009).	39
Figure 27.	October LTM 850 hPa vector wind (m/s). In fall, the northern (southern) portion of the WNP AOI (boxed region) is doimnated by northerly (easterly) low level winds. Basic figure created at ESRL web site (http://www.cdc.noaa.gov , accessed May 2009).	40
Figure 28.	October LTM sea surface temperature (SST; °C). In fall, SSTs over most of the WNP AOI (boxed region) transition from warm summer conditions to cool winter conditions. Basic figure created at ESRL web site (http://www.cdc.noaa.gov , accessed May 2009).	40
Figure 29.	January LTM EDH (m) for the WNP AOI.	42
Figure 30.	January LTM wind speed (m/s) at 10 meters for WNP AOI.	42
Figure 31.	January LTM air-sea temperature difference (°C) for WNP AOI.	43
Figure 32.	January LTM relative humidity (%) at 2 meters for WNP AOI.	43

Figure 33.	April LTM EDH (m) for the WNP AOI.....	44
Figure 34.	April LTM wind speed (m/s) at 10 meters for WNP AOI.	45
Figure 35.	April LTM air-sea temperature difference (°C) for WNP AOI.	45
Figure 36.	April LTM relative humidity (%) at 2 meters for WNP AOI.	46
Figure 37.	July LTM EDH (m) for the WNP AOI.	47
Figure 38.	July LTM wind speed (m/s) at 10 meters for WNP AOI.	47
Figure 39.	July LTM air-sea temperature difference (°C) for WNP AOI.	48
Figure 40.	July LTM relative humidity (%) at 2 meters for WNP AOI.	48
Figure 41.	October LTM EDH (m) for the WNP AOI.	49
Figure 42.	October LTM wind speed (m/s) at 10 meters for WNP AOI.	50
Figure 43.	October LTM air-sea temperature difference (°C) for WNP AOI.	50
Figure 44.	October LTM relative humidity (%) at 2 meters for WNP AOI.	51
Figure 45.	January LTM RDR (nmi) for WNP AOI.	52
Figure 46.	April LTM RDR (nmi) for WNP AOI.	53
Figure 47.	July LTM RDR (nmi) for WNP AOI.	53
Figure 48.	October LTM RDR (nmi) for WNP AOI.	54
Figure 49.	October conditional composite of surface winds for the five years with the highest meridional wind speeds averaged over 20-28°N, 123-128°E (area east of Taiwan shown in Figure 9). From Turek (2008).	56
Figure 50.	October conditional composite of surface winds for the five years with the lowest meridional wind speeds averaged over 20-28°N, 123-128°E (area east of Taiwan shown in Figure 9). From Turek (2008).	56
Figure 51.	October conditional composite anomaly of surface winds for the five years with the highest meridional wind speeds averaged over 20-28°N, 123-128°E (area east of Taiwan shown in Figure 9). From Turek (2008).	57
Figure 52.	October conditional composite anomaly of surface winds for the five years with the lowest meridional wind speeds averaged over 20-28°N, 123-128°E (area east of Taiwan shown in Figure 9). From Turek (2008).	57
Figure 53.	Correlation of October radar detection range (RDR) in the focus region east of Taiwan (purple box) with SST in October for the years 1970-2006. The RDR is for a 9 GHz radar at 85 ft above the surface, looking for a 4 ft target with a detection threshold of 150 dB. The red box highlights a region of persistently high correlations when SST leads October RDR by zero to five months (see Figures 55-59). Basic figure created at ESRL web site (http://www.cdc.noaa.gov , accessed May 2009).	60
Figure 54.	Correlation of October radar detection range (RDR) in the focus region east of Taiwan (purple box) with SST in September for the years 1970-2006. The RDR is for a 9 GHz radar at 85 ft above the surface, looking for a 4 ft target with a detection threshold of 150 dB. The red box highlights a region of persistently high correlations	

	when SST leads October RDR by zero to five months (see Figures 55-59). Basic figure created at ESRL web site (http://www.cdc.noaa.gov , accessed May 2009).	61
Figure 55.	Correlation of October radar detection range (RDR) in the focus region east of Taiwan (purple box) with SST in August for the years 1970-2006. The RDR is for a 9 GHz radar at 85 ft above the surface, looking for a 4 ft target with a detection threshold of 150 dB. The red box highlights a region of persistently high correlations when SST leads October RDR by zero to five months (see Figures 55-59). Basic figure created at ESRL web site (http://www.cdc.noaa.gov , accessed May 2009).	62
Figure 56.	Correlation of October radar detection range (RDR) in the focus region east of Taiwan (purple box) with SST in July for the years 1970-2006. The RDR is for a 9 GHz radar at 85 ft above the surface, looking for a 4 ft target with a detection threshold of 150 dB. The red box highlights a region of persistently high correlations when SST leads October RDR by zero to five months (see Figures 55-59). Basic figure created at ESRL web site (http://www.cdc.noaa.gov , accessed May 2009).	63
Figure 57.	Correlation of October radar detection range (RDR) in the focus region east of Taiwan (purple box) with SST in June for the years 1970-2006. The RDR is for a 9 GHz radar at 85 ft above the surface, looking for a 4 ft target with a detection threshold of 150 dB. The red box highlights a region of persistently high correlations when SST leads October RDR by zero to five months (see Figures 55-59). Basic figure created at ESRL web site (http://www.cdc.noaa.gov , accessed May 2009).	64
Figure 58.	Verification metrics for hindcasts for 1970-2006 of above normal (i.e., high) meridonal wind in October in the WNP focus region using eqatorial SST near the dateline in October, September, August, July, and June as the predictor. The hindcast methods, and the metrics and metrics legend acronyms are explained in Chapter II, section B. See text for additonal details.	65
Figure 59.	Verification metrics for hindcasts for 1970-2006 of above normal (i.e., high) EDH in October in the WNP focus region using eqatorial SST near the dateline in October, September, August, July, and June as the predictor. The hindcast methods, and the metrics and metrics legend acronyms are explained in Chapter II, section B. See text for additonal details.	66
Figure 60.	Verification metrics for hindcasts for 1970-2006 of near normal RDR in October in the WNP focus region using eqatorial SST near the dateline in October, September, August, July, and June as the predictor. The hindcast methods, and the metrics and metrics legend acronyms are explained in Chapter II, section B. See text for additonal details.	66

Figure 61.	October LTM evaporation duct height (EDH) example of the present U. S. Navy LTM EDH climatology in tabular format.	68
Figure 62.	October LTM evaporation duct height (EDH) example of the present U. S. Navy LTM EDH climatology, after we manually entered and then plotted the data shown in Figure 61.....	69
Figure 63.	October LTM evaporation duct height (EDH) example of applying modern climate data sets and methods to develop a state-of-the-science EDH climatology. Note the large differences between this modern EDH climatology and the present Navy climatology (Figure 61-62).....	69
Figure 64.	February LTM EDH (m) for the WNP AOI.	75
Figure 65.	March LTM EDH (m) for the WNP AOI.....	75
Figure 66.	May LTM EDH (m) for the WNP AOI.	76
Figure 67.	June LTM EDH (m) for the WNP AOI.....	76
Figure 68.	August LTM EDH (m) for the WNP AOI.....	77
Figure 69.	September LTM EDH (m) for the WNP AOI.	77
Figure 70.	November LTM EDH (m) for the WNP AOI.	78
Figure 71.	December LTM EDH (m) for the WNP AOI.	78
Figure 72.	February LTM RDR (nmi) for WNP AOI.	79
Figure 73.	March LTM RDR (nmi) for WNP AOI.....	79
Figure 74.	May LTM RDR (nmi) for WNP AOI.....	80
Figure 75.	June LTM RDR (nmi) for WNP AOI.....	80
Figure 76.	August LTM RDR (nmi) for WNP AOI.....	81
Figure 77.	September LTM RDR (nmi) for WNP AOI.	81
Figure 78.	November LTM RDR (nmi) for WNP AOI.	82
Figure 79.	December LTM RDR (nmi) for WNP AOI.	82
Figure 80.	October conditional composite based on the five shortest RDR years of a generic radar.....	83
Figure 81.	October conditional composite based on the five longest RDR years of a generic radar.....	83
Figure 82.	October conditional anomaly based on the five shortest RDR years of a generic radar.	84
Figure 83.	October conditional anomaly based on the five longest RDR years of a generic radar.	84
Figure 84.	October LTM of RDR (nmi) for a generic radar.	85
Figure 85.	October conditional composite based on the five lowest EDH years..	85
Figure 86.	October conditional composite based on the five highest EDH years	86
Figure 87.	October conditional anomaly based on the five lowest EDH years. ...	86
Figure 88.	October conditional anomaly based on the five highest EDH years. ..	87

LIST OF TABLES

Table 1.	Reanalysis variables and variables calculated from reanalysis variables that were used in this study. <i>Not App</i> means not applicable.	21
----------	---	----

THIS PAGE INTENTIONALLY LEFT BLANK

LIST OF ACRONYMS AND ABBREVIATIONS

14WS	14 th Weather Squadron
AFW	Air Force Weather
AOI	Area of Interest
APM	Advanced Propagation Model
AREPS	Advanced Refractive Effects Prediction System
ASOS	Automated Surface Observing Station
ASTD	Air-Sea Temperature Difference
ASW	Anti-Submarine Warfare
ATMS	Atmosphere
BonD	Battlespace on Demand
CDC	Climate Diagnostics Center
CSI	Critical Success Index
dB	Decibel
DoD	Department of Defense
ECS	East China Sea
EDH	Evaporation Duct Height
EN	El Nino
ENSO	El Nino Southern Oscillation
EOF	Empirical Orthogonal Function
ESM	Electronic Support Measures
ESRL	Earth System Research Laboratory
FAR	False Alarm Rate
HSS	Heidke Skill Score

IDM	Indian Dipole Mode
IOZM	Indian Ocean Zonal Mode
LN	La Nina
LRF	Long Range Forecast
LTM	Long-Term Mean
MEI	Multivariate ENSO Index
METOC	Meteorology and Oceanography
MJO	Madden-Julian Oscillation
NCEP	National Centers for Environmental Prediction
NCAR	National Center for Atmospheric Research
nmi	Nautical Mile
NOAA	National Oceanic & Atmospheric Administration
NPS	Naval Postgraduate School
PC	Percent Correct
RDR	Radar Detection Range
SCS	South China Sea
SST	Sea Surface Temperature
TS	Threat Score
U.S.	United States
WNP	Western North Pacific

ACKNOWLEDGMENTS

I would like to thank Fleet Numerical Meteorology and Oceanography Center for offering me the opportunity to attend the Naval Postgraduate School.

I would like to recognize my advisors, Dr. Tom Murphree and Mr. Paul Frederickson, for all their guidance and patience. Many thanks go to Mr. Bob Creasey for retrieving reanalysis data that is the backbone of this thesis.

I owe a large debt of appreciation to my parents for always supporting and believing in me. To my friends, I am grateful for the encouragement and support throughout this educational journey.

THIS PAGE INTENTIONALLY LEFT BLANK

I. INTRODUCTION

A. MOTIVATION

The focus of this study is the long range prediction of radar detection ranges (RDRs) for planning anti-submarine warfare (ASW) operations. With knowledge of expected RDRs in the area of interest at long lead times, an operational planner can make more effective decisions regarding offensive or defensive ASW tactics. More skillful long range environmental forecasts will give operational planners a better understanding of what types of environmental scenarios to expect leading to more insightful decisions concerning, for example, platform positioning in the area of operations.

Presently, the planning of ASW operations and naval operations in general, begins on the order of three to six months before the operation starts. For environmental information, the planners of these operations generally rely on Navy climatologies that describe the estimated long term mean conditions that have occurred in the past. These climatologies are generally based on outdated data sets and analysis methods. Long range forecasts (LRFs; lead times of two weeks or longer) are almost never available to the planners. In this study, we investigated the use of modern data sets and methods for developing state-of-the-science climate analyses and long range environmental predictions.

Much of the motivation for this study came from comparing existing U. S. Navy climatologies with new experimental climate products developed using modern methods. Figure 1 shows a comparison of traditional and modern, or smart, climatology from Twigg (2007) for the evaporation duct height (EDH), a key variable in determining RDRs. As explained in Twigg (2007), the traditional EDH climatology provides information in text format only and is based on outdated data sets and data analysis methods. The smart EDH climatology is

provided in graphical map format and is based on advanced data sets and data analysis methods, and gives more accurate and reliable results at much higher spatial and temporal resolutions.

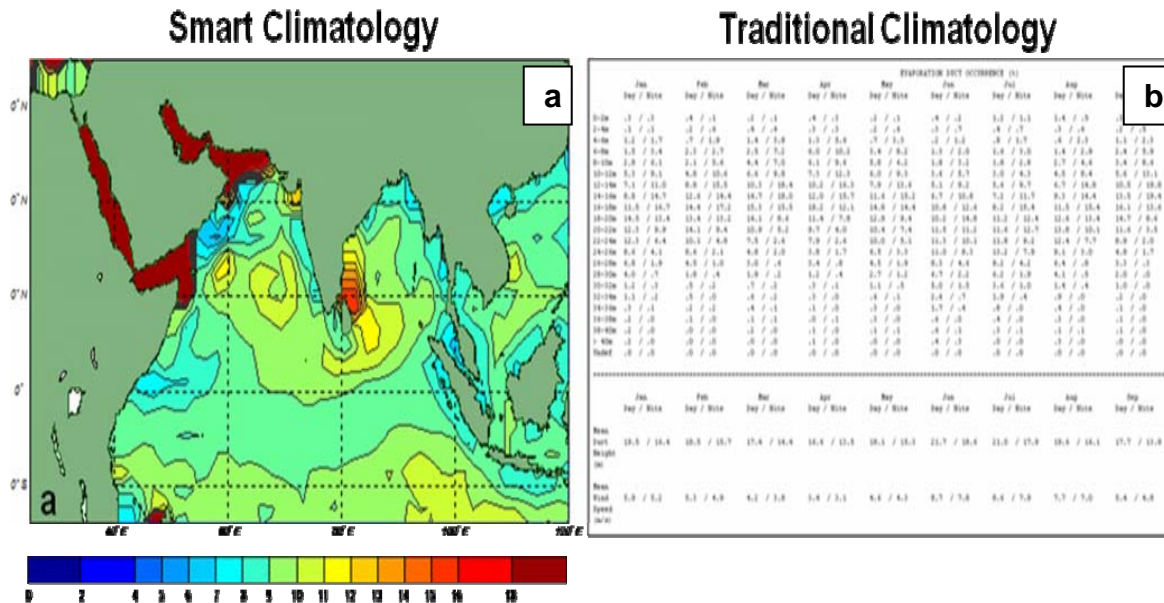


Figure 1 Evaporation duct height (EDH, in m) for September from: (a) NPS smart EDH climatology and (b) existing Navy climatology. NPS smart climatology developed from existing civilian multi-decadal atmospheric and oceanic reanalysis data sets. From Twigg (2007).

B. DEFINITIONS

1. Smart Climatology

Smart climatology, or warfighter climatology, is a concept developed by Dr. Tom Murphree and Rear Admiral David Titley. It can be defined as state-of-the-science basic and applied climatology that directly supports Department of Defense (DoD) operations. Smart climatology involves the use of state-of-the-science data sets, data access and visualization tools, statistical and dynamical analysis, climate modeling, climate prediction, and climate science decision analysis and support tools for risk assessment, mitigation, and exploitation (Murphree 2008a).

2. Traditional Climatology

Traditional climatology is defined in this study as the climatological methods currently employed by the U. S. Navy. Traditional climatology relies mainly on long term mean (LTM) descriptions of climate system variables that are of interest to warfighters. In some cases, LTMs provide useful guidance for planners. But in many other cases, LTMs do not accurately depict the present or future state of the climate system. This is largely because: (a) many of the LTMs used in Navy climatology are based on inadequate and/or outdated data sets; and (b) the climate system undergoes large variations that LTMs cannot explicitly describe. For example, some Navy climatologies are constructed in part from observational sea surface temperature data from ships during the period 1854-1997. These climatologies differ significantly from those based on more recent observations, analyses, and reanalyses. This is in part because the former data set is: (a) sparse in many areas, especially outside of common shipping lanes and for times of infrequent ship travel due to inclement weather; and (b) not up to date and so does not represent the most recent decade(s). Modern or smart climatologies emphasize the use of data sets and methods that compensate for the shortcomings of traditional climatologies by, for example, focusing on data from all reliable sources, data from the satellite era (e.g., 1970 onward), and modern reanalysis methods for providing consistent multi-decadal, and state-of-the-science descriptions of the climate system.

3. Smart Climatology Processes

The smart climatology process has been described and evaluated in many studies, and through interactions between warfighters and Naval Postgraduate School (NPS) faculty and students (e.g., LaJoie 2006; Hanson 2007; Montgomery 2008; Moss 2007; Tournay 2008; Turek 2008; Twigg 2007; Mundhenk 2009). Figure 2 shows the process that the NPS smart climatology team uses to provide smart climatology support. The process starts with identifying customer needs, timeline for completion, and the climate support

products that will be most beneficial for warfighters. In step two, information about the mission (e.g., dates, objectives, operational thresholds) are used to design the development and delivery of the climate support products. Step three is to obtain and assess the required resources, for example, the appropriate data sets, and analysis and prediction tools. In step four, the data sets and tools are used to conduct analyses and produce predictions of the relevant environmental conditions. The environmental predictions are then applied to tactical decision aids and other tools to produce: (a) predictions of the operational impacts of the expected environmental conditions; and (b) recommendations for how to deal with the predicted impacts. The overall result of step five is a smart climatology product support package delivered to military planners. The final step in the smart climatology process is to verify, validate, and assess the operational value of the support process and resulting support package.

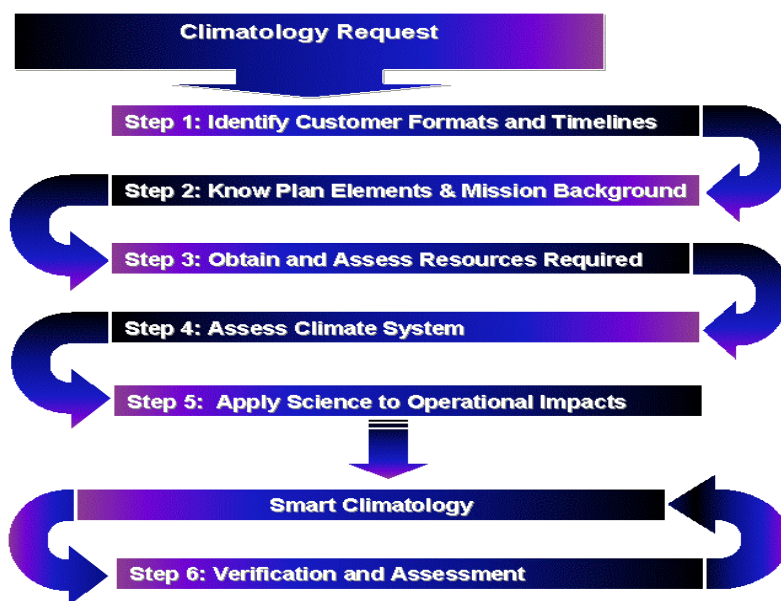


Figure 2. The smart climatology process. From LaJoie (2006).

4. Smart Climatology Elements and Gaps in Military Support

Figure 3 shows the seven major elements of climate support identified by Murphree (2008a). This figure also compares the overall status of operational

climate support by operational civilian climate centers and military climate centers. For all seven elements, military support lags civilian support, with the status of military support being comparable to the status of civilian support several decades ago. In the last 5-10 years, the Navy meteorology and oceanography (METOC) and Air Force Weather (AFW) communities have become increasingly aware of these gaps in the climate support they provide. However, the will and the resources to correct these gaps have been minimal, so far. One motivation for this study is to provide additional evidence of the gaps in military climate support, identify feasible methods for rapidly filling those gaps, and make recommendations on how to quickly improve military climate support capabilities. Many improvements are possible at relatively low cost by adapting existing civilian data sets and methods that are available at little or no cost (Murphree 2008a).

Smart Climatology: Civilian-Military Comparison

State-of-the-Science Climatology Element	Civilian Climo Operations *	Military Climo Operations *
Data sets	Yes	Very limited
Data access & visualization	Yes	Very limited
Statistical & dynamical analysis	Yes	Very limited
Climate modeling	Yes	No
Climate monitoring	Yes	No
Climate prediction	Yes	No
Climate scale decision analysis	Yes	No

Figure 3. A comparison of the status of routine, readily available, operational climate support from operational civilian and military centers in terms of the seven major elements of climate support. From Murphree (2008a).

5. Smart Climatology and Battlespace on Demand (BonD)

Figure 4 illustrates the Battlespace on Demand (BonD) concept was developed by the Navy METOC community to define the process by which the U. S. Navy provides environmental support to warfighters. BonD has four tiers,

each representing a different step in providing support. The first step, known as Tier 0, represents the development of environmental data sets. Tier 1 represents the use of the data sets and various analysis and forecasting tools to describe and predict the environment. Tier 2 represents the development of analyses and predictions of how the environment affects military equipment (e.g., radar, sonar, ships). Tier 3 describes the development of analyses and recommendations for military planners on how best to exploit environmental opportunities and mitigate environmental risks.

The BonD concept was developed to describe short range support (e.g., support provided at lead times of five days or less), but the concept also applies to long lead support, including climate support. In Figure 4, the pink text boxes identify smart climatology products associated with each of the four BonD tiers. In this study, we developed examples of smart climatology products for all four BonD tiers, including climate scale analyses and long range forecasts of radar detection ranges, which are examples of a Tier 2 and 3 products.

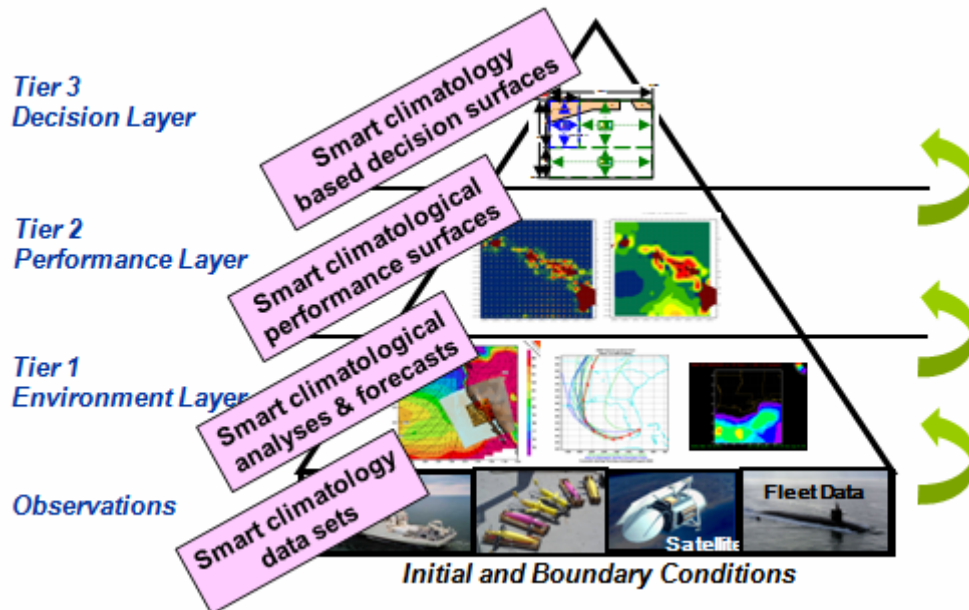


Figure 4. Schematic depiction of the Battlespace on Demand (BonD) including descriptions of smart climatology support products for each of the four BonD tiers. From Murphree (2008a).

C. RADAR TACTICAL DECISION AIDS

1. Definitions

a. Propagation Loss

Radar propagation loss is defined as the ratio of the transmitted power over the received power (assuming the antenna patterns are normalized to unity gain) at a given point in space. Propagation loss is expressed in terms of decibels (dB).

b. Radar Detection Range

For the purposes of this study, radar detection range (RDR) is defined as the maximum distance from a radar antenna at which a specific target can be detected by a given radar system. RDR is sometimes referred to as the target detection range. In order to estimate RDR, the propagation loss versus range at the target height first needs to be computed. A target can theoretically be detected where the propagation loss is less than the detection threshold value, and cannot be detected where the propagation loss is greater than the threshold. The RDR can therefore be defined as the maximum distance from a radar at which the propagation loss equals the detection threshold. The detection threshold value is a function of the radar system attributes and the target's size, shape, composition, and orientation with respect to incident radar waves. The RDR as defined above is only an approximation, although often a very good approximation, of the actual range at which a surface or low altitude target might be detected in a real-world situation. Radar target detection depends on other factors in addition to the propagation loss, such as sea clutter, system signal-to-noise ratios, and the signal filtering and target recognition procedures being employed.

2. Use of Climatology in Tactical Decision Aids

a. Traditional Climatology

Atmospheric electromagnetic propagation tactical decision aids (TDAs) currently in use by the U. S. military are based on traditional climatologies that were produced from outdated data sets. These data sets were created primarily from observations from ships that followed major shipping lanes and avoided areas of inclement weather using methods from the late 1980s and early 1990s.

b. State-of-the-Science Atmospheric Reanalysis

In order to provide warfighters with the most accurate analyses and forecasts of the climate system possible, the best and most up-to-date data sets should be used as inputs to TDAs. As mentioned previously, the climate system is always changing. Figure 5 shows an example of this in terms of the long term mean (LTM), interannual variations, and long term trend in sea surface temperature (SST) in the East China Sea for the last four decades. LTM data is presently the standard used in most Navy TDAs. Figure 5 illustrates how LTM data can provide a very misleading representation of the environment. SST is an input to TDA-based predictions of RDRs. Using up-to-date and state-of-the-science data sets for SST and other variables that affect radar performance is important in getting reliable results from radar TDAs.

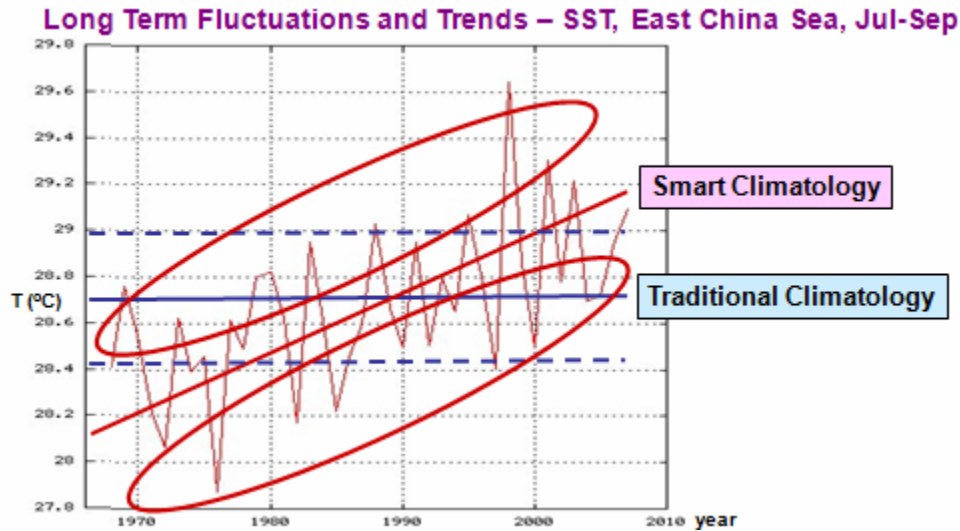


Figure 5. Sea surface temperature (SST; C°) in the East China Sea for July - September of 1968-2006. Traditional climatology describes the long term mean SST and related quantities (e.g., the long term mean high and low SST) shown by the solid and dashed blue lines. But traditional climatology does not describe interannual variations (identified by red ovals), long term trends (identified by red line), and other deviations from long term mean conditions.

3. Naval Postgraduate School Bulk Model

The Naval Postgraduate School (NPS) has created a state-of-the-science operational bulk evaporation duct model that computes the near-surface modified refractivity profile and evaporation duct height from measured or modeled values of wind speed, air and sea temperature, relative humidity, and atmospheric pressure. The NPS model is based on Monin-Obukhov similarity theory and is therefore only valid within the atmospheric surface layer, which extends upwards on the order of 10 to 100 meters above the surface, depending on atmospheric stratification conditions. The model uses a modified form of the TOGA-COARE bulk algorithm to compute the surface layer scaling parameters, which are then used to compute the modified refractivity profile up to a height of 100 m. The evaporation duct height is determined by finding the height of the local minimum in the modified refractivity profile that occurs nearest to the surface. In order to prevent erroneous solutions from the model, the NPS model incorporates operational checks on all input data and flags any impossible or unrealistic

cases. The modified refractivity profile is used as the environmental input to electromagnetic propagation models, such as the Advanced Propagation Model (APM) described in the next section.

Previous studies (e.g., Frederickson 2008) have shown that the Naval PostgraduateSchool bulk model has outperformed the Paulus-Jeske (P-J) Model, which is the current model in the Advanced Refractive Effects Predicted System (AREPS) and used by the U.S. Navy for radar detection range and propagation loss. See Figure 6 for a comparison of propagation loss as determined from measurements, the NPS model, the P-J model, standard atmosphere, and free space measurements (Frederickson 2008).

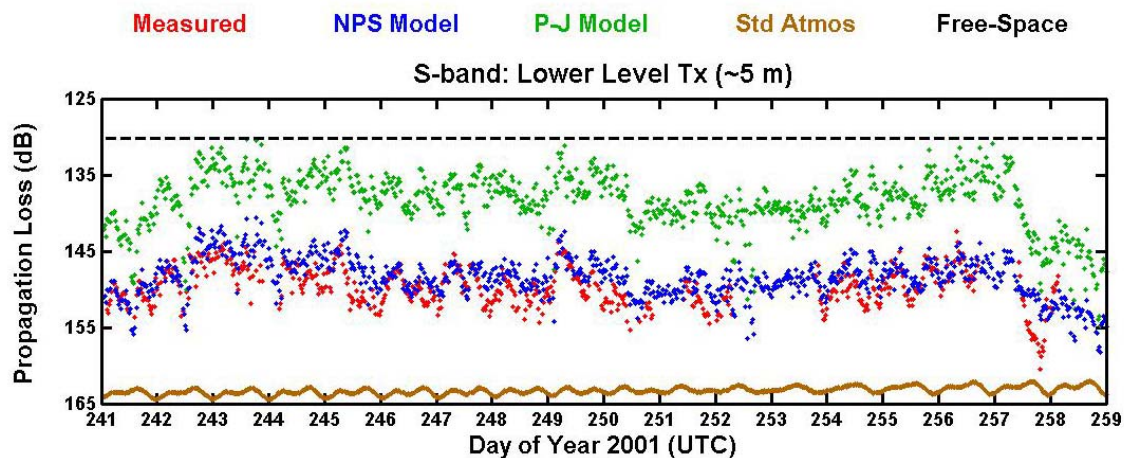


Figure 6. Comparison of the propagation loss (dB) for a 19 day period in 2001 as determined by measurements (red), NPS model (blue), P-J model (green), standard atmosphere, (brown) and free space measurements (black). From Frederickson (2008).

Recently, the NPS bulk model has been incorporated in the latest version of AREPS TDA, developed by the Space and Naval Warfare Systems Center, San Diego, CA. Frederickson (2008) used the results of this study to assess the NPS bulk model as follows:

The error and sensitivity analysis conducted in this study demonstrates that the NPS model's accuracy is highly dependent upon the atmospheric stability conditions. In stable situations (the air warmer than the sea surface) with moderate to high wind

speeds and humidity, the model may perform adequately well for propagation modeling purposes. With large positive air-sea temperature differences and low wind and humidity, however, the model results become highly suspect because Monin-Obukhov similarity theory, upon which the model is based, begins to break down in such low-turbulence situations. In addition, the model becomes extremely sensitive to the input parameters in highly stable conditions. In some cases evaporation duct height errors can exceed 4 m as a result of only modest uncertainties in the model inputs. In unstable conditions (the air colder than the sea surface), the NPS model produces highly accurate evaporation duct and refractivity profile information, suitable for high-fidelity propagation modeling applications. Fortunately, unstable conditions are the most prevalent situation over the world's oceans. The error and sensitivity analysis in this study demonstrated that when provided with high quality input data the NPS model can determine the evaporation duct height with an accuracy of about 2 m or better in almost all unstable cases. When the NPS model is used in conjunction with modern propagation codes, such as the Advanced Propagation Model, near surface propagation loss predictions accurate to about 1-3 dB at a range of 30 km and 3-7 dB at 60 km can be expected in unstable conditions for a S-band radar. Near surface target detection range errors were estimated to be approximately 1-4 km for a target that is normally detectable at 30-35 km, and 2-8 km for a target normally detected at 50-70 km. Real-time propagation assessments and short-range forecasts with such accuracies would constitute a highly valuable tool for planning and executing naval and maritime operations. It must be noted that these accuracy estimates do not take into account potential errors due to temporal and spatial variations in atmospheric refractivity or surface scattering conditions, for example. (Frederickson 2008).

4. Advanced Propagation Model

We used the Advanced Propagation Model (APM) in our study to compute the propagation loss for a specific height versus range coverage area. APM was developed by the Atmospheric Propagation Branch of the Space and Naval Warfare Systems Center, San Diego (Barrios and Patterson 2002) and uses a hybrid ray-optic and parabolic equation model to compute the propagation loss. In order to generate radar detection range analyses and forecasts, we used the NPS bulk evaporation duct model to compute the modified refractivity profile,

which was then used as input to APM. APM then computed the propagation loss versus range at the target height for a specific radar system, from which the radar detection range was determined.

5. Advanced Refractive Effects Prediction System

The Advanced Refractive Effects Prediction System (AREPS) was developed by the Space and Naval Warfare Systems Center, San Diego and is used by the U. S. Navy to determine radar probability of detection, propagation loss, and signal-to-noise ratios, electronic support measures (ESM) vulnerability, UHF/VHF communications, and surface-borne surface-search radar capability versus range, height, and bearing from a transmitter (Patterson 1987). For this study, AREPS was used to determine the frequency of occurrence of evaporation ducts over the western North Pacific (WNP), especially the East China Sea (ECS), South China Sea (SCS), and surrounding waters. We used smart climatology data sets and methods to develop the input fields for AREPS to expand on what AREPS can provide and give warfighters climate analyses and forecasts of radar performance for large regions, instead of the probability of detection at specific point locations.

D. REFRACTION, DUCTING, AND RADAR DETECTION RANGES

Due to the common occurrence of evaporation ducts over the ocean and their strong impact on near-surface radar propagation, it is important to accurately predict the characteristics of evaporation ducts in order to estimate the radar detection and tracking of submarine periscopes, low-flying missiles and aircraft, and surface combatants. In our study, we focused on the ability to predict radar detection ranges for submarine periscopes using surface ship-based search radars. In the following sections we describe how the near-surface atmospheric and sea surface conditions affect radar propagation and detection ranges.

1. Modified Refractivity and Ducting Layers

Vertical and horizontal gradients of the refractive index of air determine the propagation of electromagnetic radiation through the atmosphere. The refractive index of air, n , is defined as the ratio of the speed of an electromagnetic wave through a vacuum over the speed through air (Frederickson 2008). Electromagnetic waves bend or refract toward regions of higher n . The refractivity, denoted as N , describes the difference of n from unity and is often used since n is always close to unity. For the radar wavelengths that we used in our research, N is related to the atmospheric variables of absolute temperature (T), partial pressure of water vapor (e), and total atmospheric pressure (P) through the following equation (Bean and Dutton 1968):

$$N = 77.6 \frac{P}{T} - 5.6 \frac{e}{T} + 3.75 \times 10^5 \frac{e}{T^2} \quad (1)$$

where T is in Kelvin, and P and e are in hPa.

The modified refractivity, m , takes into account the curvature of Earth's surface, which assists in determining the presence or absence of ducts and trapping layers. Equation 2 defines modified refractivity as:

$$m = N + \frac{z}{r_e * 10^{-6}} = N + 0.1568z \quad (2)$$

where z is the height above the ocean surface, r_e is Earth's radius ($\sim 6.378 \times 10^6$), and both are expressed in meters. The vertical gradient of m (dm/dz) determines the direction waves are refracted relative to Earth's surface, rather than its absolute value. When $dm/dz = 0$, the electromagnetic ray curvature is equal to Earth's curvature and propagating waves travel parallel to Earth's surface. When $dm/dz > 0$, electromagnetic rays curve upward relative to Earth's surface, and when $dm/dz < 0$, electromagnetic rays curve downward relative to Earth's surface.

When a negative dm/dz layer extends down to the surface, electromagnetic rays can be trapped between the reflecting surface and the top of the layer. This phenomenon is known as ducting (Frederickson 2008). Figure 7 shows examples of different types of modified refractivity profiles and the associated ducting conditions.

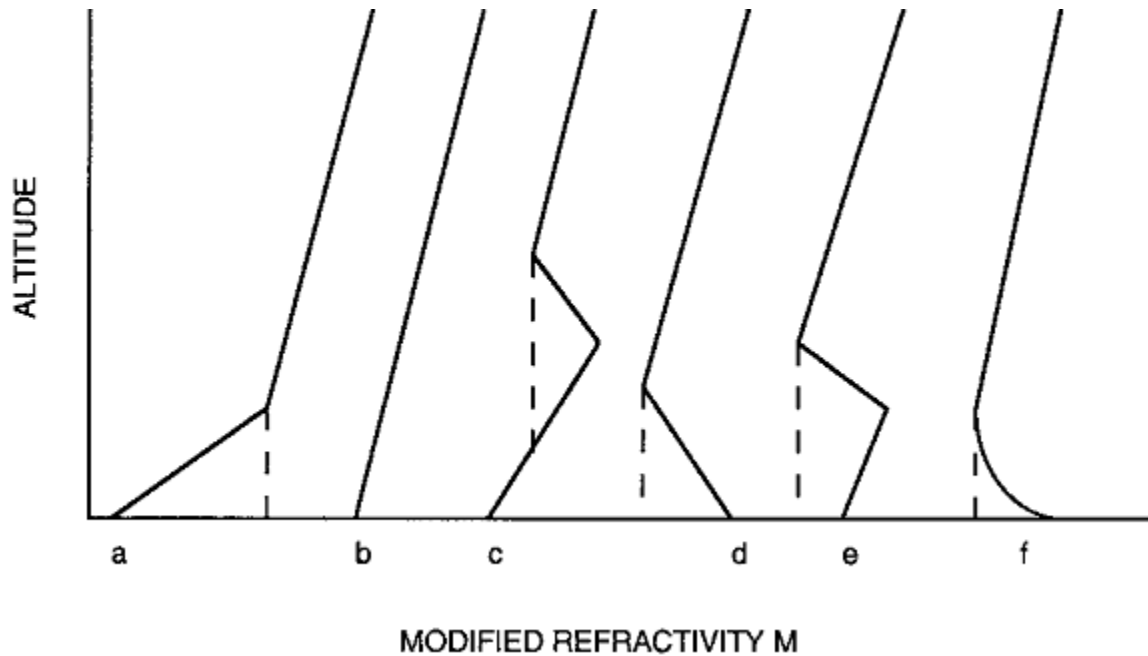


Figure 7. Plots of modified refractivity (M) versus altitude: (a) sub-refractive layer denoted by dashed line; (b) normal refraction; (c) elevated duct denoted by dashed line; (d) surface duct denoted by dashed line; (e) surface-based duct denoted by dashed line, (due to an elevated layer with a strongly negative vertical M gradient); (f) evaporation duct denoted by dashed line. From: Babin et al. (1997).

Figure 8 shows a case in which a negative dm/dz layer extends down to the surface and ducting occurs, which can result in greatly extended radar detection ranges.

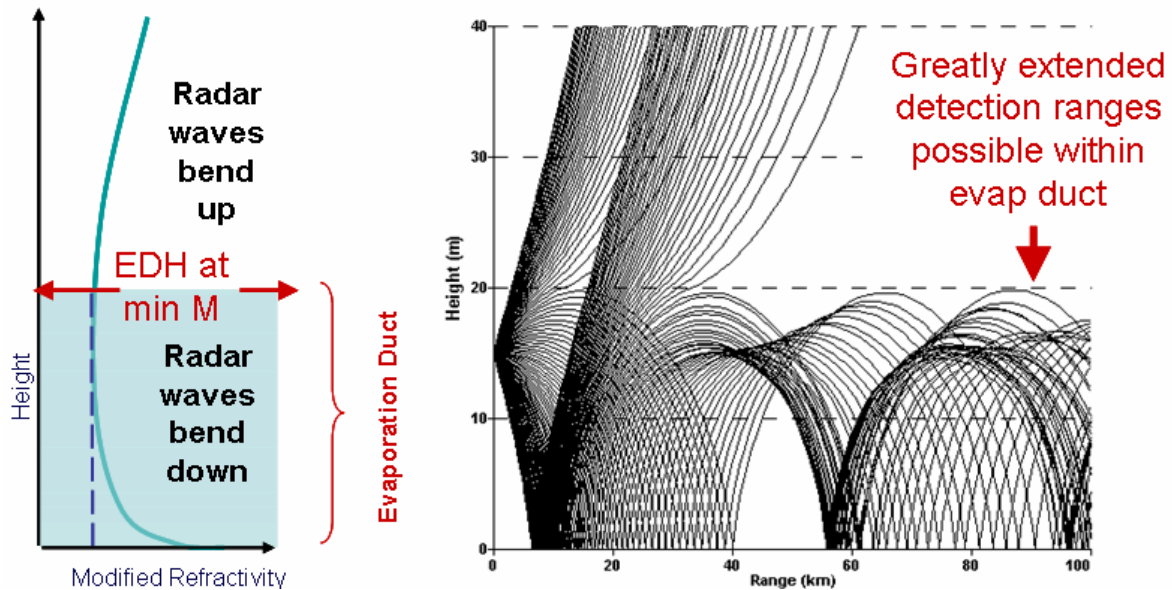


Figure 8. A vertical M profile for a surface duct and its associated height versus range ray trace plot of X-band waves emitted from an antenna at 25 m height propagating through an atmosphere with an EDH of 20 m. From Frederickson et al. (2000).

2. Environmental Factors Affecting the Evaporation Duct

The evaporation duct is mainly affected by four environmental factors: near-surface wind speed, air temperature, and relative humidity, and sea surface temperature. Evaporation duct height generally increases as relative humidity decreases for all stability conditions (except over a narrow range of slightly positive ΔT values with low winds). When the relative humidity is low and the air-sea temperature difference (ASTD) is positive, the evaporation duct height may become undefined. When the relative humidity is high and the ASTD is positive, or even slightly negative, there may be no evaporation duct present in the surface layer, as indicated by an evaporation duct height value of zero. The evaporation duct height increases with wind speed in unstable conditions and at some slightly positive ΔT value. As stability conditions change from neutral to weakly stable, the situation is reversed, and evaporation duct heights decrease

with wind speed. For a given ASTD, the evaporation duct height generally increases with increasing sea surface temperature (Frederickson 2008).

3. Electromagnetic Propagation and Detection Ranges

The best single parameter for quantifying near-surface microwave propagation is the evaporation duct height (EDH). The EDH is a critical factor in determining the near-surface refractivity conditions and higher EDHs often lead to increased signal strength and radar detection ranges, depending upon the frequency, and the height of the radar and target (Twigg 2007). Radar detection ranges are estimated from the computed propagation loss by determining the maximum distance where the propagation loss at the target height is equal to the propagation loss detection threshold assumed for the target (Twigg 2007). Propagation loss will decrease and the detection range will increase when the radar and target are located within the duct. Even when the radar and target are not located within the duct there can be some trapping of EM energy within it and extended detection ranges are possible.

4. Current Radar Detection Range Products

Currently, the U. S. Navy provides few radar detection range products as tactical guidance to warfighters. Forecast in the form of threshold-based stop-light charts are produced at lead times of a couple days in advance. The Advanced Refractive Effects Prediction System (AREPS) (see Chapter I, section C, part 4) is used to plot electromagnetic propagation for specific sensor systems and environmental conditions. These products rely on an outdated bulk evaporation duct model and an outdated climatological data set. This study examined the potential of state-of-the-science climate data sets and methods to produce products for warfighters that are both more accurate representations of the actual environment that will be encountered during an operation and more relevant to warfighter needs.

E. OVERVIEW OF THIS STUDY

Our study addressed the following research questions:

1. Can state-of-the-science data sets and methods be used to create a more accurate and useful characterization of atmospheric radar propagation, and thus provide tactically significant improvements in war fighting capabilities?
2. Can skillful long range forecasts of evaporation duct heights and radar detection ranges be developed for mission planning purposes?

We addressed these questions in the context of the western North Pacific (WNP), centered on the East China Sea (ECS) and nearby waters (15-45°N, 95-145°E; see Figure 9). We chose this as our study area because it is affected by several major climate variations, it is operationally significant to the U. S. military, and prior studies have shown skill at long range forecasting in this region (cf. Ford 2000; Tournay 2008; Turek 2008; Mundhenk 2009). The WNP region bounded by 20-28°N and 122-126°E (red box in Figure 9) was a focus area for developing our long range forecasting methods.

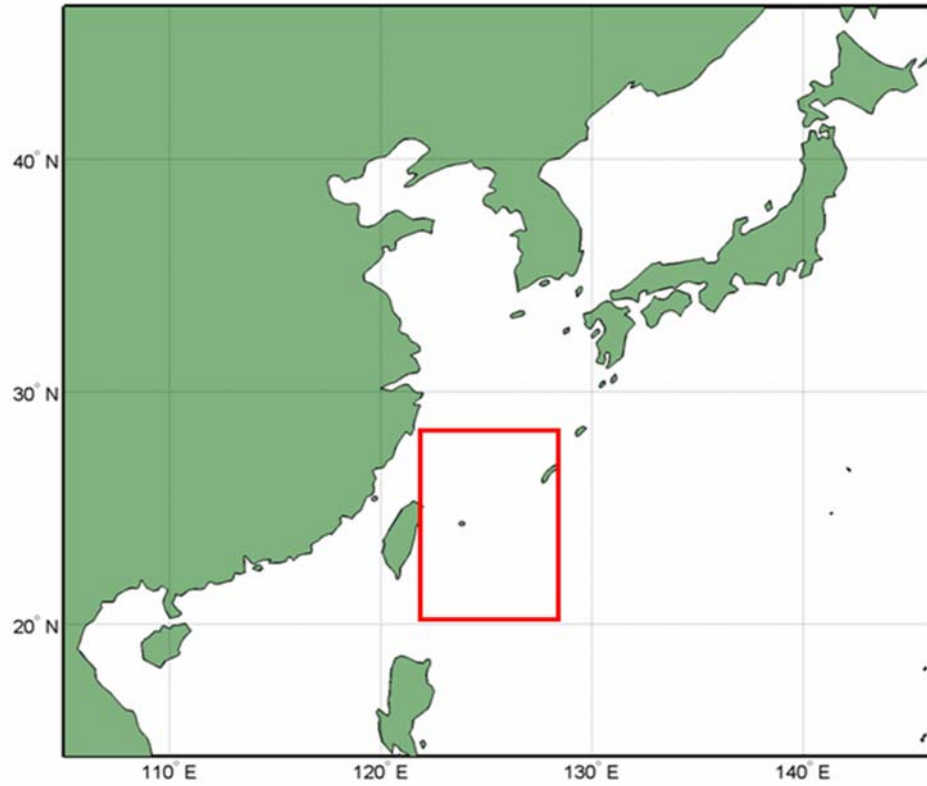


Figure 9. Western North Pacific study region. The red box encompassing 20-28°N and 122-126°E was a focus area for developing our long range forecasting methods.

Our data and methods are presented in Chapter II. In Chapter III, we present our answers to our research questions. Chapter IV provides a summary of our results, conclusions, and suggestions for future research.

II. DATA AND METHODS

A. DATA

The main environmental data used in this study was obtained from the National Center for Environmental Prediction and the National Center for Atmospheric Research (NCEP/NCAR) Reanalysis-1 data set. The data set was obtained on March 20, 2009, via the National Oceanic & Atmospheric Administration (NOAA) Climate Diagnostic Center (CDC) website (<http://www.cdc.noaa.gov>). The NCEP/NCAR reanalysis-1 data set includes data for a wide range of standard atmospheric variables plus sea surface temperature (SST). The reanalysis data set has a 1.875° latitude by 1.875° longitude spatial resolution, which is equivalent to about 210 km horizontal resolution, and a temporal resolution of every 6 hours (0, 6, 12 and 18Z) (Kistler 2001). Figure 10 shows the reanalysis grid for our WNP study area, or area of interest (AOI). The data set spans 61 years (1948 to present). However, for this study we only used data from 1970-2008, based on our determination that the reanalysis data prior to 1970 are less reliable, mainly due to a lack of significant amounts of satellite data prior to the 1970s. This lack of data is especially significant for studies such as ours that deal with environmental conditions over the ocean. The reanalysis data set incorporates ship, land surface, satellite, rawinsonde, aircraft, and other data sets. This data is assimilated via a T62 global spectral model with 28 vertical sigma levels (Kistler 2001). The vertical resolution of the reanalysis data set is not high enough to explicitly resolve EM ducts just above the ocean surface. However, the evaporation duct over the ocean can be characterized in terms of surface quantities (see Chapter II, section D), so we were able to use the reanalysis data to calculate EDHs and the related RDRs. The reader is referred to Kalnay et al. (1996) and Kistler et al. (2001) for further details regarding the reanalysis data set.

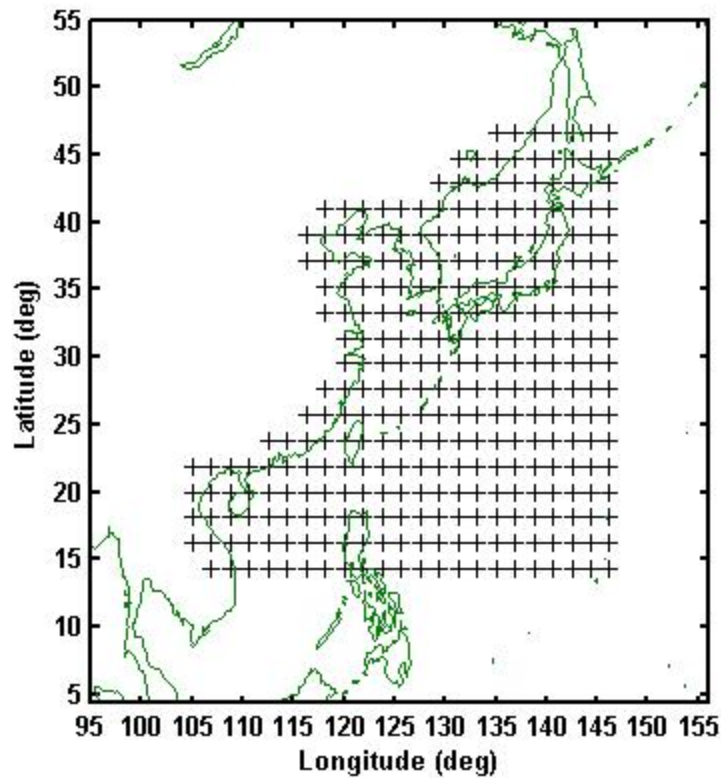


Figure 10. Western North Pacific study area with mesh showing locations of reanalysis data grid points used in our calculations of evaporation duct heights and radar detection ranges.

The following NCEP/NCAR reanalysis variables were required to compute the modified refractivity profiles and EDH: zonal wind, meridional wind, specific humidity, air temperature, sea level pressure, and sea surface temperature. From these variables, additional variables were calculated. Table 1 lists the reanalysis variables and calculated variables.

Table 1. Reanalysis variables and variables calculated from reanalysis variables that were used in this study. *Not App* means not applicable.

Reanalysis Variables	Height (m)
Air Temperature	2m
Sea Surface Temperature	Surface
Relative Humidity	2m
Zonal Wind	10m
Meridional Wind	10m
Sea Level Pressure	Surface
Calculated Variables	Height (m)
Wind Speed	10m
Air-Sea Temperature Difference	Surface
Specific Humidity	2m
Evaporation Duct Height	Not App
Radar Detection Range	Not App

B. METHODS

1. Evaporation Duct Height and Radar Detection Range Calculations

The six hourly wind speed, air and sea surface temperatures, relative humidity, and atmospheric pressure data from the reanalysis data set were put into the NPS bulk evaporation duct model for each grid point in our area of interest. From these input data, the NPS model computed the modified refractivity profile up to a height of 100 meters. The evaporation duct height (EDH) was determined by finding the height closest to the surface at which the local minima in modified refractivity occurred.

Next, the modified refractivity profile from the NPS model was put into APM, which computed the propagation loss versus range for our radar parameters at the height of our assumed target. The radar detection range (RDR) was then estimated by finding the maximum distance from the radar where the propagation loss at the target height was equal to the target detection threshold value. Note that in this method we assumed that the environmental

conditions were horizontally homogeneous in the region near each grid point, with no attempt being made to resolve spatial variations in refractivity conditions near each grid point. The spatial variations were determined by the refractivity differences between the grid points.

The evaporation duct height and radar detection range calculations described above are only valid over the ocean. Reanalysis data for grid points close to the coast represent information about conditions over both the land and ocean. This means that an ocean grid point close to land may represent an average of data from both over the land and the ocean. As an example, for such a grid point the surface temperature would be an average of the sea surface temperatures from the ocean areas of the grid box and the land skin temperatures from the land areas. The resulting EDH values from a near shore grid point can exhibit a very drastic change from adjacent grid boxes that are entirely over the ocean. For this reason, EDH and RDR results near coastlines should be treated with caution. To eliminate erroneous EDH and RDR computations from near shore grid points, we created a land mask that eliminated as many land values as possible that could affect our calculations.

2. Climate Analyses

We applied a number of standard climate analysis methods to develop our climate scale analyses and long range forecasts of EDH and RDR in the WNP. During our research, we used various techniques to manipulate the NCEP/NCAR reanalysis data set in order to find deviations from the long term mean and provide the most accurate radar detection ranges for our given environment.

To identify the major temporal variations, we broke the data for 1970-2006 into above normal (AN), near normal (NN), and below normal (BN) tercile categories representing the upper, middle, and lower 33% of the values for each variable of interest. This tercile information was used to: (a) identify years for conditional compositing (see Chapter II, section 4) and long range forecast

development (see Chapter II, section 5); and (b) interpret the physical processes that create climate variations and long range predictability in EDH and RDR in the WNP.

Our analyses were facilitated by use of online tools for processing the reanalysis data made available by the Earth Systems Research Laboratory (ESRL; <http://www.esrl.noaa.gov/>). These tools, plus additional Excel and Matlab based tools, were used to compute long term means, conditional composite means, conditional composite anomalies, time series, and linear correlations. The results of these calculations were used to identify and assess the climate variations that determine how EDH and RDR, and the environmental factors that determine them. Plots of radar detection ranges and evaporation duct heights were generated using MATLAB (Mathworks 2005).

Linear correlation was used to identify relationships between different climate system variables, EDH, and RDR. Correlations between variables at widely separated locations provided us with information about the teleconnections between the variables. Teleconnections describe how variations in the environment at one location are related to those at distant location. In our study, we used such correlations to determine how the environment factors, EDH, and RDR in our WNP AOI were correlated with SST and other environmental variables in remote locations. A two-tailed test was used to determine the significance at a 95% confidence interval. The significance testing for spatial correlations was based on the test statistic equation:

$$Z = \left| \frac{z_{0.025}}{\sqrt{n}} \right| \quad (3)$$

where: Z is the test statistic; $z_{0.025}$ = standard normal distribution = 1.96 and n = 37 years (1970-2006). Z, or correlation, values greater than 0.318 are significant at the 95% level. See Wilks (2006) for additional information on significance testing.

We used conditional compositing to average together past events in which conditions of interest were met. For example, we constructed conditional composites of the conditions over the East China Sea (ECS) in October when extreme conditions occurred — for example, when meridional winds were exceptionally strong and weak (e.g., composites of the five highest and lowest wind events) and when RDRs were exceptionally long and short (e.g., composites of the five longest and shortest RDR events). Using this technique allows us to isolate and analyze the years of greatest variation in the climate system.

We also analyzed how the conditional composites differed from the LTMs by calculating conditional composite anomalies. For these calculations, the conditional composite anomaly was defined as the conditional composite minus the LTM, with the LTM calculated for the base period 1970-2006. The conditional composite anomalies highlight the deviations from normal associated with the conditional composites (e.g., how RDRs during high wind periods tend to vary from LTM RDRs).

3. Forecasting

Figure 11 summarizes the processes used to produce long range forecasts (LRFs) of the environmental factors, EDH, and RDR for the WNP AOI. Step 1 involved identifying the predictands for which LRFs are produced. For our study, the predictands of interest were meridional wind speed, EDH, and RDR in the WNP AOI. Meridional wind was selected because of: (a) the prior work by Turek (2008) that showed strong interannual variations of the meridional wind in our WNP AOI; and (b) the importance of the meridional wind in the WNP AOI in determining EDH via direct influences on ducting and via effects on the other factors that determine EDH (air temperature, SST, and relative humidity). In step 2, correlations between the predictands and other environmental variables (e.g., SST in the tropical Pacific) were computed. These correlations were used in step 3 to select the predictors with the most potential for producing skillful LRFs.

In step 4, hindcasts of the predictands were produced. The hindcast method was based on using the correlation results, and AN, NN, and BN tercile break downs of the predictands and predictors (see Chapter II, section B.2) to identify predictable relationships between the predictors and predictands (e.g., AN SST in the western central equatorial Pacific is strongly associated with BN meridional winds in the WNP AOI). Hindcasts of monthly mean values of the predictands at lead times of 0-5 months were done for the years 1970-2006. In step 5, the hindcasts were verified against reanalysis monthly mean values using a variety metrics calculated using contingency tables. The resulting metrics of hindcast skill were used to identify the predictor-predictand relationships and the lead times with a high potential for skillful LRFs. These high potential relationships and lead times were then used to select develop the LRF method for each predictand. In step 6, LRFs were produced using the methods identified in step 5.

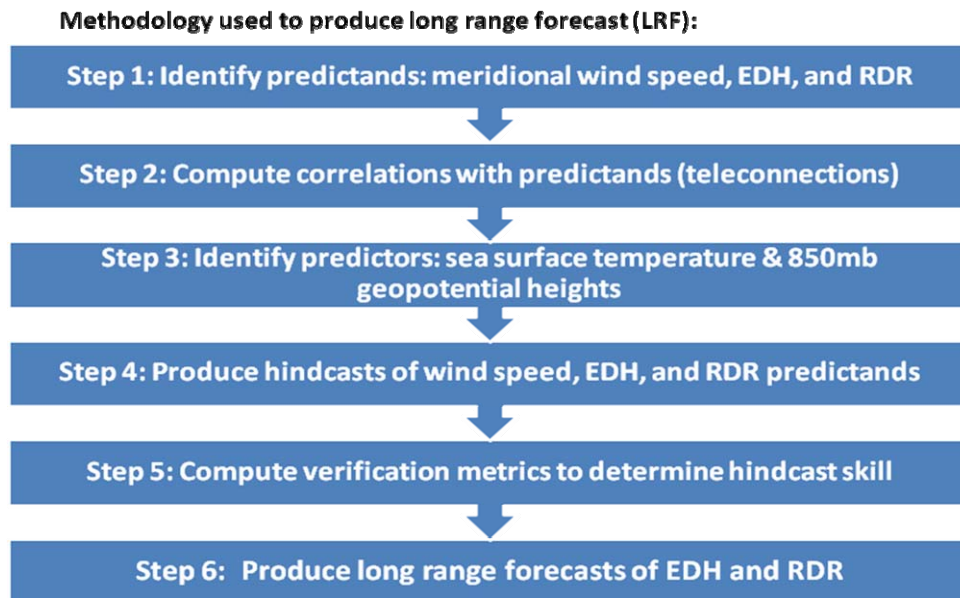


Figure 11. Summary of the long range forecasting process developed and applied in our study.

4. Verification Metrics

a. Contingency Tables

In order to assess the hindcasts and forecasts, we needed to determine what types of errors were made and to quantify the differences between the predicted events and what actually occurred. Two by two contingency tables (e.g., Figure 12) are commonly used to four possible outcomes from forecasts: hits, misses, false alarms, and correct negatives (e.g., Wilks 2006). A perfect prediction would produce only hits and correct negatives. Hits and correct negatives occur when the observed value equals that of the forecast. A hit represents a case in which an event was forecasted and observed. A correct negative represents a case in which an event was forecasted not to occur and it did not occur. The following sub-sections describe the main skill metrics we used to assess our hindcasts and forecasts. See Wilks (2006) and the Australian Bureau of Meteorology web site for more information on forecast verification metrics:

(http://www.bom.gov.au/bmrc/wefor/staff/eee/verif/verif_web_page.html)

		Observed	
		Yes	No
Forecast	Yes	Hit	False Alarm
	No	Miss	Correct Rejection

Figure 12. Two by two contingency table used in our study to categorize and assess our hindcast and forecast results.

b. Percent Correct

The most direct and intuitive measure of non-probabilistic forecast accuracy for discrete events is the percent correct (PC) proposed by Finley (1884). This is simply the percent of forecasts that correctly anticipated the subsequent event or non-event. The percent correct penalizes both kinds of

errors (false alarm and misses) equally. The best (worst) result is 100 (0). PC was calculated as:

$$PC = \frac{Hits + Correct\ Rejection}{Total\ Number\ of\ Forecast} \times 100 \quad (3)$$

c. Probability of Detection

The probability of detection (POD) is defined as the percentage of forecasts that correctly predicted the observed events. The best (worst) result is 100 (0). The POD was calculated as:

$$POD = \frac{Hits}{Hits + Misses} \times 100 \quad (4)$$

d. False Alarm Rate

The false alarm rate (F) is the percentage of forecasts that forecasted events or non-events that did not happen. It is calculated as ratio of false alarms to the total number of non-occurrences of the forecast event or the conditional relative frequency of a wrong forecast given the event does not occur. The best (worst) result is 0 (100). F was calculated as:

$$F = \frac{False\ Alarm}{False\ Alarm + Corret\ Rejection} \times 100 \quad (5)$$

e. Threat Score

The threat score (TS; also known as the critical success index (CSI)) is the number of correct yes forecasts divided by the total number of occasions on which that event was forecast and/or observed. It can be viewed as the proportion correct for the quantity being forecast, after removing correct no forecasts from consideration. The best (worst) possible threat score is one (zero). TS was computed as:

$$TS = CSI = \frac{Hits}{Hits + False\ Alarms + Misses} \quad (6)$$

f. Heidke Skill Score

The Heidke Skill Score (HSS) describes the skill after subtracting credit for accurate forecasts that could have been achieved by random forecasting. Random forecasts define the standard or reference forecast against which the actual forecasts are measured. HSS gives more (less) credit for accurate forecasts of rare (common) events. The best HSS is one, a HSS of zero indicates the forecasts have no skill with respect to the reference forecast, and a HSS less than zero less skill than the reference forecast. We computed HSS as:

$$HSS = \frac{2 \{ (Hits \times Correct\ Rejections) - (False\ Alarms \times Misses) \}}{(Hits + Misses)(Misses + Correct\ Rejections) + (Hits + False\ Alarms)(False\ Alarms + Correct\ Rejections)} \quad (7)$$

C. SUMMARY

The data and methods used in this study are designed to design, develop, and test methods for producing skillful long range forecasts of EDH and RDR that can be used to improve long lead mission planning.

III. RESULTS

A. LONG TERM MEAN SEASONAL CYCLES: LARGE SCALE FEATURES AND PROCESSES

To develop methods for producing skillful LRFs of EDH and RDR in the WNP, it is important to start with an understanding of the seasonal cycle of the large scale features and processes that determine environmental conditions in the WNP. To do so, we examined global scale patterns in surface air temperature, 1000 hPa geopotential height, 850 hPa winds, and SST for winter (January-March), spring (April-June), summer (July-September), and fall (October-December), with a focus on the WNP in January, April, July, and October.

1. Winter

Figures 13-16 show the January LTM surface air temperature, 1000 hPa geopotential height, 850 hPa winds, and SST for most of the globe and centered on the western North Pacific area of interest (WNP AOI) for this study (14°N-47°N, 105°E-148°E; see Figures 9-10). As described in the captions for these figures, the AOI is strongly influenced by large scale atmospheric and oceanic features over Asia, the North Pacific, and the tropical Pacific. The Asian High and accompanying northerly winds along its eastern flank, are especially important features in determining winter air temperature, relative humidities, and winds over much of the AOI. The trade winds on the southern flank of the North Pacific High are important in determining conditions in much of the southern portion of the AOI. The presence of strong gradients in air temperature, geopotential heights, winds, and SST in and near the AOI, and the relationship of these variables and their gradients to hemispheric scale climate features,

suggest that large climate variations are probably in the AOI during winter, and are likely to be related via teleconnections to climate variations in distant locations.

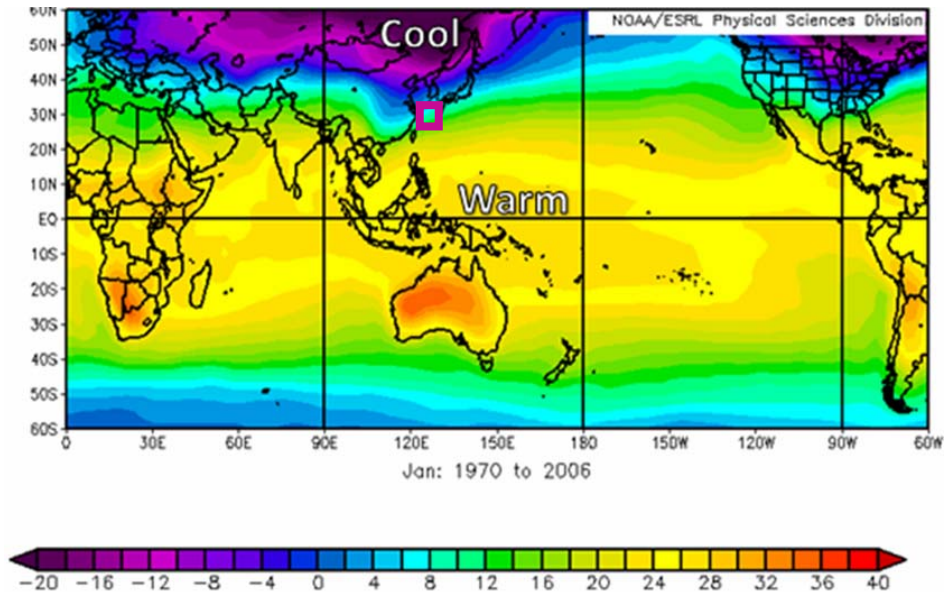


Figure 13. January LTM air temperature ($^{\circ}\text{C}$) at 1000 hPa. Relatively cool (warm) air can be seen over the northern (southern portion) of the WNP AOI (boxed region) for this study. The cool air is associated with the southward outflow of cold dry air along the eastern flank of the Siberian high (see Figures 14-15). Basic figure created at ESRL web site (<http://www.cdc.noaa.gov>, accessed May 2009).

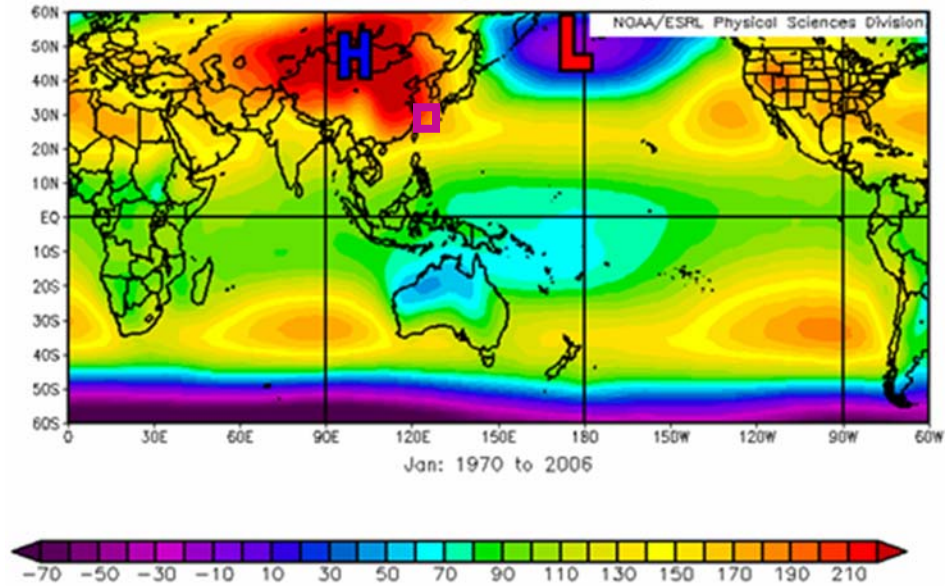


Figure 14. January LTM 1000 hPa geopotential height (m). The WNP AOI (boxed region) for our study occurs on the eastern flank of the Asian High (H) and near the western flank of the Aleutian Low (L) and North Pacific High (centered between Hawaii and California). Climate scale variations in these three height centers can lead to variations in the WNP AOI. Basic figure created at ESRL web site (<http://www.cdc.noaa.gov>, accessed May 2009).

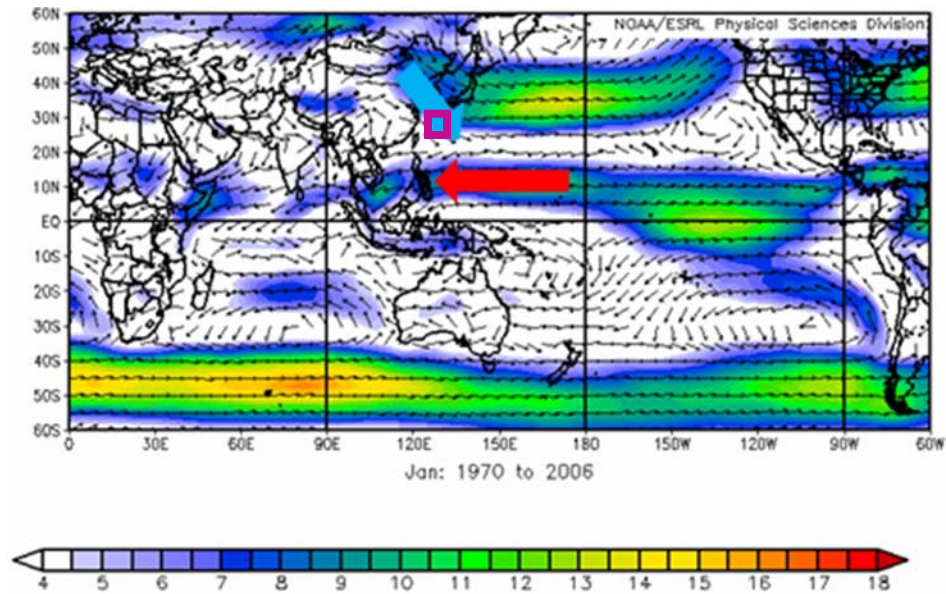


Figure 15. January LTM 850 hPa vector wind (m/s). The northern (southern) portion of the WNP AOI (boxed region) for our study experiences predominantly southward (westward) low level winds. Northerly winds can be seen over the Korean peninsula as a result of the tightened gradient between the Siberian high and the Aleutian low while warm moist air is coming from the easterlies. Basic figure created at ESRL web site (<http://www.cdc.noaa.gov>, accessed May 2009).

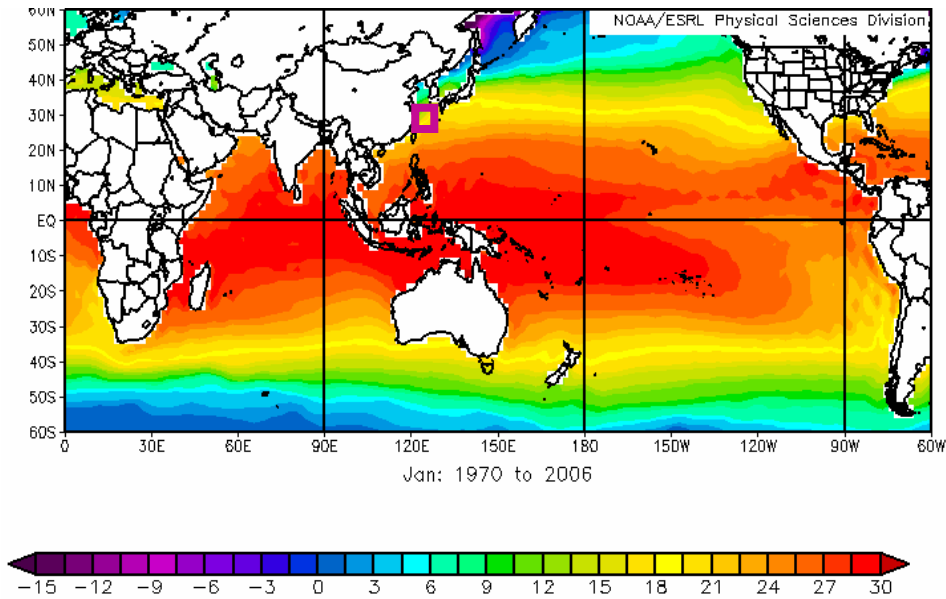


Figure 16. January LTM sea surface temperature (SST; °C). The northern (southern) portion of the WNP AOI (boxed region) for our study experiences relatively warm (cool) SSTs, with strong SST gradients near the Korean peninsula. Basic figure created at ESRL web site (<http://www.cdc.noaa.gov>, accessed May 2009).

2. Spring

Figures 17-20 show the April LTM surface air temperature, 1000 hPa geopotential height, 850 hPa winds, and SST for most of the globe and centered on the WNP AOI for this study. As noted in the captions for these figures, the AOI experiences large seasonal changes in the transition from winter to spring. These changes are closely linked to seasonal shifts in the intensity and location of the Asian High, Aleutian Low, and North Pacific High. This transition causes the AOI to become more tropical in character — for example, via the replacement over much of the AOI of cold, dry air with warm, moist air, and of strong northerly winds with weaker westerly and southerly winds.

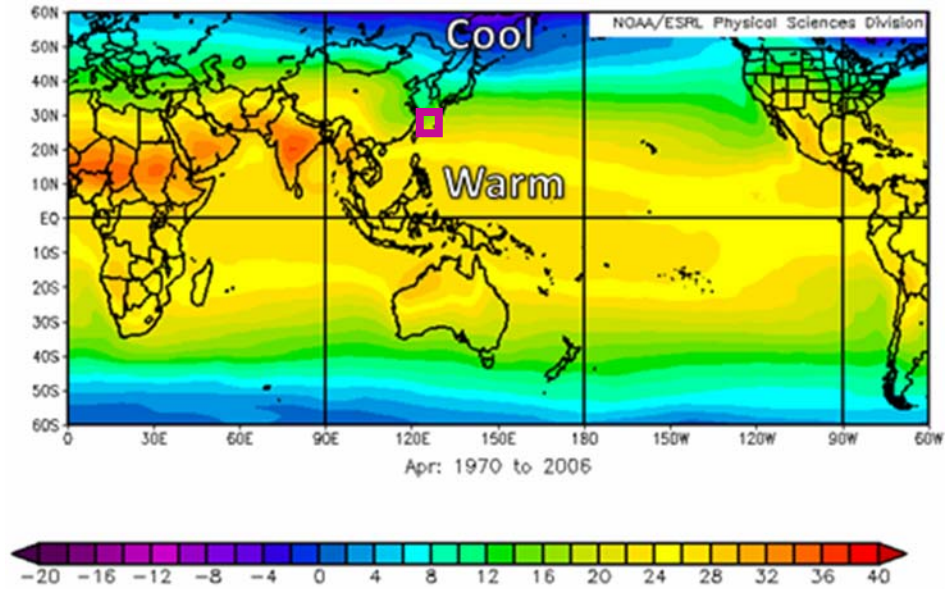


Figure 17. April LTM air temperature ($^{\circ}\text{C}$) at 1000 hPa. When compared to January, April air temperature is greater over the entire WNP AOI (boxed region), with the largest change being over the Sea of Japan and the northern portion of the East China Sea. Basic figure created at ESRL web site (<http://www.cdc.noaa.gov>, accessed May 2009).

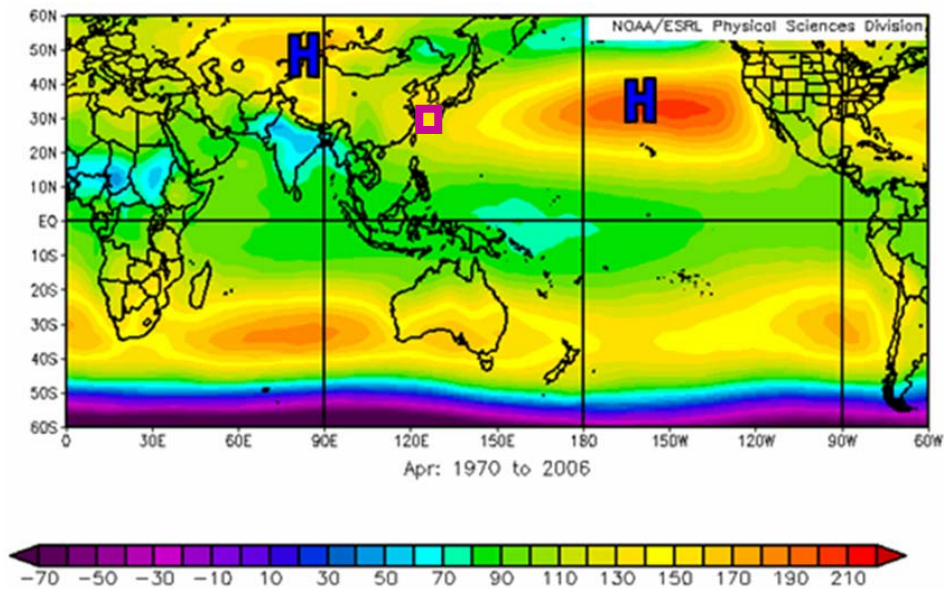


Figure 18. April LTM 1000 hPa geopotential height (m). Winter to spring changes in the WNP AOI (boxed region) are strongly influenced by the weakening of the Asian High and the strengthening of the North Pacific High from January to April. Basic figure created at ESRL web site (<http://www.cdc.noaa.gov>, accessed May 2009).

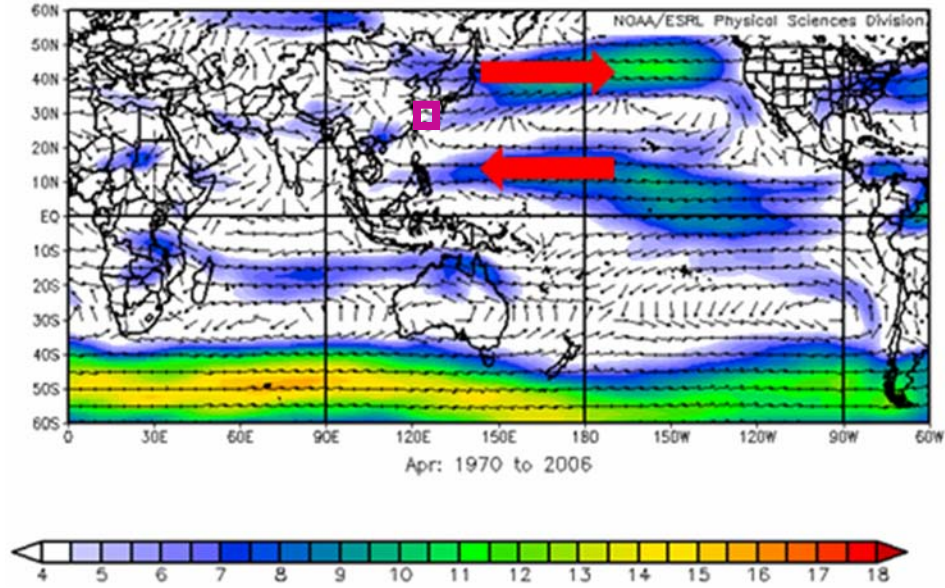


Figure 19. April LTM 850 hPa vector wind (m/s). Note the shift from predominantly northerly winds over much of the WNP AOI (boxed region) in January to westerly and southerly winds in April. Basic figure created at ESRL web site (<http://www.cdc.noaa.gov>, accessed May 2009).

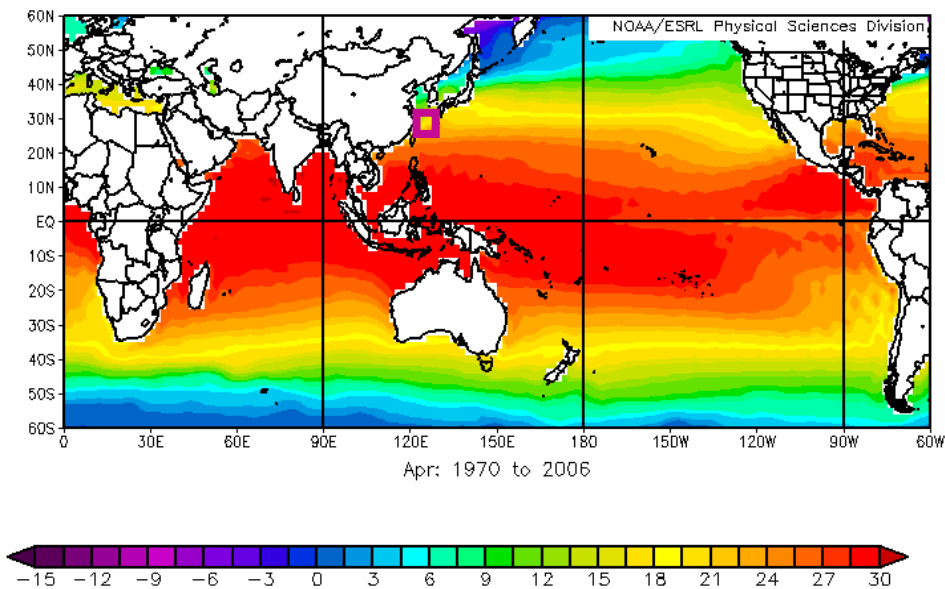


Figure 20. April LTM sea surface temperature (SST; °C). Note the increase in SSTs throughout the entire WNP AOI (boxed region) from January to April. Basic figure created at ESRL web site (<http://www.cdc.noaa.gov>, accessed May 2009).

3. Summer

Figures 21-24 show the July LTM surface air temperature, 1000 hPa geopotential height, 850 hPa winds, and SST for most of the globe and centered on the WNP AOI for this study. The AOI in summer experiences warm moist conditions with: (a) relatively weak temperature gradients; and (b) winds that are generally southerly and weak compared to winter. These conditions are closely linked to seasonal shifts in the intensity and location of the Asian Low, Aleutian Low, and North Pacific High. In particular, the northward retreat of the Aleutian Low, the development of the Asian Low, and the strengthening of the North Pacific High lead to southerly low level winds over the AOI and the advection of warm moist tropical marine air into the AOI.

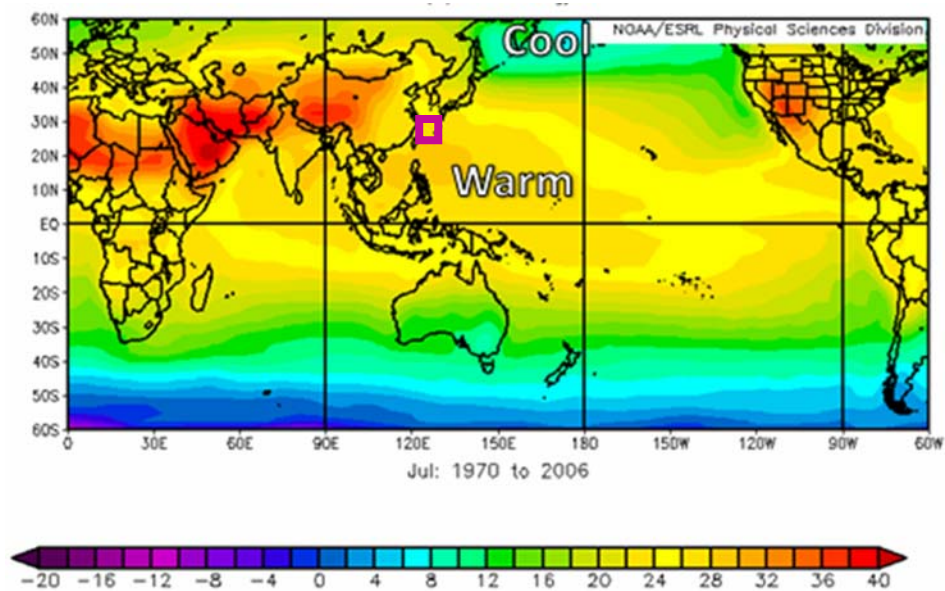


Figure 21. July LTM air temperature (°C) at 1000 hPa. The WNP AOI (boxed region) is dominated by warm, moist air and weaker temperature gradients than in January and April. Basic figure created at ESRL web site (<http://www.cdc.noaa.gov>, accessed May 2009).

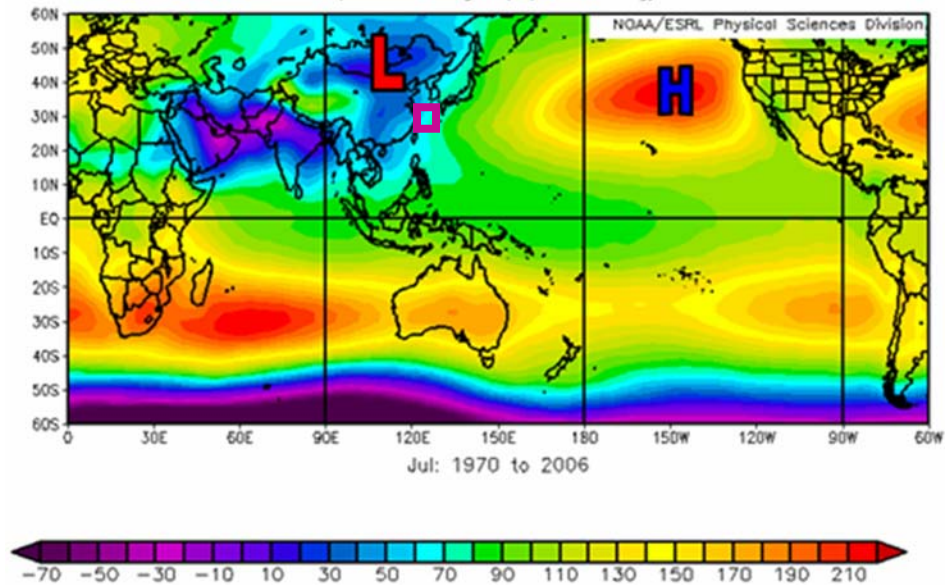


Figure 22. July LTM 1000 hPa geopotential height (m). The dominant geopotential height patterns for the WNP AOI (boxed region) are the Asian Low and North Pacific High which cause mainly southerly flow over most of the AOI. Basic figure created at ESRL web site (<http://www.cdc.noaa.gov>, accessed May 2009).

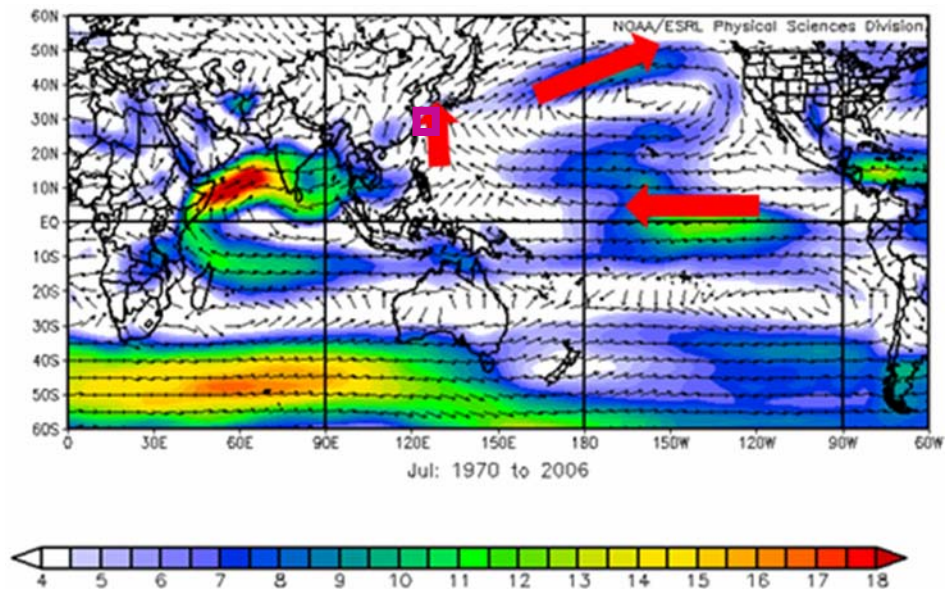


Figure 23. July LTM 850 hPa vector wind (m/s). Winds are predominantly southerly over most of the WNP AOI (boxed region) consistent with advection of warm, moist air into the AOI from the tropics. LTM wind speeds in the AOI during summer tend to be weaker than in the other seasons. Basic figure created at ESRL web site (<http://www.cdc.noaa.gov>, accessed May 2009).

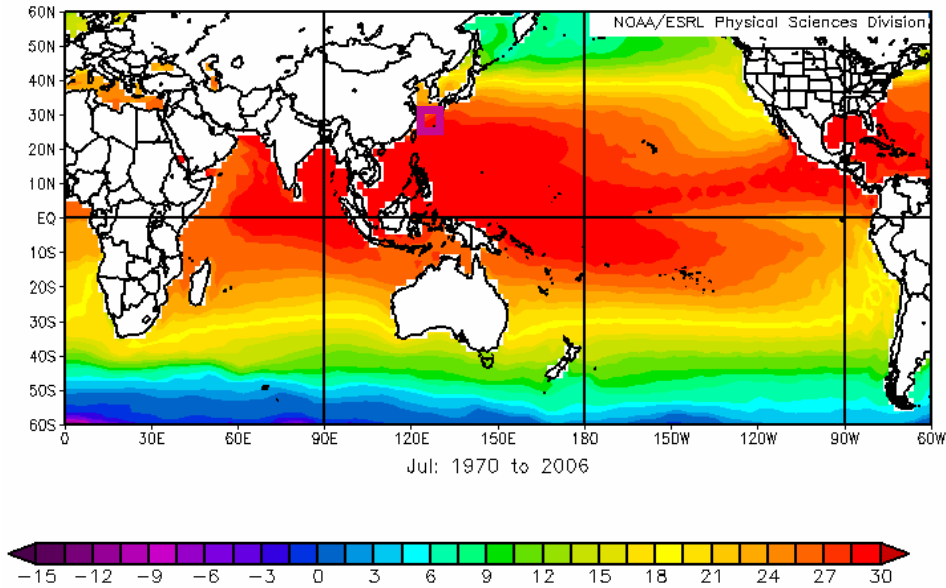


Figure 24. July LTM sea surface temperature (SST; °C). SSTs in the WNP AOI (boxed region) during summer are warmer and warmer than in the other seasons. Basic figure created at ESRL web site (<http://www.cdc.noaa.gov>, accessed May 2009).

4. Fall

Figures 25-28 show the October LTM surface air temperature, 1000 hPa geopotential height, 850 hPa winds, and SST for most of the globe and centered on the WNP AOI for this study. The AOI in fall transitions from warm, moist conditions with relatively weak southerly winds toward the winter conditions show cold, dry, and strong northerly wind conditions of winter (Figures 13-18). There placement of the Asian Low by the developing Asian High, the southward shift and strengthening of the Aleutian Low, and the strengthening and eastward shift of the North Pacific High lead to the onset of northerly low level winds over the AOI and the advection of cool, dry continental air into the AOI.

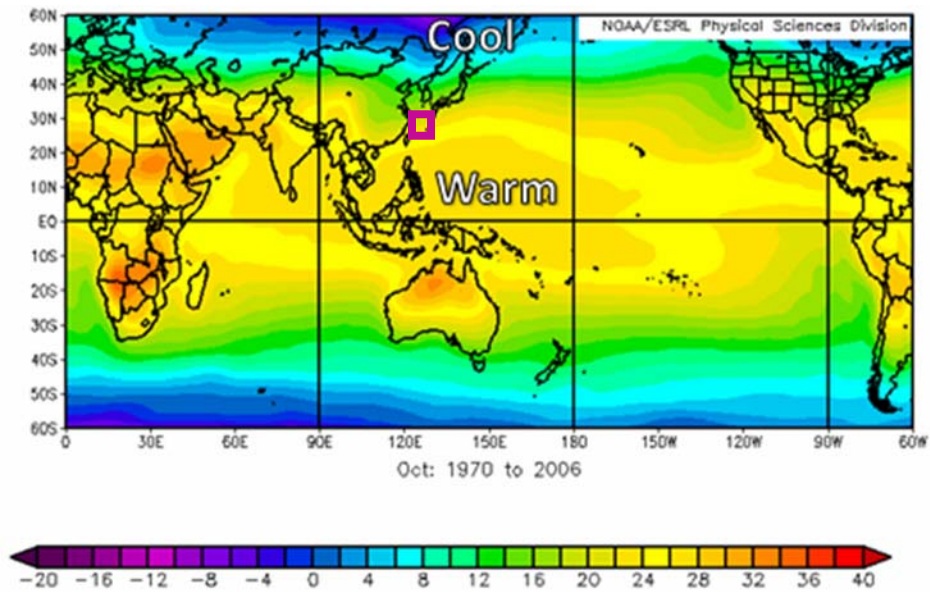


Figure 25. October LTM air temperature ($^{\circ}\text{C}$) at 1000 hPa. Cool low level air temperatures and SSTs develop during fall over East Asia and most of the WNP AOI (boxed region). Basic figure created at ESRL web site (<http://www.cdc.noaa.gov>, accessed May 2009).

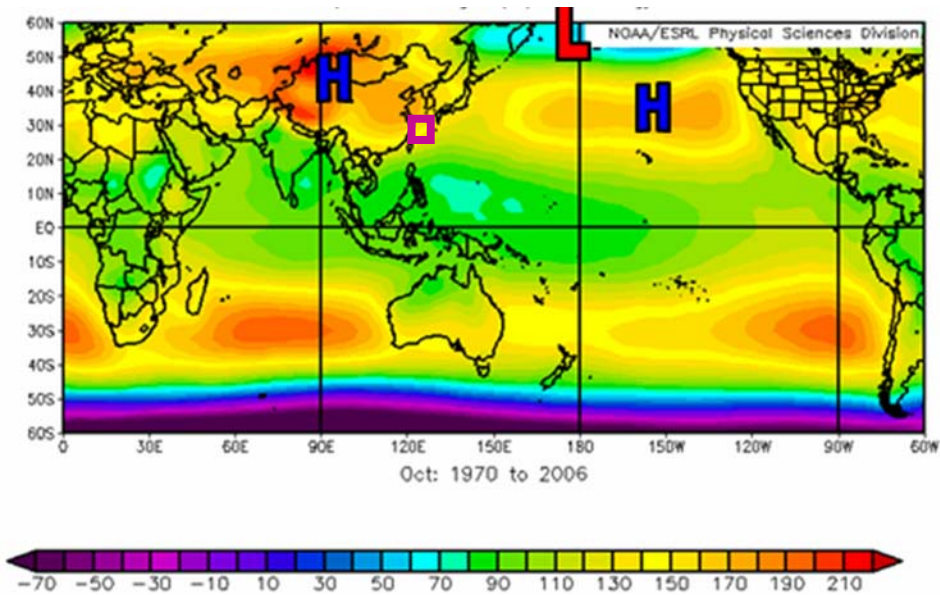


Figure 26. October LTM 1000 hPa geopotential height (m). During fall, the WNP AOI (boxed region) is strongly affected by the development of the Asian High, the southward shift and strengthening of the Aleutian Low, and the weakening and eastward shift of the North Pacific High. Basic figure created at ESRL web site (<http://www.cdc.noaa.gov>, accessed May 2009).

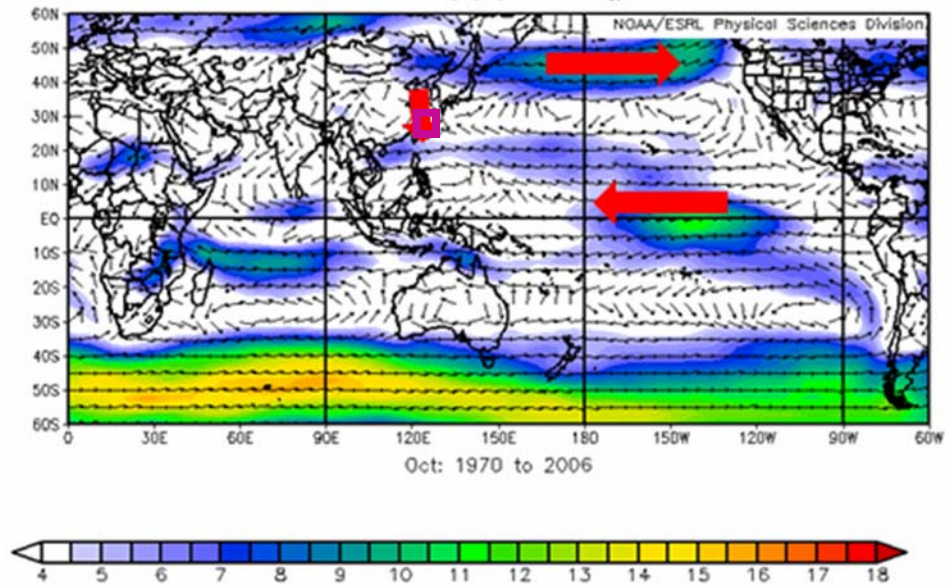


Figure 27. October LTM 850 hPa vector wind (m/s). In fall, the northern (southern) portion of the WNP AOI (boxed region) is dominated by northerly (easterly) low level winds. Basic figure created at ESRL web site (<http://www.cdc.noaa.gov>, accessed May 2009).

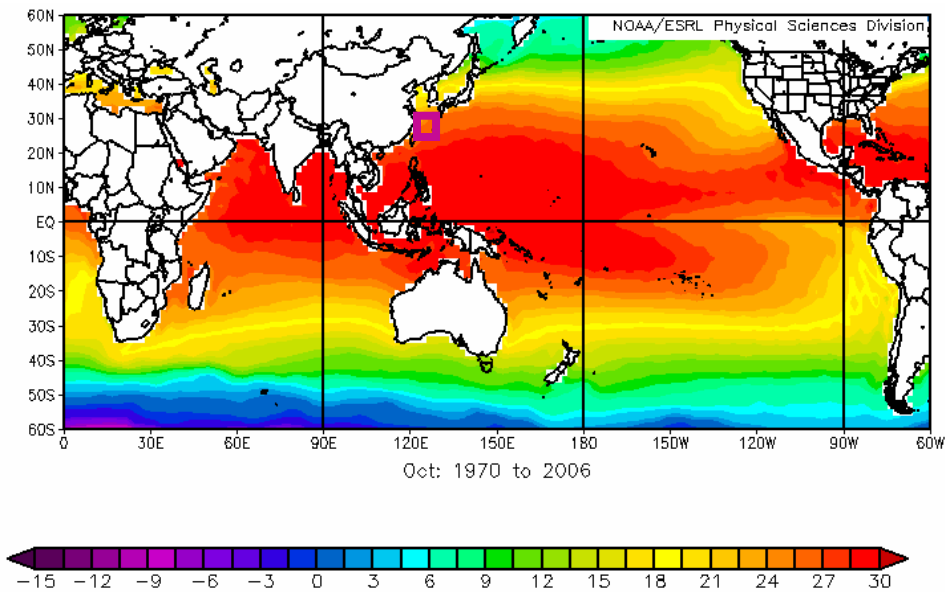


Figure 28. October LTM sea surface temperature (SST; °C). In fall, SSTs over most of the WNP AOI (boxed region) transition from warm summer conditions to cool winter conditions. Basic figure created at ESRL web site (<http://www.cdc.noaa.gov>, accessed May 2009).

B. LONG TERM MEAN SEASONAL CYCLES: EDH AND FACTORS THAT DETERMINE EDH

We also examined the seasonal cycles of EDH and the factors that we used to calculate EDH — air temperature at 2 meters, sea surface temperature, wind speed at 10 meters, and relative humidity at 2 meters — with a focus on the WNP in January, April, July, and October (Figures 29-44). See Chapter I, sections C and D, to review the relationships between EDH and these factors.

1. January

Figure 29 shows the January LTM EDH for the WNP AOI. The overall patterns are: (a) lower EDH close to the cool dry continent, over the East China Sea (ECS) and South China Sea (SCS) where cold dry winds flowing southward away from the Asian High occur, and over colder ocean surfaces in the northern part of the AOI; and (b) higher EDH over warmer ocean surfaces in the southern part of the AOI (cf. Figures 11-16, 29-32). These patterns are consistent overall with the general tendency for high SSTs, cool air, negative ASTD, low relative humidity, and low wind speeds to lead to higher EDHs, and vice versa. For example, note the broad correspondence between low (high) ASTD and low (high) EDH (Figures 29 and 31). For most of the AOI in January, the ASTD is negative, due to the flow of cold continental air over relatively warm SSTs. Thus, we would expect the NPS bulk model to perform relatively well in determining EDHs (see Chapter I, sections C and D).

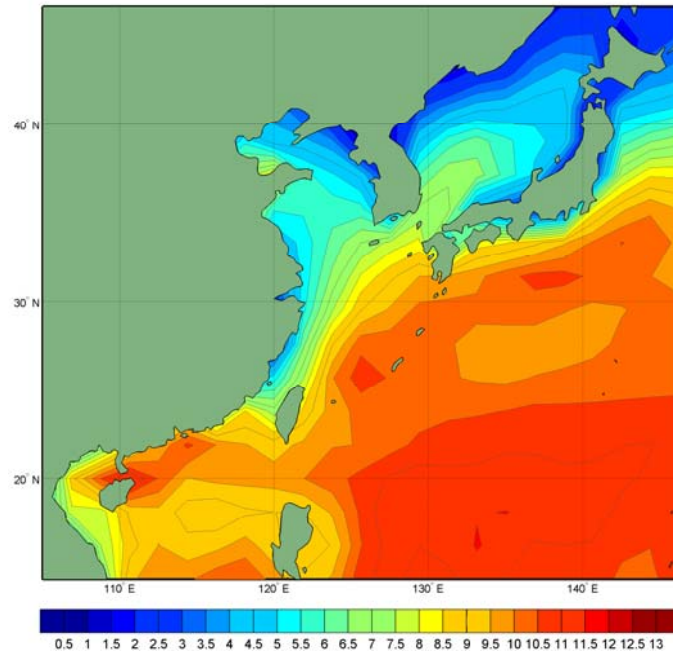


Figure 29. January LTM EDH (m) for the WNP AOI.

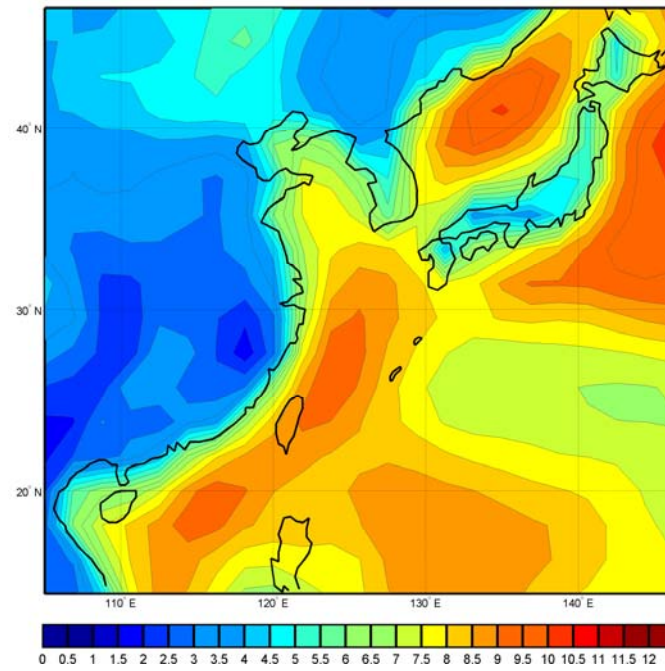


Figure 30. January LTM wind speed (m/s) at 10 meters for WNP AOI.

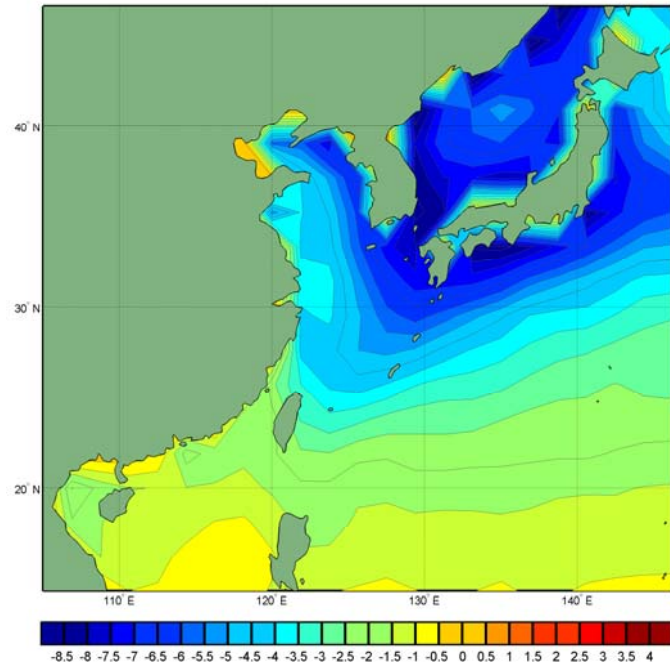


Figure 31. January LTM air-sea temperature difference (°C) for WNP AOI.

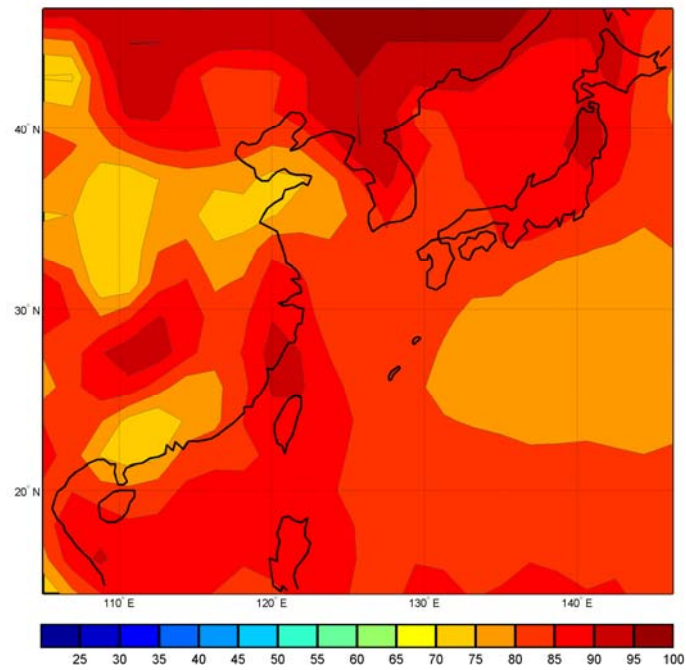


Figure 32. January LTM relative humidity (%) at 2 meters for WNP AOI.

2. April

Figures 33-36 show the April LTM EDH and associated factors. Almost all of the AOI has lower EDHs in April than in January (Figure 33). The main exception is the southern Sea of Japan where the increased EDHs may be attributable to a decrease in humidity and a change from unstable to near-neutral conditions (Figures 35-36). More moisture is present in April than in January over most of the southern ocean region in the AOI (Figure 36), leading to a decrease in the EDH over most of this region compared to January. The EDH maxima over the northeastern portion of the Yellow Sea should be regarded with caution, since it is: (a) associated with strongly positive ASTD and EDH is very sensitivity to ASTD when ASTD is positive; and (b) surrounded on several sides by land and thus may be overly influenced by conditions over the land (see Chapter II, section B).

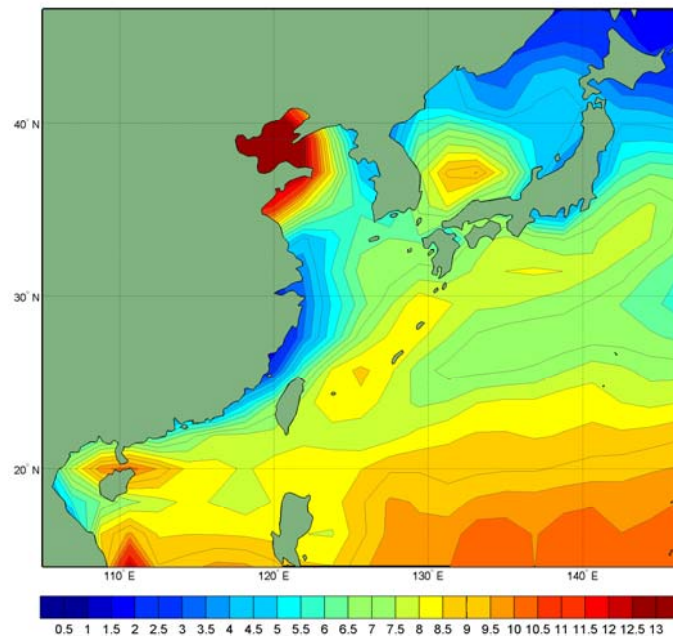


Figure 33. April LTM EDH (m) for the WNP AOI.

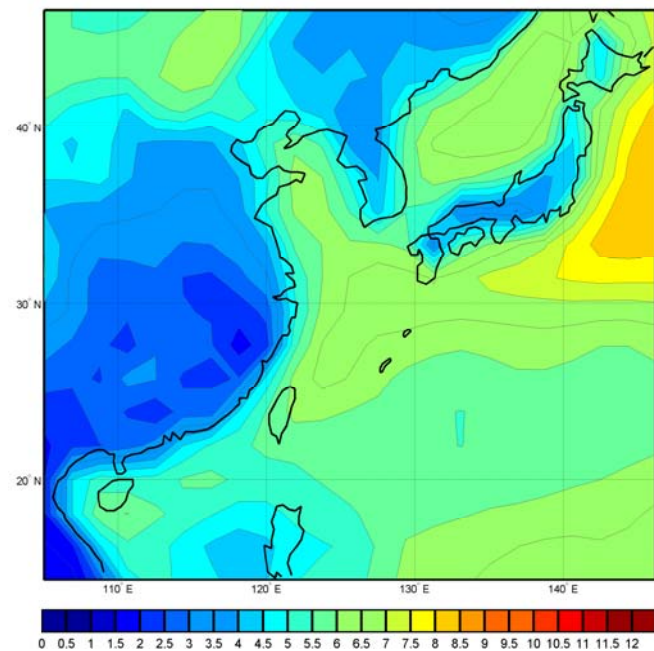


Figure 34. April LTM wind speed (m/s) at 10 meters for WNP AOI.

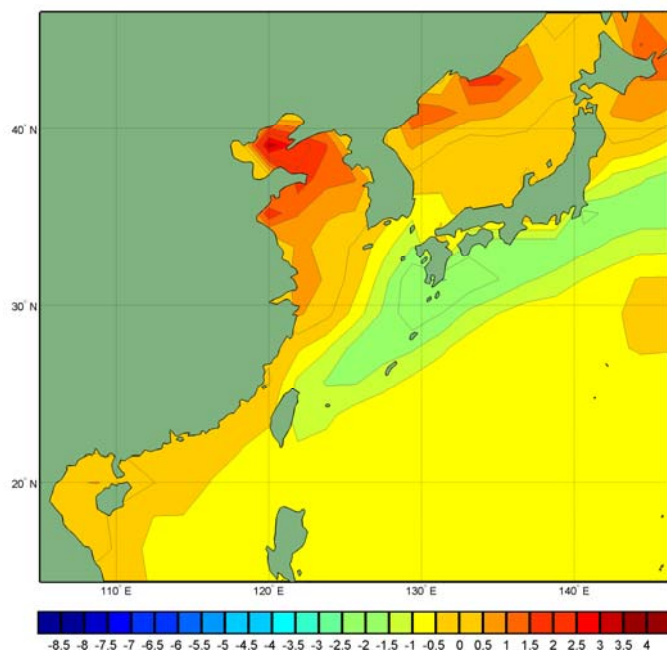


Figure 35. April LTM air-sea temperature difference (°C) for WNP AOI.

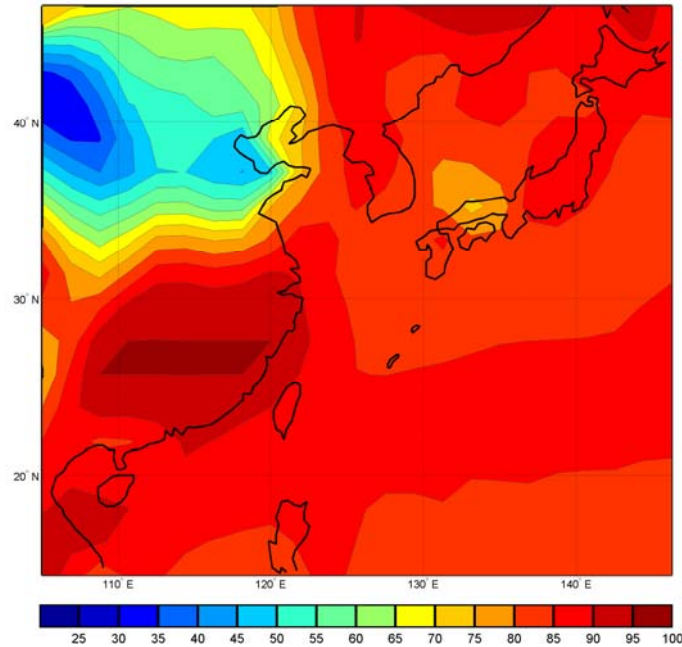


Figure 36. April LTM relative humidity (%) at 2 meters for WNP AOI.

3. July

In July, the WNP AOI is dominated by that the northward advection warm, moist air by relatively weak winds from the tropics (see Figures 21-24, 38, 40). The higher relative humidity combined with near-neutral and weakly stable conditions lead to lower EDHs in the northern latitudes compared to April (Figure 37). Conversely, the lower relative humidity and weakly unstable conditions in the southern latitudes (south of roughly 30°N; Figures 39-40) combine to produce higher EDHs than in April.

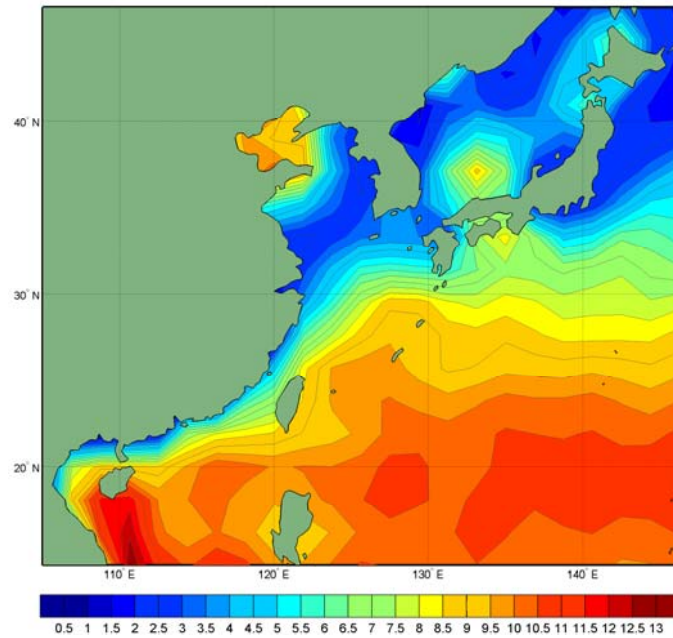


Figure 37. July LTM EDH (m) for the WNP AOI.

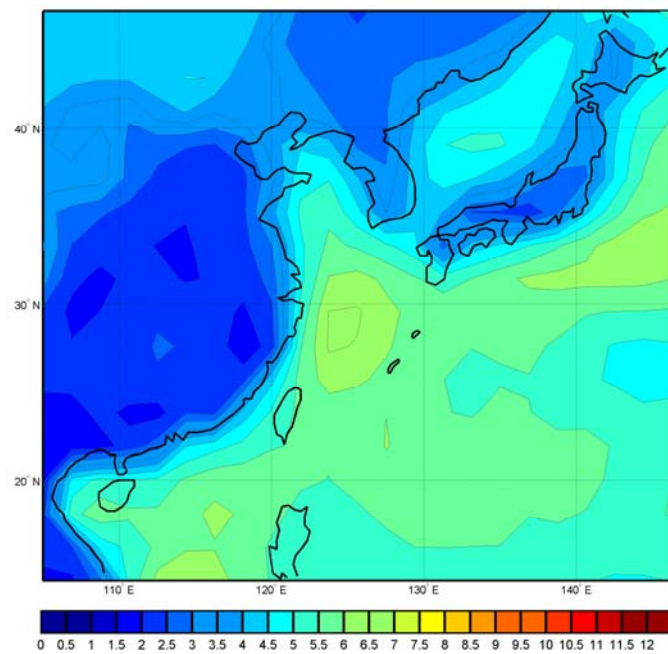


Figure 38. July LTM wind speed (m/s) at 10 meters for WNP AOI.

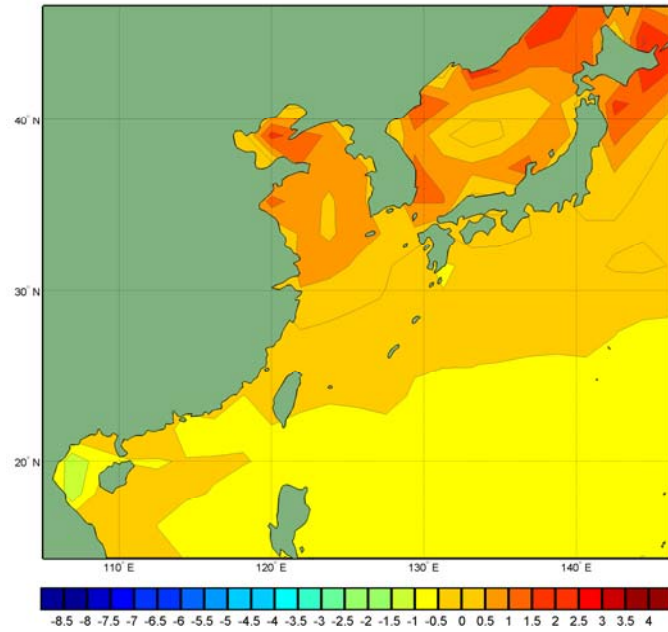


Figure 39. July LTM air-sea temperature difference (°C) for WNP AOI.

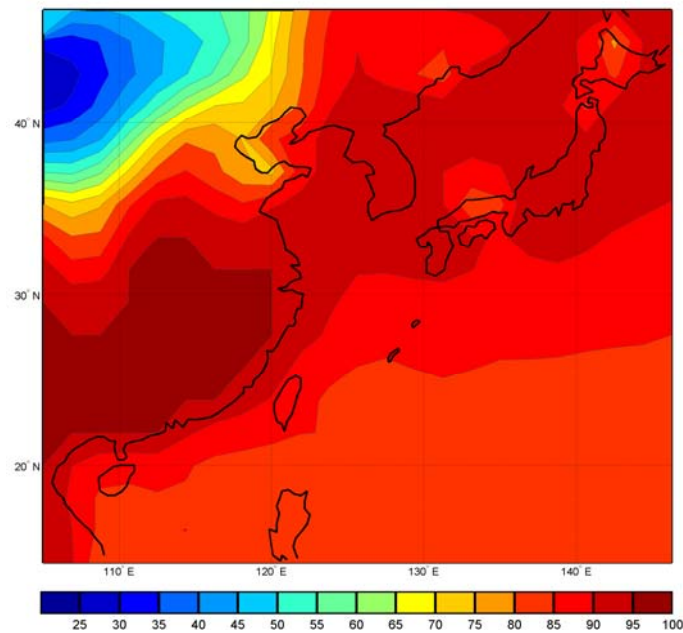


Figure 40. July LTM relative humidity (%) at 2 meters for WNP AOI.

4. October

Figures 41-44 show the October LTM EDH and associated factors. The overall patterns in EDH are broadly similar to those for July, but the range of

EDH values in October is smaller than in July (compare Figures 37, 41). The EDH (Figure 41) shows the influence of the weakening and eastward shift of the North Pacific High, the development of the Asian High, and the onset of strong southward outflows of cold dry air from East Asia and over the Yellow Sea, ECS, and SCS (Figures 25-28, 42, 44). During October, the entire AOI is unstable (negative ASTD, Figure 43). These changes result in increased EDHs in all but the most southern portions (south of roughly 20° N) of the region of interest compared to July (compare Figures 37, 41).

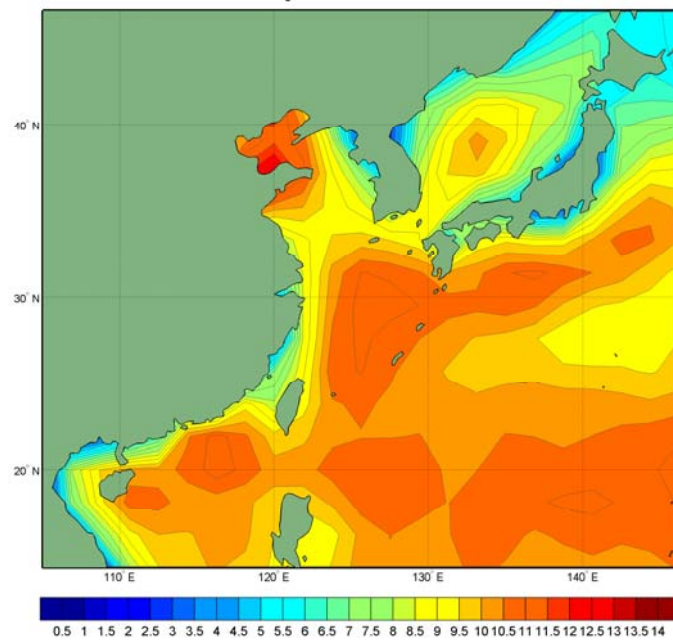


Figure 41. October LTM EDH (m) for the WNP AOI.

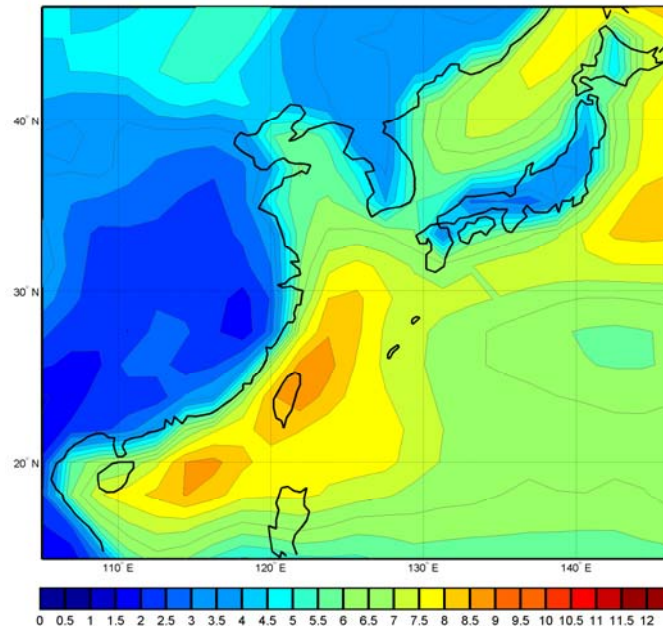


Figure 42. October LTM wind speed (m/s) at 10 meters for WNP AOI.

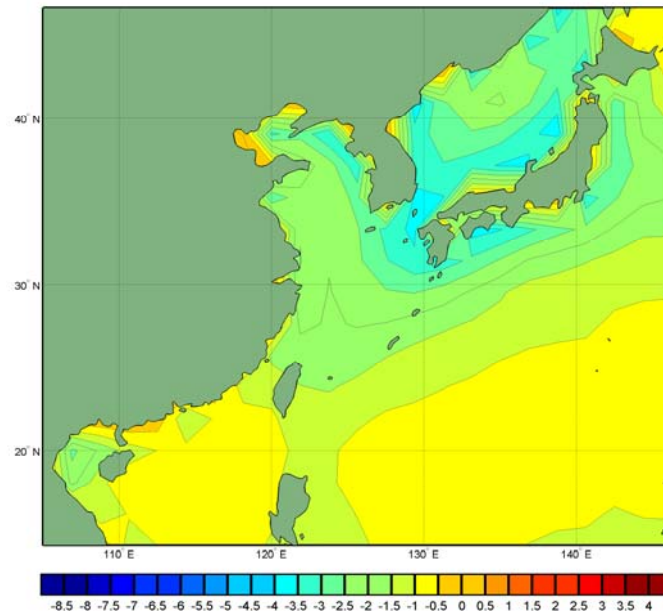


Figure 43. October LTM air-sea temperature difference (°C) for WNP AOI.

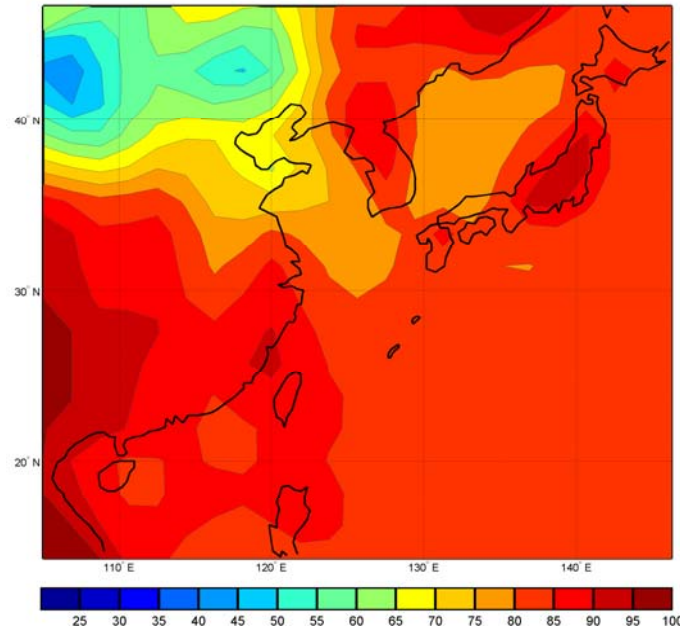


Figure 44. October LTM relative humidity (%) at 2 meters for WNP AOI.

C. LONG TERM MEAN SEASONAL CYCLES: RADAR DETECTION RANGES

To investigate the seasonal cycle of radar detection range in the WNP AOI in an unclassified context, we worked with a generic surface search radar with realistic parameters. This generic radar has a frequency of 9 GHz, is positioned 85 feet above the ocean surface, and is searching for a small target located four feet above the ocean surface and with a detection threshold of 150 dB. The process for calculating RDR is based on the calculation of EDH (see Chapter II, section B). Since RDR is derived from and closely related to EDH, the seasonal cycle of RDR is similar to that of EDH.

Figures 45-48 show the January, April, July, and October LTM RDRs, for the WNP AOI. Note: (a) the general correspondence between high (low) EDH and long (short) RDR (compare Figures 29, 33, 37, and 41 to Figures 45-48); (b) the differences in RDR within the AOI for a given month (e.g., differences on the order of 10 nmi between the Sea of Japan and the Kuroshio region south of Japan in January); and (c) the differences in RDR between months for a given

location within the AOI (e.g., differences on the order of 10 nmi between January and July for the Sea of Japan and the Kuroshio region south of Japan).

The RDR maps shown in Figures 45-48 provide useful guidance for military planners on: (a) the ability to detect adversaries and be detected by adversaries; and (b) managing the opportunities and risks posed by those abilities. However, this guidance is based on long term mean (LTM) conditions and does not account for the climate variations (deviations from LTM conditions) that are known to occur in the WNP (e.g., Figure 5; Ford 2000; Tournay 2007; Turek 2008; Mundhenk 2009). Thus, the RDR differences between locations and between months discussed in the preceding paragraph very likely under-state the spatial and temporal differences that actually occur in the WNP. The impacts of these climate variations on EDH and RDR are discussed in the following section.

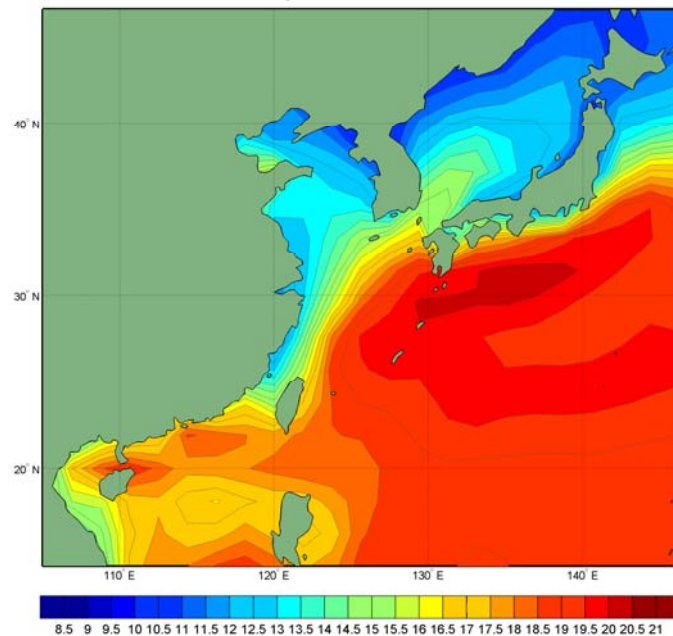


Figure 45. January LTM RDR (nmi) for WNP AOI.

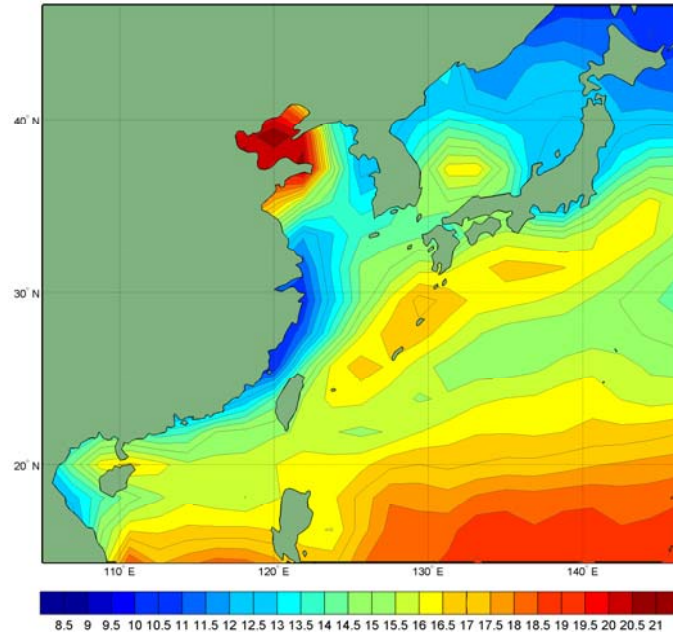


Figure 46. April LTM RDR (nmi) for WNP AOI.

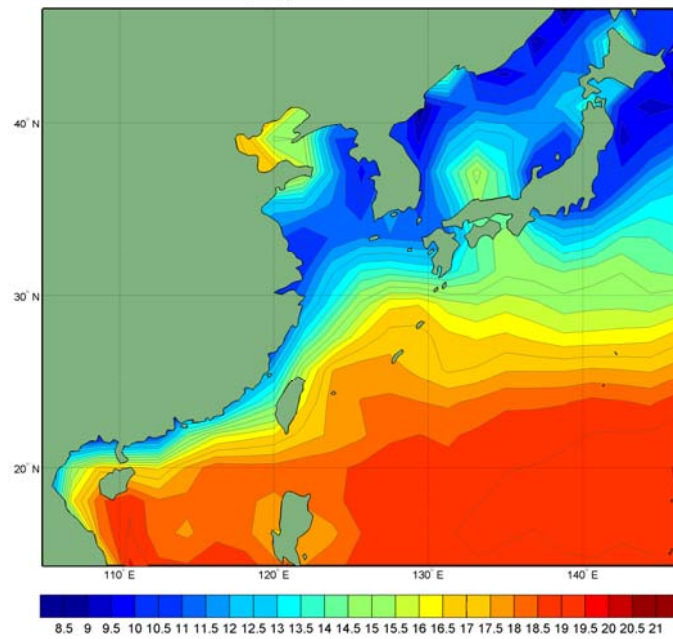


Figure 47. July LTM RDR (nmi) for WNP AOI.

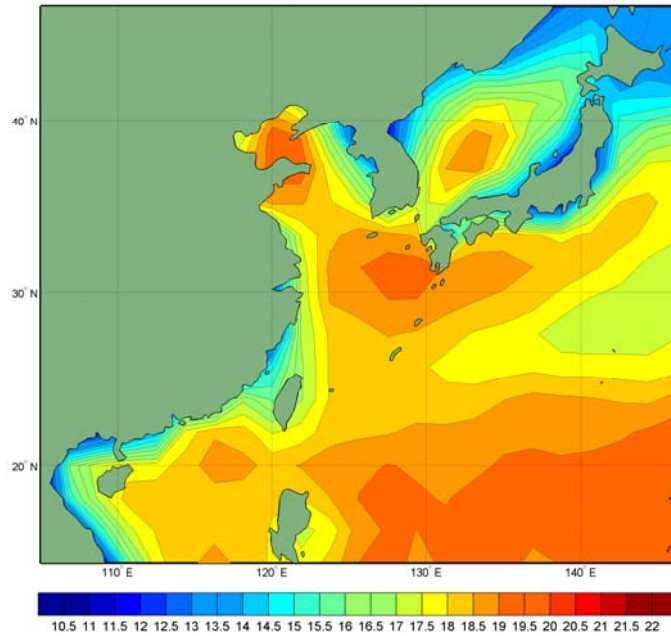


Figure 48. October LTM RDR (nmi) for WNP AOI.

D. OCTOBER CONDITIONAL COMPOSITES

1. Conditional Composites Based on Winds

Wind is a large factor in directly and indirectly determining EDH (see Chapter II, section B.3). Turek (2008) showed that large meridional wind variations occur in the WNP during October and are associated with large variations in SST and implied variations in low level air temperature and relative humidity. We investigated the impacts of these variations by identifying Octobers during 1970-2006 that experienced high and low meridional monthly mean winds in a region east of Taiwan bounded by 20-28°N and 123-128°E (Figures 9, 49-52). We then created conditional composites of meridional wind, EDH, and RDR for the years with the five highest and lowest October mean meridional wind speeds. These conditional composites were then compared and analyzed to see how the variations in the magnitude of the wind, EDH, and RDR are related during high and low wind years.

Figures 49-52 from Turek (2008) show the conditional composite winds and wind anomalies for the October high wind and low wind years. The composites indicate that the high (low) winds are associated with an early (late) transition to winter conditions in the ECS, SCS, and Ryuku Islands regions (see Figures 25-28, 41-44). This is especially evident in the anomalies (Figures 51-52) which in these regions show anomalously strong (weak) northeasterly winds in the high (low) wind composite. The conditional composites of the five Octobers during 1970-2006 with the highest (longest) and lowest (shortest) monthly mean EDH (RDR) in the region east of Taiwan bounded by 20-28°N and 123-128°E are shown in Appendix A. The wind, EDH, and RDR conditional composites are useful indicators of the extremes that planners may need to prepare for when operating in the WNP. However, conditional composites do not by themselves indicate the conditions that are most likely for a given period in the future (e.g., for an upcoming October). But the likely conditions can be determined from a long range forecasts (LRFs) generated using information about the past occurrences represented by conditional composites — for example, LRFs that use data from past occurrences of high wind events to predict future high wind events.

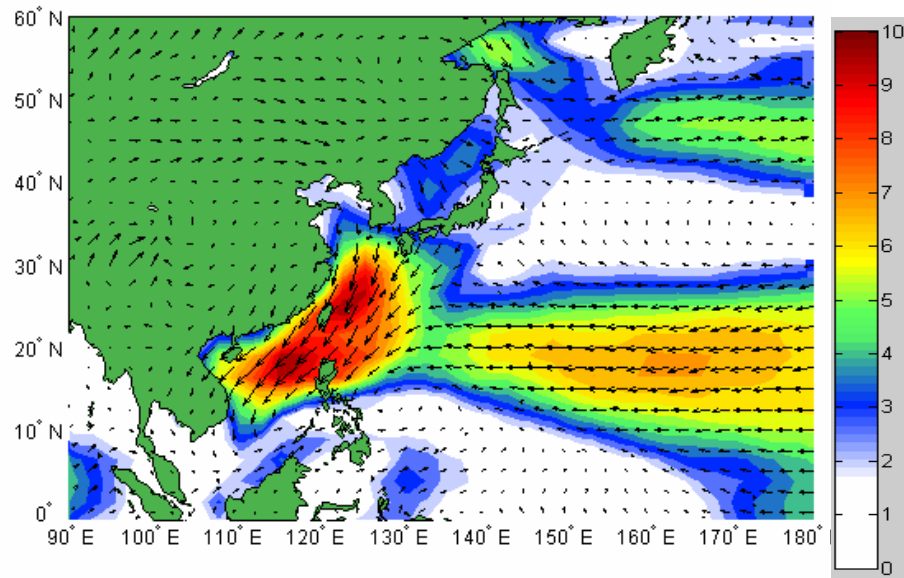


Figure 49. October conditional composite of surface winds for the five years with the highest meridional wind speeds averaged over 20-28°N, 123-128°E (area east of Taiwan shown in Figure 9). From Turek (2008).

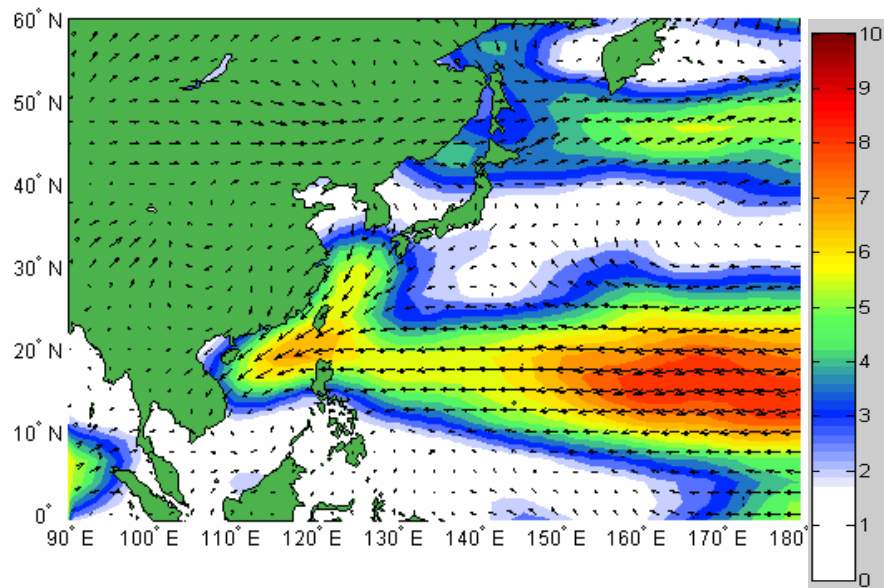


Figure 50. October conditional composite of surface winds for the five years with the lowest meridional wind speeds averaged over 20-28°N, 123-128°E (area east of Taiwan shown in Figure 9). From Turek (2008).

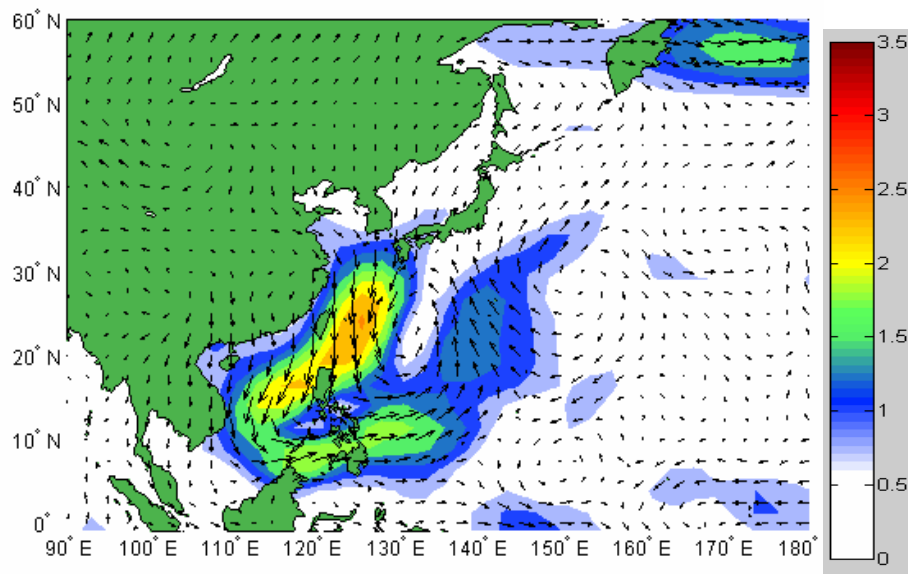


Figure 51. October conditional composite anomaly of surface winds for the five years with the highest meridional wind speeds averaged over 20-28°N, 123-128°E (area east of Taiwan shown in Figure 9). From Turek (2008).

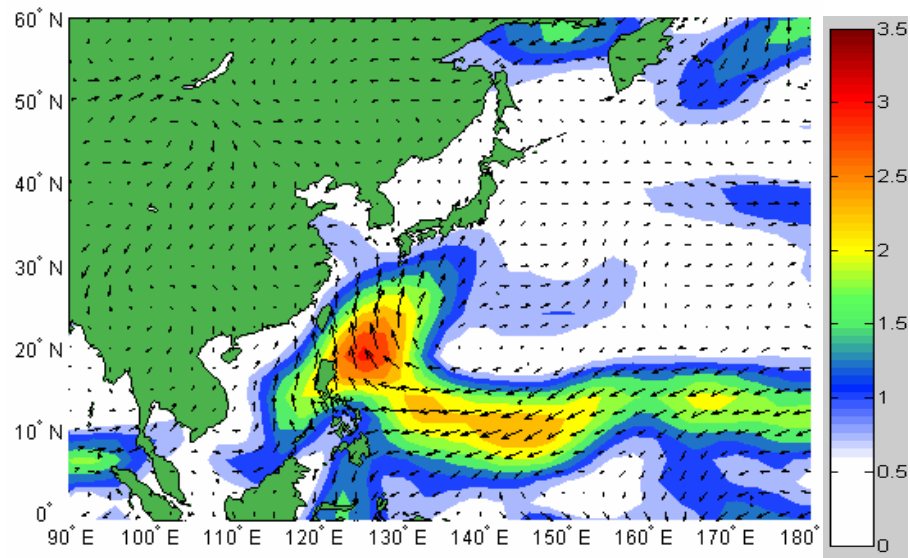


Figure 52. October conditional composite anomaly of surface winds for the five years with the lowest meridional wind speeds averaged over 20-28°N, 123-128°E (area east of Taiwan shown in Figure 9). From Turek (2008).

E. DEVELOPMENT OF LONG RANGE FORECAST PROCESS

U. S. Navy planners often begin preparing for an operation or exercise at lead times of up to four months and their decisions can benefit greatly by having accurate long range guidance on the expected environmental conditions and the resulting impacts on sensor and weapons systems performance. The statistical long range forecast methods used in this study require reliable predictors. We experimented with using indices of El Nino – La Nina (ENLN) as predictors but found relatively low correlations with our predictands, meridional wind, EDH, RDR in our WNP AOI focus region east of Taiwan (see Figure 9). So we then searched for other potential predictors by correlating the predictands with numerous atmospheric and oceanic variables. We found that all three predictands were well correlated with equatorial SST near the dateline (in the western half of the Nino 4.0 box, 5°S-5°N, 160°E-175°W) when the SST lead the predictands by zero to five months. This indicated that this SST could be a useful long range predictor. Prior studies indicate that this SST is a physically plausible predictor and likely influences the WNP AOI by altering equatorial Pacific atmospheric convection, which leads to anomalous Rossby wave activity that then alters the circulation in the WNP AOI (e.g., Ford 2000; Tournay 2007).

Figures 55-59 show maps of the correlations for 1970-2006 of monthly mean October RDR in the focus region east of Taiwan (purple box) with global monthly mean SST, with SST leading by zero to four months. Correlation magnitudes of 0.318 or greater indicate significance at the 95% confidence level (see Chapter II, section B.2). The red box on the equator near the dateline in each correlation map indicates a region of high correlation at all lead times (e.g., correlations with October RDRs in the WNP focus region of 0.60, 0.55, 0.50, 0.50, and 0.35 for SST in October, September, August, July, and June, respectively).

Figures 53-57 show broad scale correlation patterns that are similar to SST anomaly patterns for ENLN (e.g., Ford 2000; Schwing et al. 2002). This

suggests that the processes that cause climate variations in the WNP, including RDR variations, are physically plausible and related to ENLN — for example, that EN (LN) related positive SST anomalies in the central and eastern equatorial Pacific during June-October tend to be associated with positive (negative) RDR anomalies in the WNP in October. However, the details of the correlation patterns indicate that the relationship to ENLN is strongest for equatorial SSTs near the dateline (red box in Figures 53-57), on the far western edge of the central and eastern equatorial Pacific region where EN and LN related SST anomalies tend to be strongest. So the relationships to ENLN are notable but not especially robust.

Similar maps (not shown) were constructed for correlations between meridional wind and EDH in the WNP focus region with SST, and for correlations of all three WNP predictands with other potential predictors (e.g., air temperature, geopotential height, etc.). However, the correlations with the equatorial SST near the dateline tended to be the highest overall for zero to four-month lead times. All the correlations had similar spatial patterns and were physically consistent (e.g., SST was positively (negatively) correlated with RDR and EDH and high (low) wind speeds). These results support the conclusion that the correlations are physically plausible and represent real physical processes.

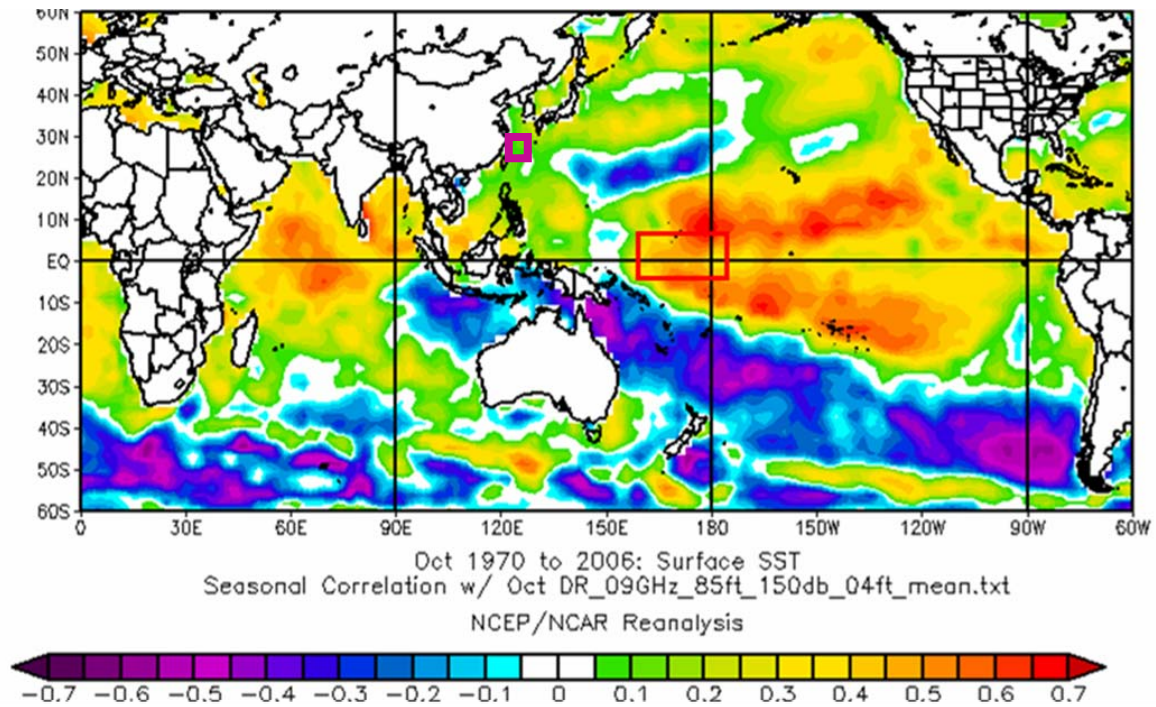


Figure 53. Correlation of October radar detection range (RDR) in the focus region east of Taiwan (purple box) with SST in October for the years 1970-2006. The RDR is for a 9 GHz radar at 85 ft above the surface, looking for a 4 ft target with a detection threshold of 150 dB. The red box highlights a region of persistently high correlations when SST leads October RDR by zero to five months (see Figures 55-59). Basic figure created at ESRL web site (<http://www.cdc.noaa.gov>, accessed May 2009).

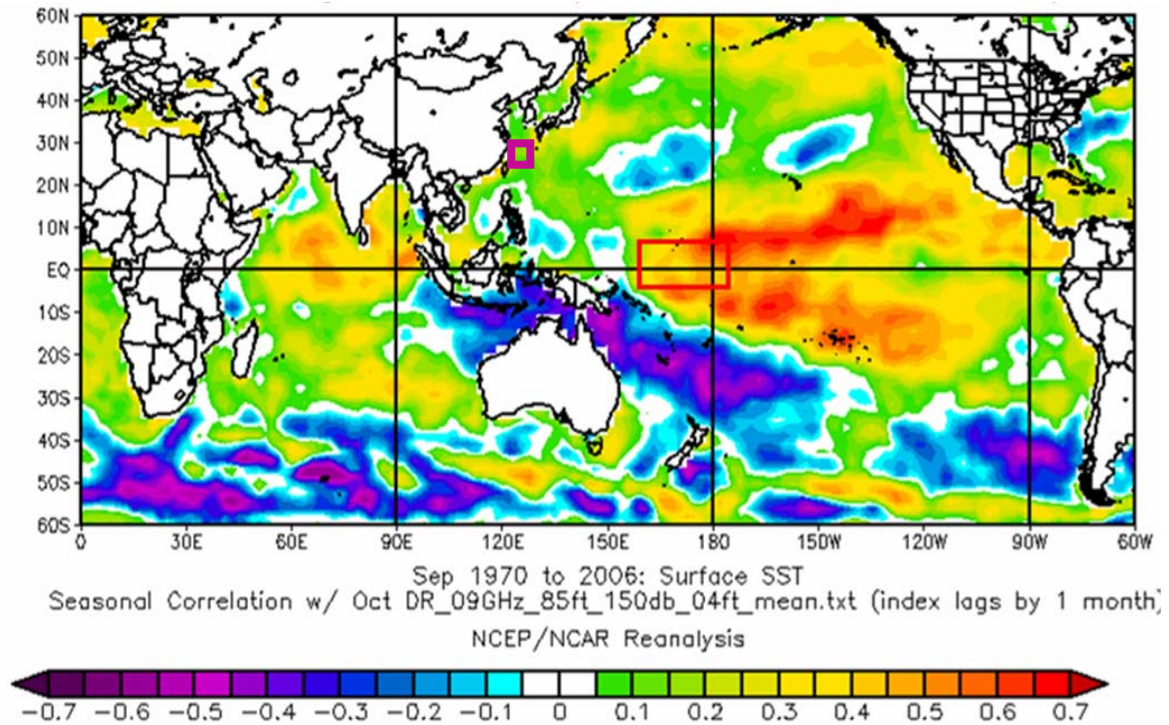


Figure 54. Correlation of October radar detection range (RDR) in the focus region east of Taiwan (purple box) with SST in September for the years 1970-2006. The RDR is for a 9 GHz radar at 85 ft above the surface, looking for a 4 ft target with a detection threshold of 150 dB. The red box highlights a region of persistently high correlations when SST leads October RDR by zero to five months (see Figures 55-59). Basic figure created at ESRL web site (<http://www.cdc.noaa.gov>, accessed May 2009).

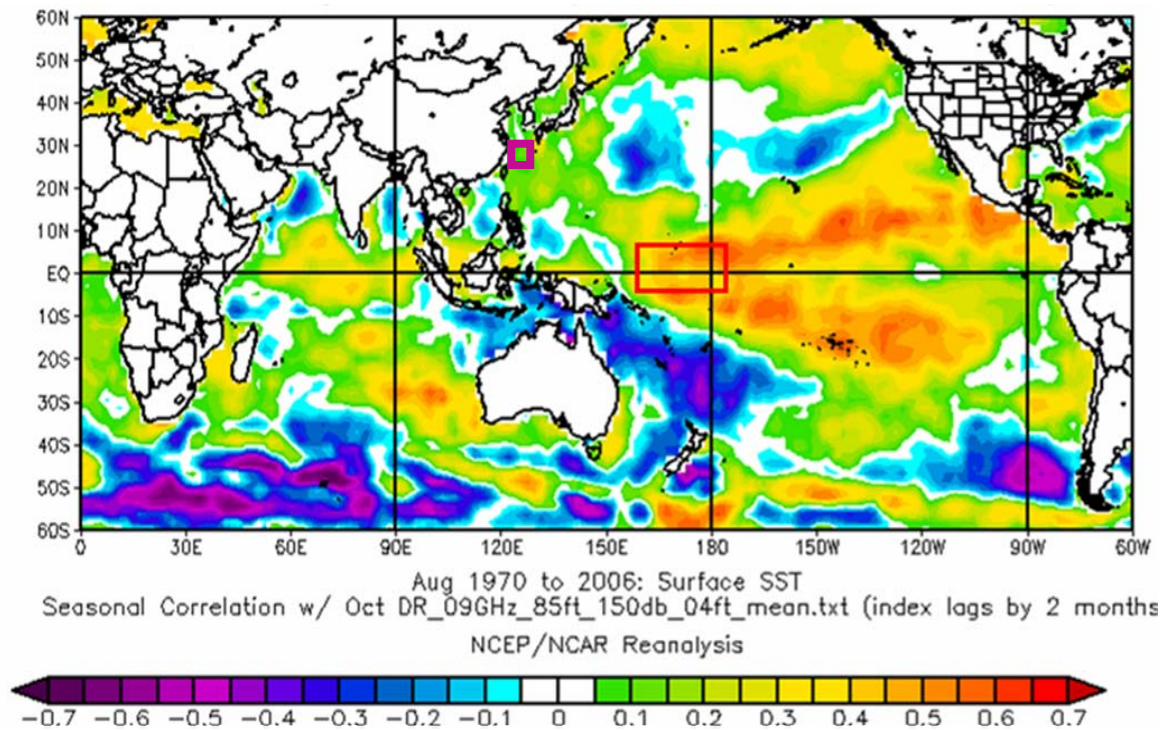


Figure 55. Correlation of October radar detection range (RDR) in the focus region east of Taiwan (purple box) with SST in August for the years 1970-2006. The RDR is for a 9 GHz radar at 85 ft above the surface, looking for a 4 ft target with a detection threshold of 150 dB. The red box highlights a region of persistently high correlations when SST leads October RDR by zero to five months (see Figures 55-59). Basic figure created at ESRL web site (<http://www.cdc.noaa.gov>, accessed May 2009).

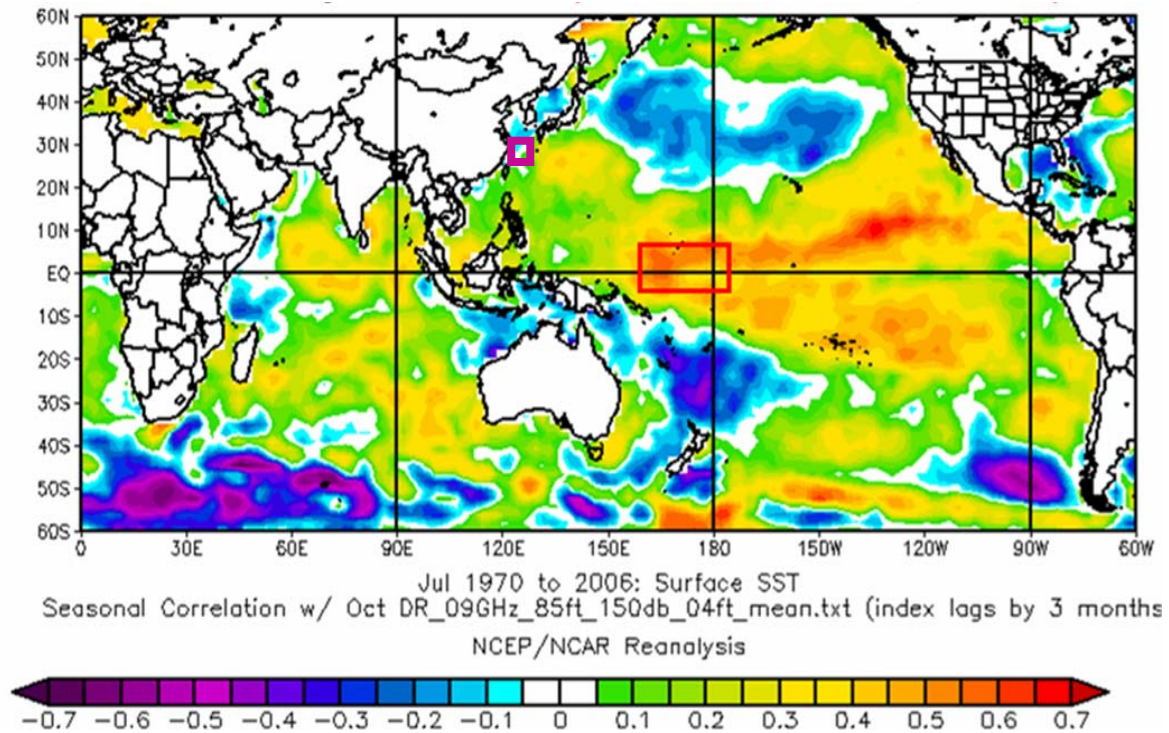


Figure 56. Correlation of October radar detection range (RDR) in the focus region east of Taiwan (purple box) with SST in July for the years 1970-2006. The RDR is for a 9 GHz radar at 85 ft above the surface, looking for a 4 ft target with a detection threshold of 150 dB. The red box highlights a region of persistently high correlations when SST leads October RDR by zero to five months (see Figures 55-59). Basic figure created at ESRL web site (<http://www.cdc.noaa.gov>, accessed May 2009).

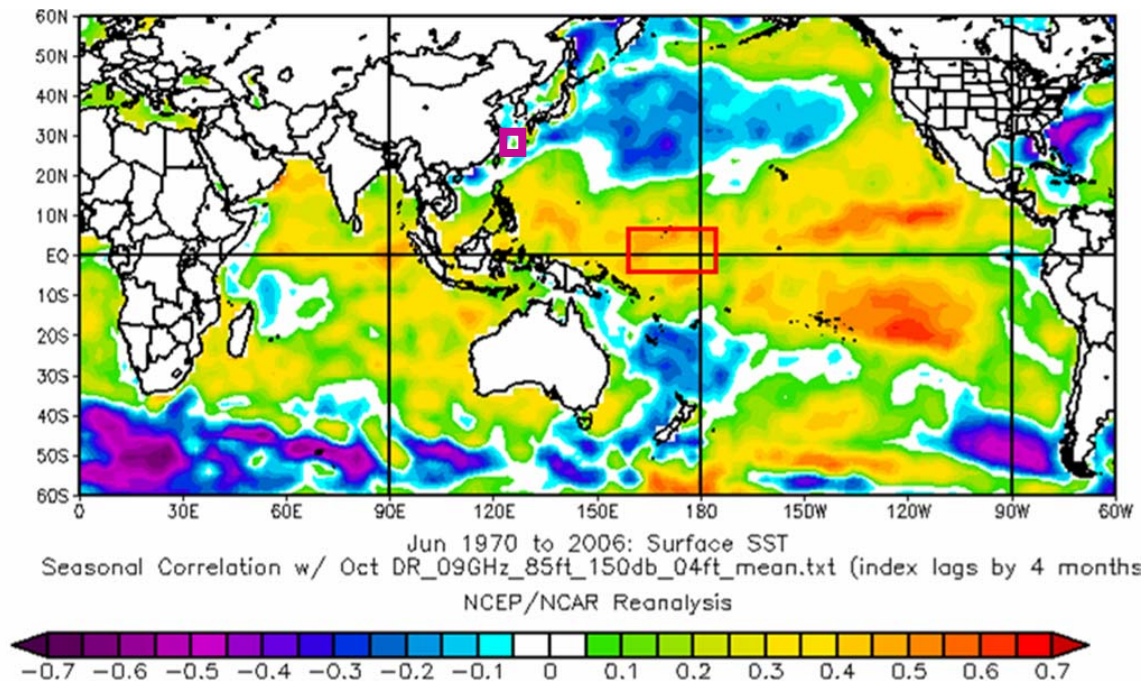


Figure 57. Correlation of October radar detection range (RDR) in the focus region east of Taiwan (purple box) with SST in June for the years 1970-2006. The RDR is for a 9 GHz radar at 85 ft above the surface, looking for a 4 ft target with a detection threshold of 150 dB. The red box highlights a region of persistently high correlations when SST leads October RDR by zero to five months (see Figures 55-59). Basic figure created at ESRL web site (<http://www.cdc.noaa.gov>, accessed May 2009).

F. HINDCASTS AND HINDCAST VERIFICATION METRICS

Hindcasts of the WNP predictands (meridional wind, EDH, and RDR) in October of 1970-2006 were calculated using the methods described in Chapter II, section B.3 and verified using the methods described in Chapter II, section B.4. The lead times ranged from zero to four months (e.g., hindcasts issued in June through September and valid in the following October). Figures 58-60 present representative samples of the hindcast verification metrics. For example, Figure 58 shows verification metrics for hindcasts of above normal (high tercile) meridional wind speeds in October in the WNP focus region. Note the relatively high percent correct, probability of detection, threat score, and Heidke skill score values, plus the low false alarm values, at all lead times. The best scores occur

at one month lead times, perhaps because lags in the dynamical processes that links the SST predictor to the meridonal wind predictand mean that the link is less apparent when there is no lag (i.e., when the lead time is zero). This relative high scores at the longer lead times is clear evidence that skillful long range forecasts of WNP meridional winds, and the closely related EDH and RDR, could be made up to lead times of 5 months with greater skill than that of traditional climatology.

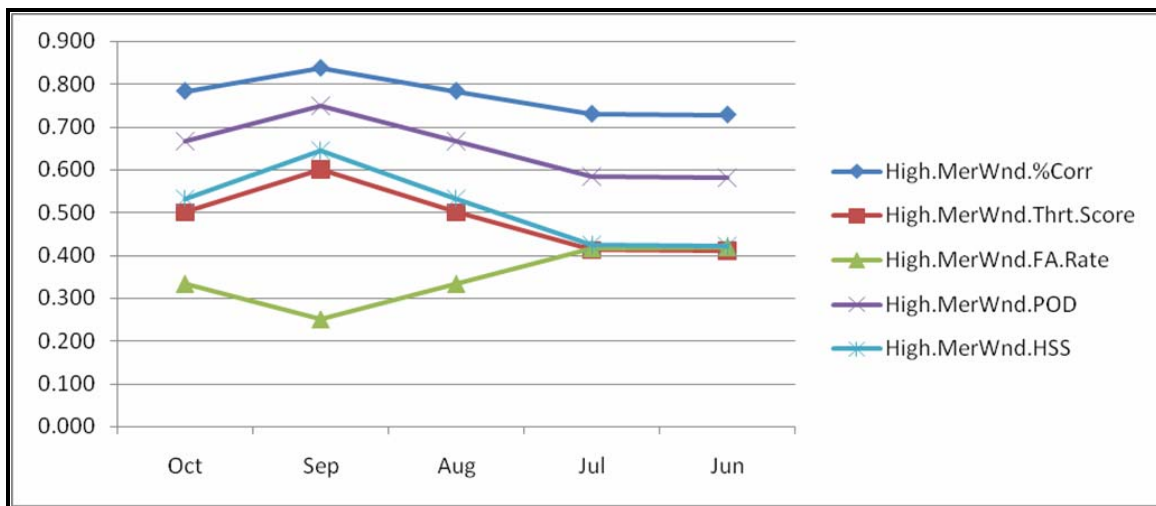


Figure 58. Verification metrics for hindcasts for 1970-2006 of above normal (i.e., high) meridonal wind in October in the WNP focus region using eqatorial SST near the dateline in October, September, August, July, and June as the predictor. The hindcast methods, and the metrics and metrics legend acronyms are explained in Chapter II, section B. See text for additional details.

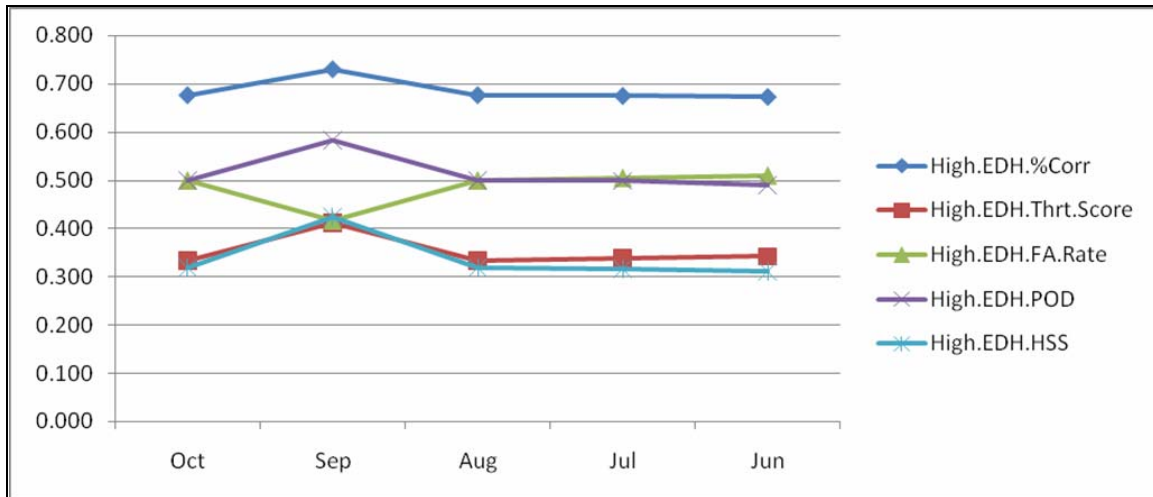


Figure 59. Verification metrics for hindcasts for 1970-2006 of above normal (i.e., high) EDH in October in the WNP focus region using eqatorial SST near the dateline in October, September, August, July, and June as the predictor. The hindcast methods, and the metrics and metrics legend acronyms are explained in Chapter II, section B. See text for additonal details.

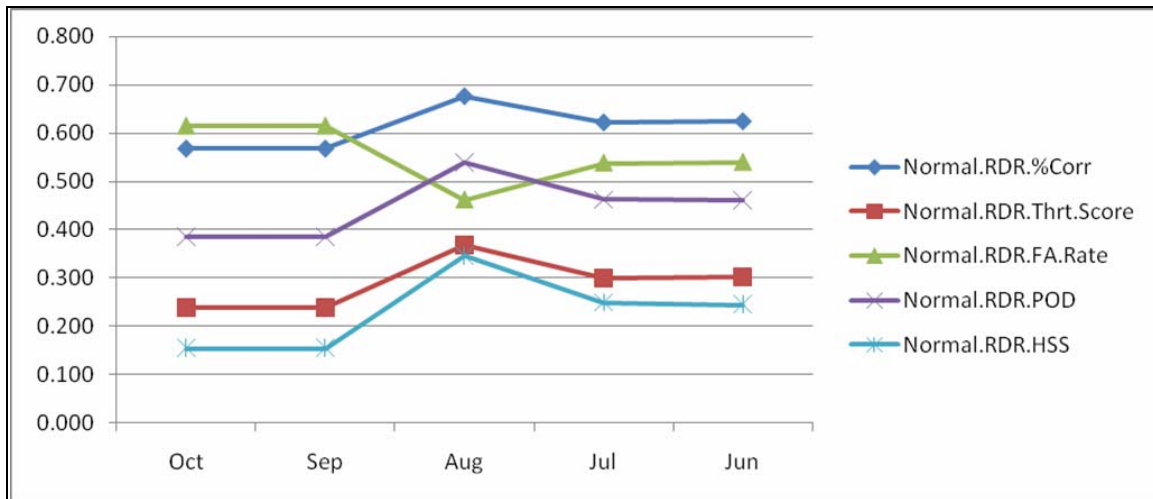


Figure 60. Verification metrics for hindcasts for 1970-2006 of near normal RDR in October in the WNP focus region using eqatorial SST near the dateline in October, September, August, July, and June as the predictor. The hindcast methods, and the metrics and metrics legend acronyms are explained in Chapter II, section B. See text for additonal details.

G. SMART CLIMATOLOGY VERSUS TRADITIONAL U. S. MILITARY CLIMATOLOGY

The U. S. military is lagging civilian agencies in providing state-of-the-science climatology support (see Chapter I). The U. S. military needs to improve upon this situation in order to provide more accurate and useful products to warfighters for mission planning purposes. Our results and those from prior studies (e.g., Twigg 2007; Turek 2008) clearly indicate state –of-the-science data and methods can produce climate support products that are more skillful than those produced using traditional climatology data and methods. Figure 61 shows an example of a product from the present evaporation duct climatology used by the U. S. Navy. This data is only provided in tabular form and contains information on only the EDH and only for one particular Marsden square. Clearly, it would be difficult for warfighters to correctly interpret this information and make improved tactical decisions using this table alone. The data used to produce the present evaporation duct climatology was generated from raw ICOADS data from 1970-1984, and uses the outdated Paulus-Jeske bulk model from the 1970s to produce a climatology of EDH with a 10° spatial resolution that is available only in monthly long term mean tabular and histogram form. Other shortcomings in this EDH climatology are described in Chapter I.

We plotted the data shown in Figure 61 to produce a map view of the present Navy climatology of EDH (Figure 62). Figure 63 shows an example of the corresponding state-of-the-science, or smart, climatology of EDH based on the methods described in Chapters II and II. A visual comparison of Figures 62 and 63 shows that the smart climatology: (a) has very different overall spatial patterns; (b) has much more spatial detail due to its much higher spatial resolution (1.85 degrees versus 10 degrees); and (c) has much lower EDH values, mainly due to shortcomings in the PJ model used to calculate the Navy EDH climatology. The existing navy EDH climatology also suffers from very limited temporal resolution; it provides only one set of LTM values for each month and thus cannot describe variations from the LTM conditions. Modern multi-

decadal reanalysis data sets provide much higher temporal resolution and the ability to develop LRF products such as those described in Chapter III, sections D-F).

	EVAPORATION DUCT OCCURRENCE (%)									
	Jan Day / Nite	Feb Day / Nite	Mar Day / Nite	Apr Day / Nite	May Day / Nite	Jun Day / Nite	Jul Day / Nite	Aug Day / Nite	Sep Day / Nite	
0-2m	.3 / .3	.4 / .1	.2 / .1	.4 / .3	.2 / .1	.4 / .2	1.2 / 1.1	1.4 / .5	.3 / .5	
2-4m	.1 / .1	.2 / .6	.4 / .6	.3 / .3	.2 / .6	.3 / .7	.4 / .7	.3 / .6	.2 / .5	
4-6m	1.2 / 1.7	.7 / 1.9	1.4 / 3.8	1.3 / 5.6	.7 / 3.3	.2 / 1.2	.9 / 1.7	.6 / 2.3	1.1 / 2.3	
6-8m	1.5 / 3.4	2.3 / 2.7	2.5 / 7.2	6.0 / 10.2	3.4 / 8.2	1.3 / 2.0	1.6 / 3.0	1.4 / 2.9	2.4 / 5.9	
8-10m	2.8 / 6.1	2.1 / 5.6	4.4 / 7.0	6.1 / 9.6	5.8 / 6.2	1.8 / 3.2	1.8 / 2.8	2.7 / 4.6	3.4 / 8.6	
10-12m	5.3 / 9.1	4.8 / 10.6	6.6 / 9.8	7.3 / 12.3	6.0 / 9.3	3.6 / 5.7	3.0 / 4.3	4.5 / 8.4	5.6 / 13.1	
12-14m	7.1 / 11.0	8.8 / 15.5	10.3 / 18.4	10.2 / 16.3	7.9 / 13.6	5.1 / 9.2	5.6 / 9.7	6.7 / 14.8	10.5 / 19.8	
14-16m	8.8 / 14.7	12.6 / 14.4	14.7 / 18.0	12.0 / 15.7	11.6 / 15.2	6.7 / 10.8	7.2 / 11.7	9.3 / 14.4	13.5 / 19.4	
16-18m	11.5 / 16.7	14.4 / 17.2	15.3 / 15.5	18.2 / 12.1	14.8 / 14.4	10.8 / 12.6	8.2 / 15.4	11.5 / 15.4	16.1 / 13.6	
18-20m	14.5 / 13.4	13.4 / 13.2	14.1 / 8.6	11.4 / 7.8	12.9 / 9.4	10.2 / 14.8	11.2 / 12.4	12.6 / 13.4	14.7 / 8.6	
20-22m	12.3 / 9.9	14.1 / 9.4	10.9 / 5.2	9.7 / 4.0	10.4 / 7.4	11.5 / 11.2	11.6 / 12.7	13.8 / 10.1	11.6 / 3.5	
22-24m	12.3 / 6.4	10.1 / 4.8	7.5 / 2.6	7.9 / 2.6	10.0 / 5.1	11.3 / 10.1	11.8 / 9.2	12.4 / 7.7	8.9 / 2.0	
24-26m	8.6 / 4.1	8.6 / 2.1	4.8 / 2.0	3.8 / 1.7	6.5 / 3.3	11.0 / 8.3	13.2 / 7.8	9.1 / 3.0	4.8 / 1.7	
26-28m	6.8 / 1.9	4.5 / 1.0	3.0 / .6	3.4 / .8	4.5 / 1.9	8.3 / 4.6	9.2 / 4.2	6.4 / .8	3.3 / .3	
28-30m	4.0 / .7	1.8 / .4	1.9 / .2	1.2 / .4	2.7 / 1.2	6.7 / 2.2	6.2 / 1.9	4.1 / .5	2.0 / .0	
30-32m	1.2 / .3	.5 / .2	.7 / .2	.3 / .1	1.1 / .5	5.0 / 1.5	3.6 / 1.0	1.4 / .4	1.0 / .0	
32-34m	1.1 / .2	.5 / .0	.6 / .2	.3 / .0	.6 / .1	2.6 / .7	1.9 / .4	.9 / .0	.2 / .0	
34-36m	.3 / .1	.2 / .2	.4 / .1	.1 / .0	.3 / .0	1.7 / .4	.8 / .0	.4 / .0	.1 / .0	
36-38m	.2 / .0	.1 / .0	.1 / .1	.0 / .1	.3 / .0	.6 / .0	.4 / .0	.3 / .0	.1 / .0	
38-40m	.2 / .0	.0 / .0	.2 / .0	.1 / .0	.1 / .1	.6 / .1	.3 / .1	.1 / .1	.1 / .0	
> 40m	.2 / .0	.0 / .0	.0 / .0	.1 / .0	.0 / .0	.4 / .3	.0 / .0	.3 / .0	.0 / .0	
Undef	.0 / .0	.0 / .0	.0 / .0	.0 / .0	.0 / .0	.0 / .0	.0 / .0	.0 / .0	.0 / .0	
=====										
	Jan Day / Nite	Feb Day / Nite	Mar Day / Nite	Apr Day / Nite	May Day / Nite	Jun Day / Nite	Jul Day / Nite	Aug Day / Nite	Sep Day / Nite	
Mean Duct Height (m)	19.5 / 16.4	18.5 / 15.7	17.4 / 14.4	16.6 / 13.5	18.1 / 15.3	21.7 / 18.6	21.0 / 17.9	19.6 / 16.1	17.7 / 13.9	
Mean Wind Speed (m/s)	5.9 / 5.2	5.3 / 4.9	4.2 / 3.8	3.4 / 3.1	4.6 / 4.3	8.7 / 7.8	8.6 / 7.9	7.7 / 7.0	5.4 / 4.8	

Figure 61. October LTM evaporation duct height (EDH) example of the present U. S. Navy LTM EDH climatology in tabular format.

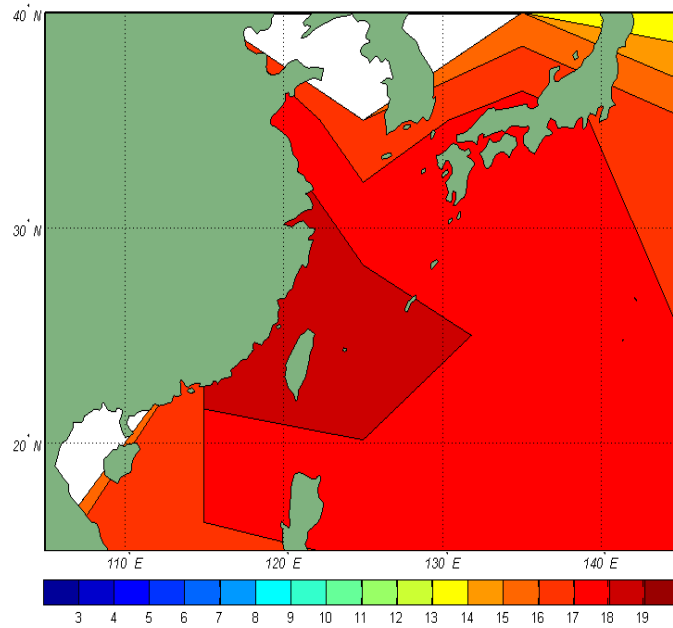


Figure 62. October LTM evaporation duct height (EDH) example of the present U. S. Navy LTM EDH climatology, after we manually entered and then plotted the data shown in Figure 61.

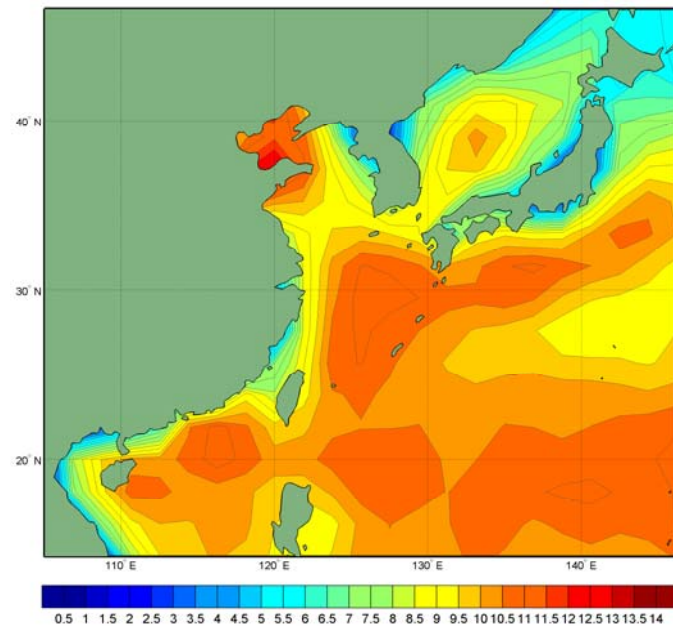


Figure 63. October LTM evaporation duct height (EDH) example of applying modern climate data sets and methods to develop a state-of-the-science EDH climatology. Note the large differences between this modern EDH climatology and the present Navy climatology (Figure 61-62).

These comparisons are just some of the many examples of how existing military climatologies fall well short of the accuracy, spatial and temporal resolutions, predictive capabilities, and usability that are possible using modern climatology data sets and methods. When the U. S. military decides to seriously pursue the development and production of modern climate analyses and long range forecasts, then warfighters will begin receiving the long lead support they need — for example, the best available long lead radar performance predictions.

H. LONG RANGE FORECASTS OF EDH AND RDR

We applied our long range forecasting methodology (see Chapter II, section B), and the lessons learned from our hindcasts (see Chapter III, section F) to produce long range forecasts (LRFs) of the evaporation duct height and radar detection ranges in the WNP for November 2009. These LRFs are classified and can be found in the classified Appendix B of this thesis. This appendix is available in the classified section of the Dudley Knox Library of the Naval Postgraduate School in Monterey, California.

IV. SUMMARY, CONCLUSIONS, AND RECOMMENDATIONS

A. SUMMARY AND CONCLUSIONS

We developed and tested a method for producing long range forecasts (LRFs) of winds, evaporation duct height, and radar detection range in the western North Pacific (WNP). The method shows a high potential for producing skillful operational LRFs that would significantly improve long lead support for the planning of military operations in the WNP. In particular, such support would have important applications in planning naval operations such as radar detection and tracking of submarine periscopes, low-flying missiles and aircraft, and surface combatants. We provided examples of the use of state-of-the-science data sets and methods for developing more accurate and useful climatologies, climate analyses, and LRFs of atmospheric electromagnetic propagation and radar performance for the WNP and with a focus on October. But the same basic data sets and methods can be used for many other climate and operational variables (e.g., sonic layer depth and sonar detection ranges), other locations, and other periods. We also created classified long range forecasts of environmental conditions and radar performance in the WNP in November 2009. These LRFs were developed to support the planning of naval operations that will be conducted in November 2009. The LRFs will be verified in early 2010. These LRFs can be found in the classified section of the Dudley Knox Library at the Naval Postgraduate School located in Monterey, CA.

One of several limitations of our research is that in some coastal locations the reanalysis data used to represent conditions over the ocean may be overly influenced by data from land locations (see Chapter II, section B.1). Thus, EDH and RDR results for such locations points should be viewed with caution. One additional limitation is that our radar detection ranges are based only on the

evaporation duct and do not account for surface-based ducts. The operational significance of this shortcoming and methods for correcting it need to be studied in the future.

B. RECOMMENDATIONS FOR FUTURE RESEARCH

We recommend that research similar to ours be conducted in the near future when higher resolution reanalysis data sets become available. A reanalysis data set with higher horizontal and vertical resolution would: (a) reduce the coastal problems discussed in Chapter II, section B.1; and (b) provide an increased number of levels below 700 mb which would allow for better mapping of both surface based ducts and evaporation ducts. By the end of 2009, NCEP is expected to release a global coupled atmospheric-oceanic reanalysis with a 0.25° by 0.25° horizontal resolution for the ocean and 0.5° by 0.5° horizontal resolution for the atmosphere. We recommend that future research investigate the use of this and other forthcoming higher resolution reanalysis data sets.

Predictors were selected by computing correlations between potential predictors and the predictands. We used sea surface temperatures as our predictor, but additional potential predictors and sets of predictors should be researched in the future. In addition, other statistical and statistical-dynamical LRF methods should be investigated, such as the composite analysis forecasting method (Hanson 2007; Moss 2007).

Future research should investigate methods for producing independent data sets for verifying reanalysis variables, and analyses and LRFs of EDH and RDR. This might be accomplished using long term buoy observations (cf. Twigg 2007) or analyses of ducts and radar performance based on field experiments in the WNP.

Smart climatology for military applications is presently done mainly by DoD climate researchers. Their prototype operational products should be

applied in future research and development efforts to test these products in operational planning and to assess the value of those products to the military planning process.

THIS PAGE INTENTIONALLY LEFT BLANK

APPENDIX

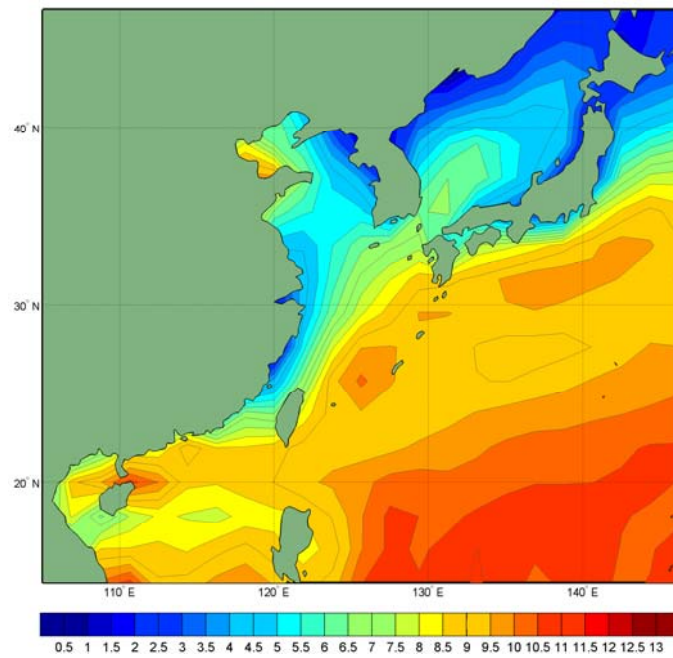


Figure 64. February LTM EDH (m) for the WNP AOI.

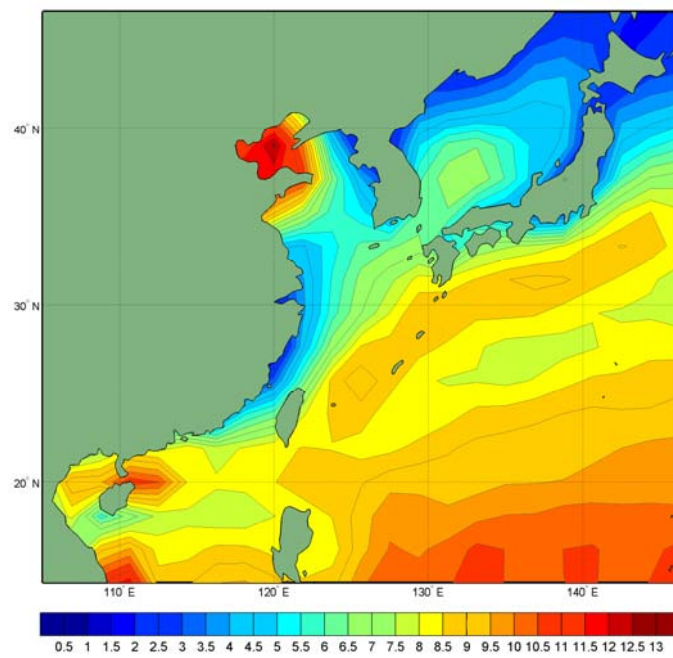


Figure 65. March LTM EDH (m) for the WNP AOI.

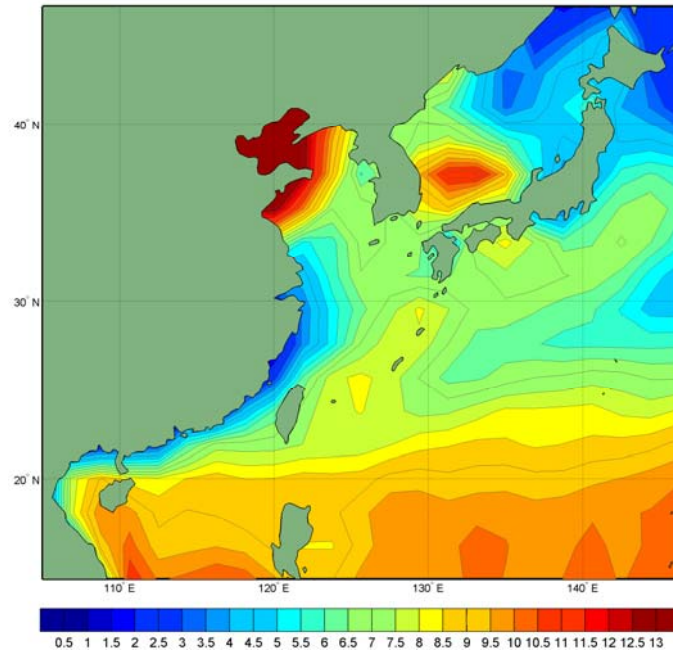


Figure 66. May LTM EDH (m) for the WNP AOI.

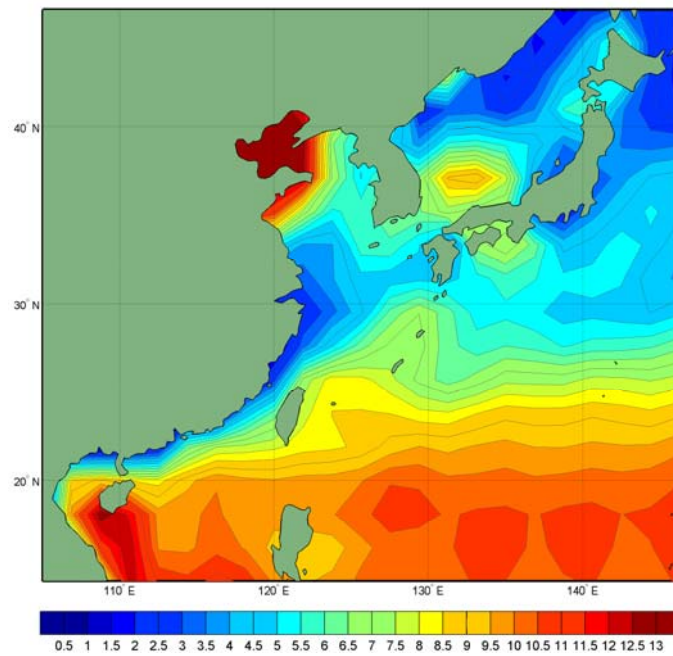


Figure 67. June LTM EDH (m) for the WNP AOI.

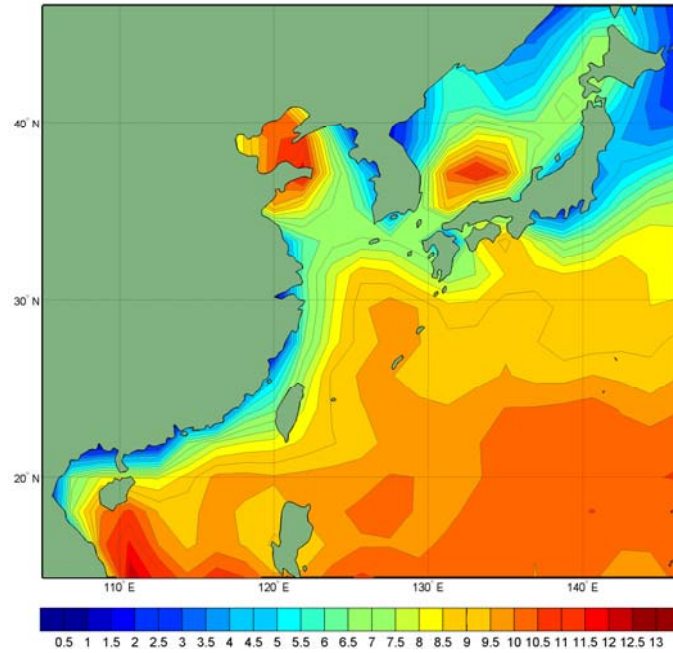


Figure 68. August LTM EDH (m) for the WNP AOI.

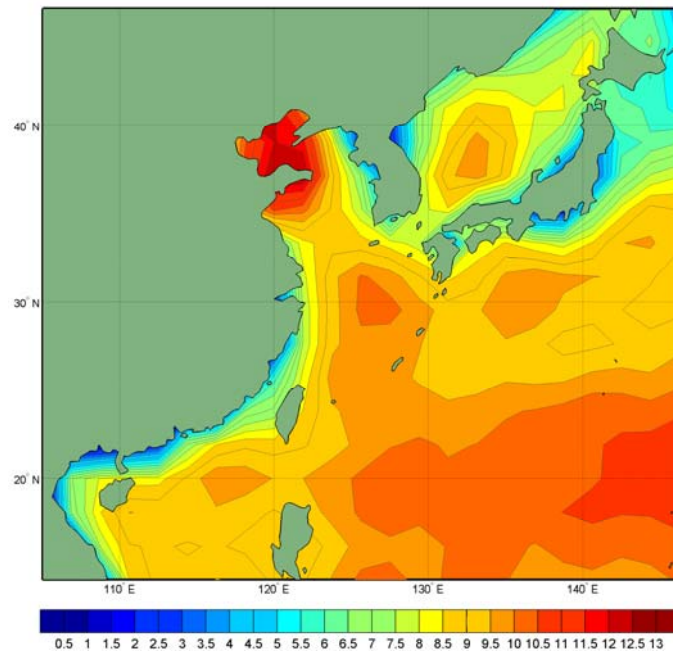


Figure 69. September LTM EDH (m) for the WNP AOI.

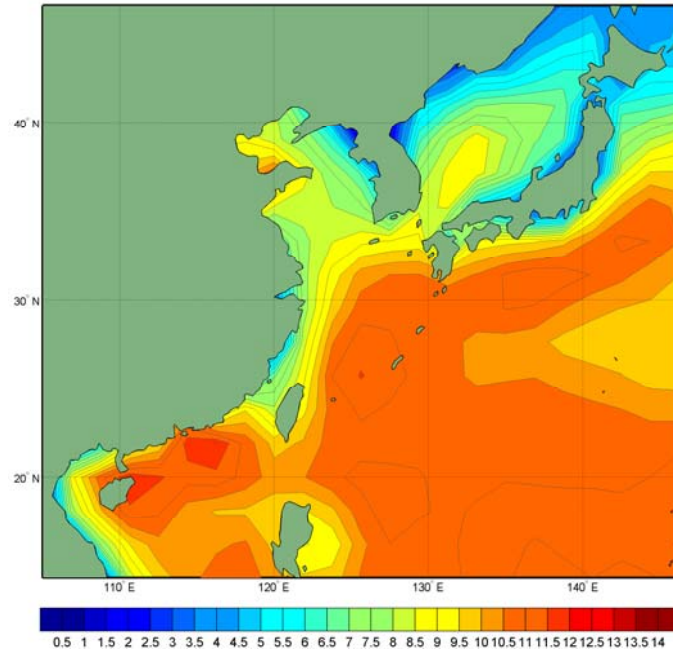


Figure 70. November LTM EDH (m) for the WNP AOI.

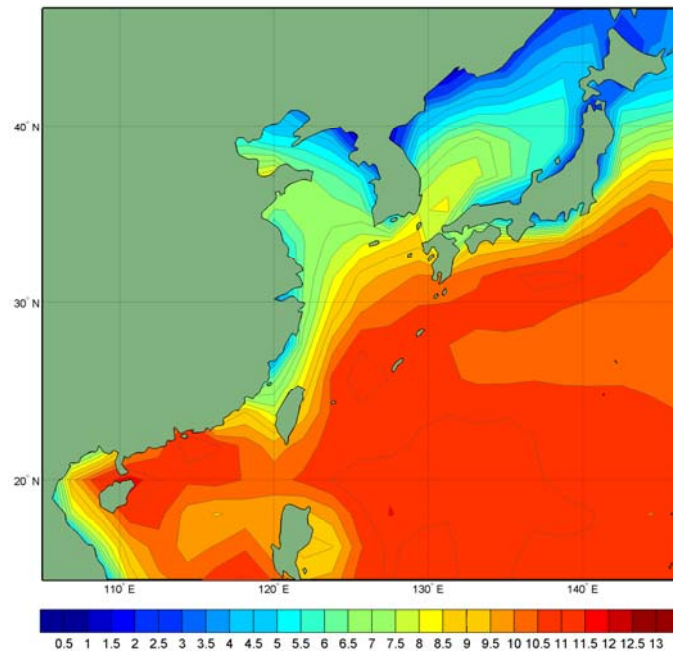


Figure 71. December LTM EDH (m) for the WNP AOI.

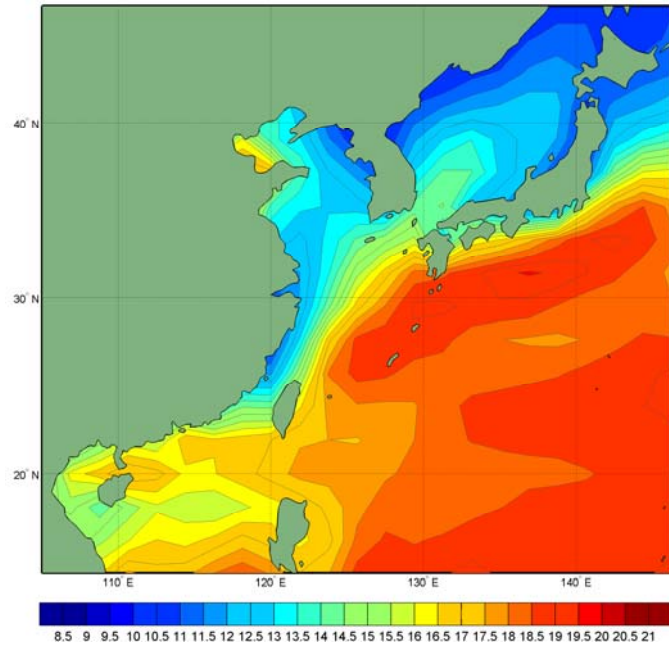


Figure 72. February LTM RDR (nmi) for WNP AOI.

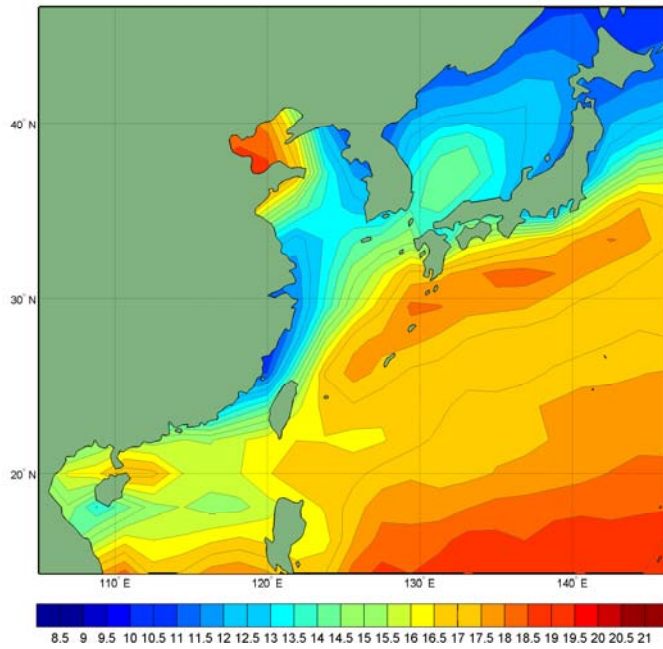


Figure 73. March LTM RDR (nmi) for WNP AOI.

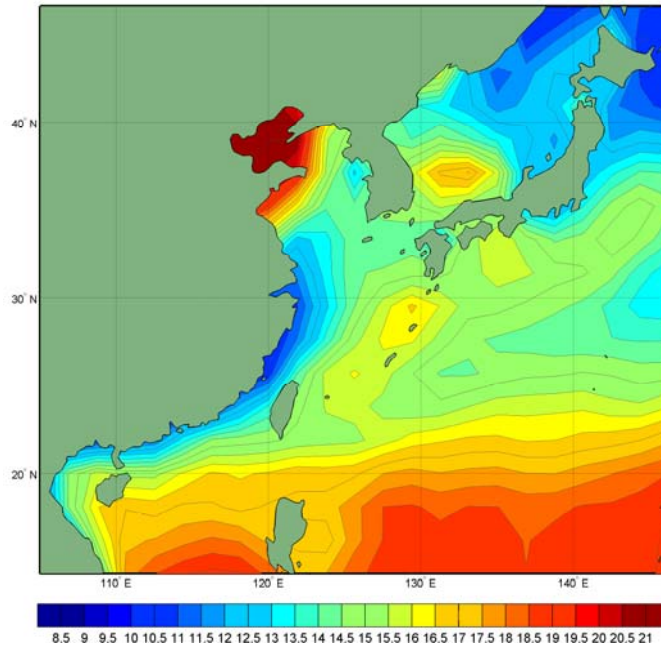


Figure 74. May LTM RDR (nmi) for WNP AOI.

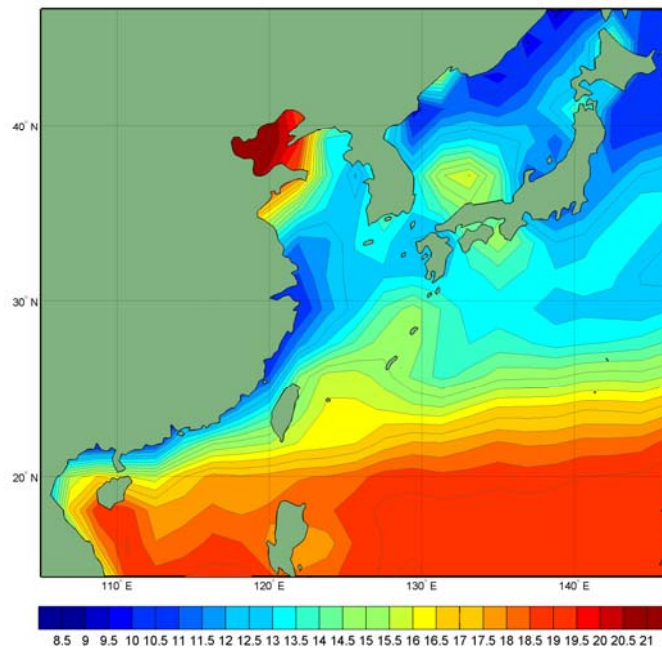


Figure 75. June LTM RDR (nmi) for WNP AOI.

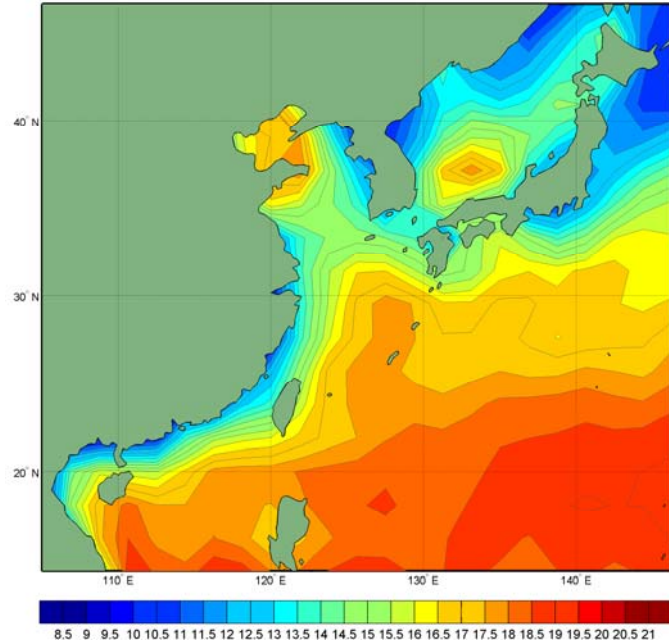


Figure 76. August LTM RDR (nmi) for WNP AOI.

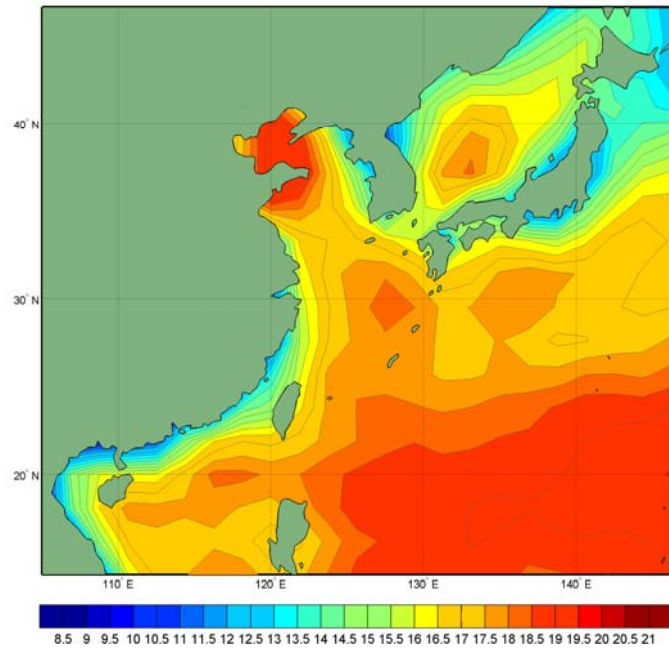


Figure 77. September LTM RDR (nmi) for WNP AOI.

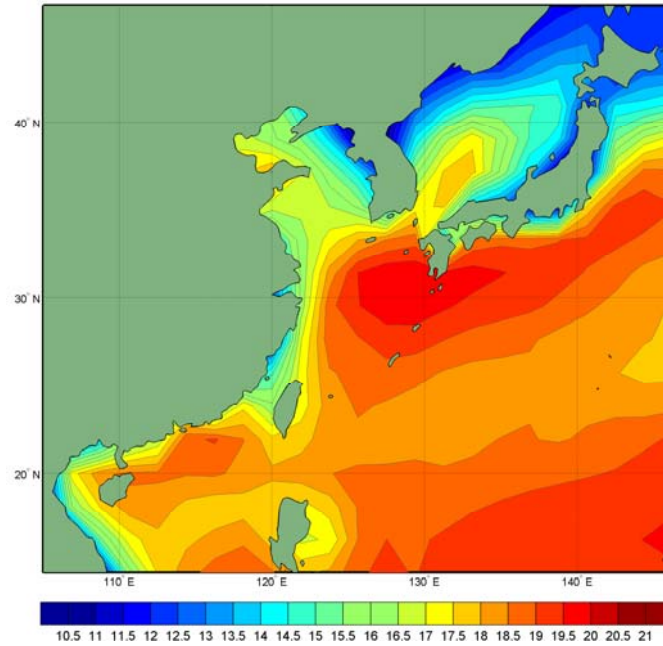


Figure 78. November LTM RDR (nmi) for WNP AOI.

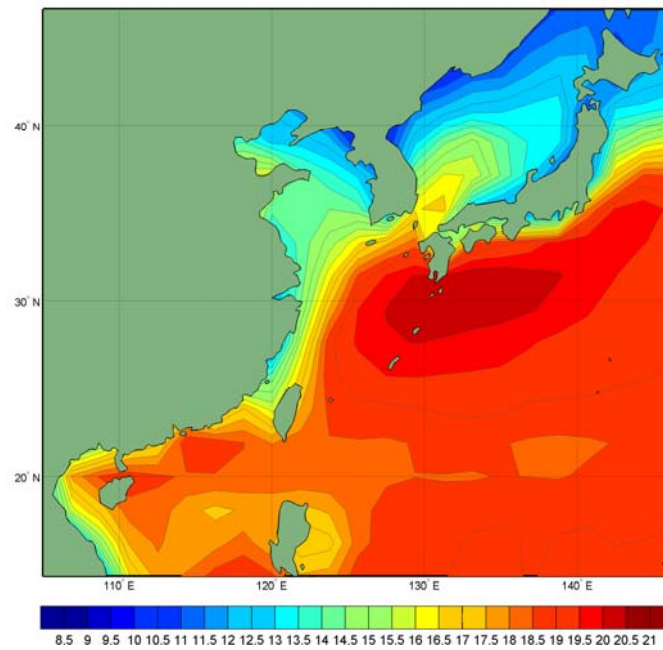


Figure 79. December LTM RDR (nmi) for WNP AOI.

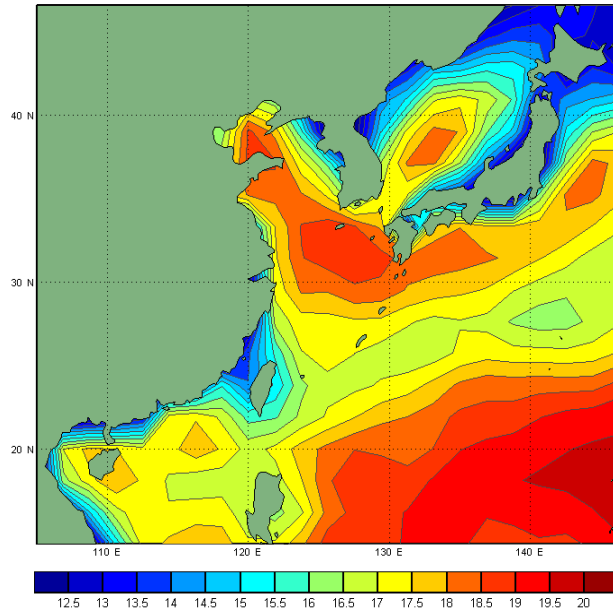


Figure 80. October conditional composite based on the five shortest RDR years of a generic radar.

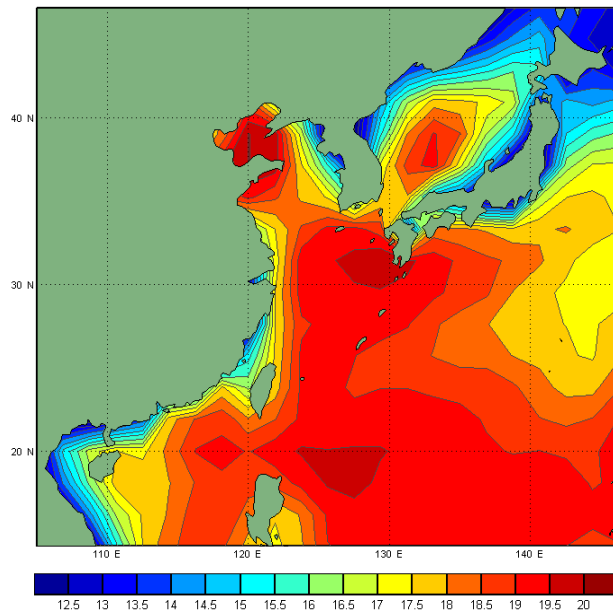


Figure 81. October conditional composite based on the five longest RDR years of a generic radar.

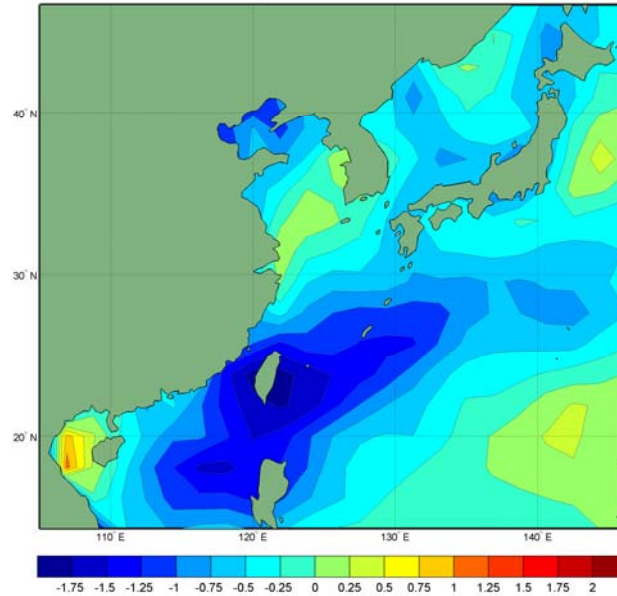


Figure 82. October conditional anomaly based on the five shortest RDR years of a generic radar.

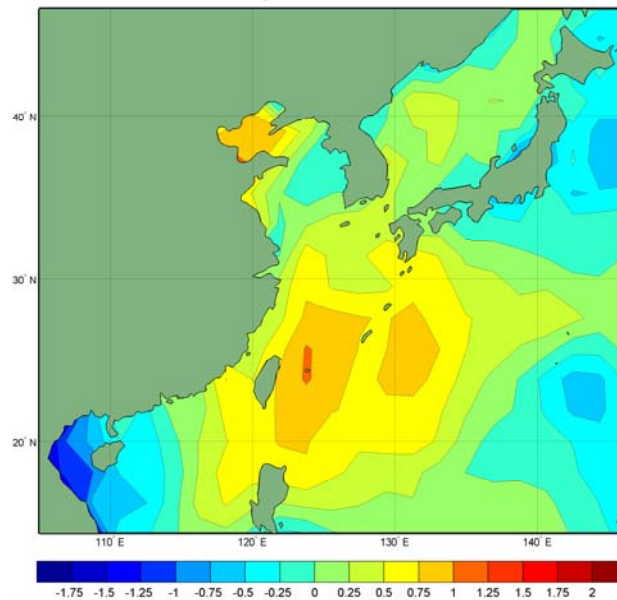


Figure 83. October conditional anomaly based on the five longest RDR years of a generic radar.

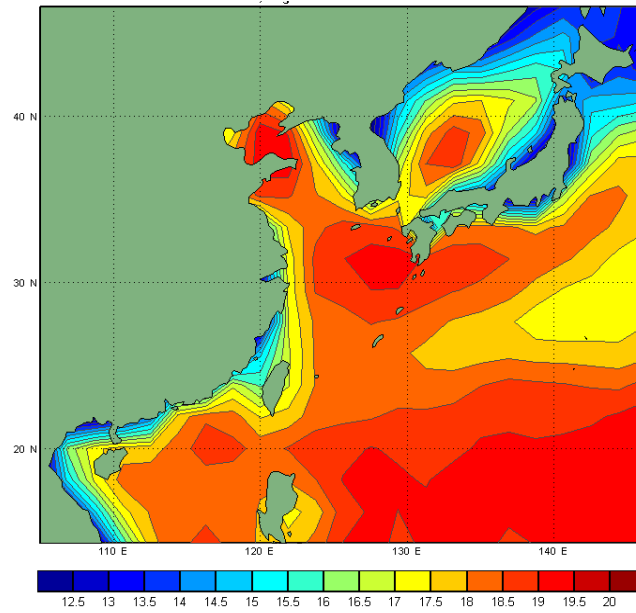


Figure 84. October LTM of RDR (nmi) for a generic radar.

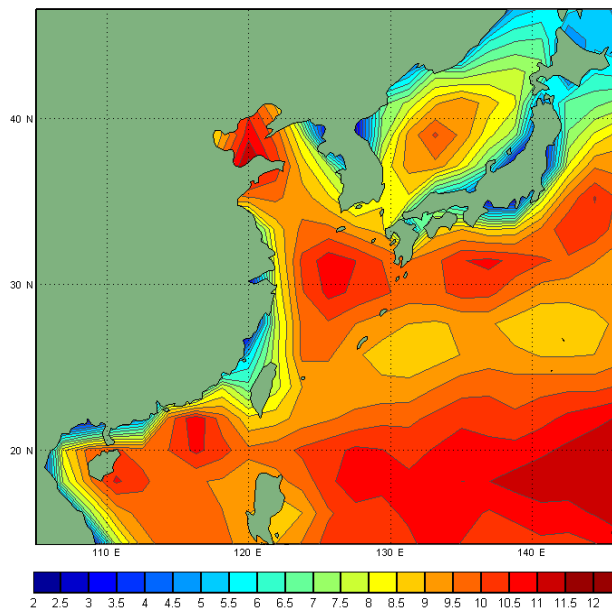


Figure 85. October conditional composite based on the five lowest EDH years.

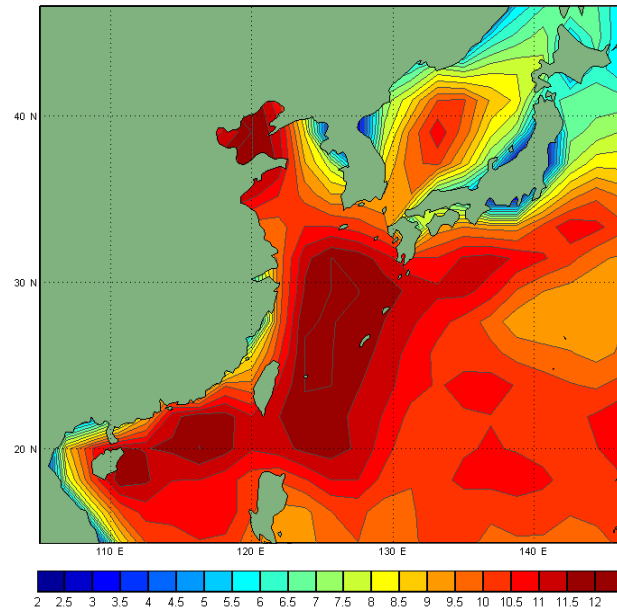


Figure 86. October conditional composite based on the five highest EDH years.

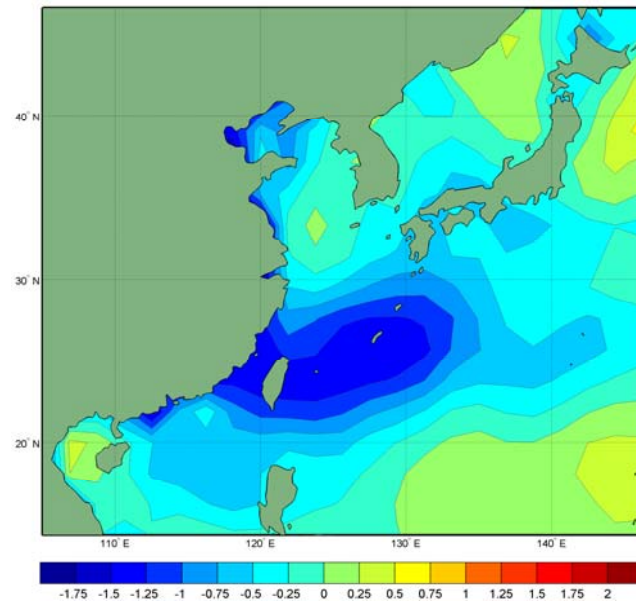


Figure 87. October conditional anomaly based on the five lowest EDH years.

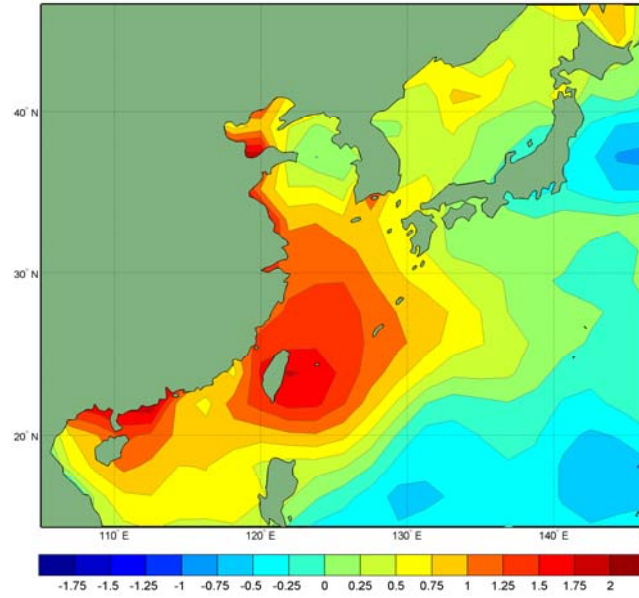


Figure 88. October conditional anomaly based on the five highest EDH years.

THIS PAGE INTENTIONALLY LEFT BLANK

LIST OF REFERENCES

- Babin, S. M., G. S. Young, and J. A. Carton, 1997: A new model of the oceanic evaporation duct. *Journal of Applied Meteorology, Boston, MA*, **36**, 193-204.
- Barrios, A. E., W. L. Patterson, 2002: Advanced propagation model (APM) ver 1.3.1 computer software configuration item (CSCI) documents. *SPAWAR Systems Center, San Diego, Tech. Doc. 3145*, 479 pp.
- Bean, B. R., and E. J. Dutton, 1968: *Radio Meteorology*. Dover Publications, New York, 435 pp.
- Bjerkness, J., 1966: A possible response of the atmospheric Hadley circulation to equatorial anomalies of ocean temperature. *Tellus*, **18**, 820-829.
- . 1969: Atmospheric teleconnections from the equatorial Pacific. *Mon. Wea. Rev.*, **97**, 163-172.
- . 1972: Large-scale atmospheric response to the 1964-1965 Pacific equatorial warming. *J. Phys. Oceanogr.*, **2**, 212-217.
- Finley, J. P., 1884: Tornado predictions. *Amer. Meteor. J.*, **1**, 85–88.
- Ford, B. W., 2000: El Nino and La Nina effects on tropical cyclones: the mechanisms. M. S. thesis, Dept. of Meteorology, Naval Postgraduate School, 190 pp.
- Frederickson, P. A., K. L. Davidson, and A. K. Gorocho, 2000: *Operational bulk evaporation duct model for MORIAH*, Version 1.2. Naval Postgraduate School, 70 pp. (Available from P. A. Frederickson, Naval Postgraduate School, 589 Dyer Road, Monterey, CA 93943-5114).
- Frederickson, P. A., and K. L. Davidson, 2008: *Operational bulk evaporation duct model*. Naval Postgraduate School, 55 pp. (Available from P. A. Frederickson, Naval Postgraduate School, 589 Dyer Road, Monterey, CA 93943-5114).
- Frederickson, P., and T. Murphree, 2008: "A Modern Global Evaporation Duct Climatology," *RADAR Conference*, Adelaide, South Australia, 04 September 2008.

- Hanson, C. M., 2007: *Long-range operational military forecasts for Iraq*. Master's thesis, Dept. of Meteorology, Naval Postgraduate School, Monterey, California, 59 pp.
- Heidt, S., 2009: Long-range atmosphere-ocean forecasting in support of USW operations in the western North Pacific. Master's thesis, Dept. of Meteorology, Naval Postgraduate School, Monterey, California.
- Hendon, H. H., and M. L. Salby, 1994: The life cycle of the Madden and Julian oscillation. *J. Atmos. Sci.*, **51**, 2225–2237.
- Kalnay, E., M. Kanamitsu, R. Kistler, W. Collins, D. Deaven, L. Gandin, M. Iredell, S. Saha, G. White, J. Woollen, Y. Zhu, A. Leetmaa, R. Reynolds, M. Chelliah, W. Ebisuzaki, W. Higgins, J. Janowiak, K. Mo, C. Ropelewski, J. Wang, R. Jenne, and D. Joseph, 1996: The NCEP/NCAR 40-year Reanalysis Project. *Bull. Amer. Meteor. Soc.*, **77**, 437-471.
- Kistler, R., E. Kalnay, W. Collins, S. Saha, G. White, J. White, J. Woollen, M. Chelliah, W. Ebisuzaki, M. Kannamitsu, V. Kousky, H. van den Dool, R. Jenne, and M. Fiorino, 2001: The NCEP/NCAR 50-year Reanalysis: Monthlymeans CD-ROM and documentation. *Bull. Amer. Meteor. Soc.*, **82**, 247-267.
- LaJoie, M., 2006: *The impact of climate variations on military operations in the Horn of Africa*. Master's. thesis, Dept. of Meteorology, Naval Postgraduate School, Monterey, California, 131 pp.
- Mathworks, 2008: MATLAB 7.7, The MathWorks, Inc.
- Molg, T., M. Renold, M. Vuille, N. J. Cullen, T. F. Stocker, and G. Kaser, 2006: Indian Ocean zonal mode activity in a multicentury-integration of a coupled AOGCM consistent with climate proxy data, *Geophys. Res. Lett.*, doi:10.1029/2006GL026384, in press.
- Montgomery, C., 2008: Climate variations in tropical West Africa and their implications for military planners. Master's thesis, Dept. of Meteorology, Naval Postgraduate School, 89 pp.
- Moss, S. M., 2007: Long-range operational military forecasts for Afghanistan. Department of Meteorology, Naval Postgraduate School, Monterey, California. 77pp.
- Mundhenk, B. D., 2009: A statistical-dynamical approach to intraseasonal prediction of tropical cyclogenesis in the western North Pacific. M. S. thesis, Dept. of Meteorology, Naval Postgraduate School, Monterey, California, 107 pp.

- Murphree, T., 2008a: *MR3610 Course Module 6: Smart Climatology*. Department of Meteorology, Naval Postgraduate School, Monterey, California, 52 pp.
- Murphree, T., 2008b: *MR3610 Course Module 19: Madden-Julian Oscillation Part 1*. Department of Meteorology, Naval Postgraduate School, Monterey, California, 32 pp.
- Rasmusson, E. G., and T. H. Carpenter, 1982: Variations in tropical sea surface temperature and surface wind fields associated with the Southern Oscillation/El Nino. *Mon Wea. rev.*, **110**, 354-384.
- Patterson, W. L., 1987: Historical Electromagnetic Propagation Condition Database Description, Naval Oceans Systems Center, San Diego, California. **NOSC TD 1149**.
- Saji, N. H., B. N. Goswami, P. N. Vinayachandran, and T. Yamagata, 1999: A dipole mode in the tropical Indian Ocean. *Nature, London, England*, **401**, 360-363.
- Saji, N. H., T. Yamagata, 2003: Possible impacts of Indian Ocean Dipole mode events on global climate. *Clim.Res.*, **25**, 151-169.
- Schwing, F., T. Murphree, L. deWitt, and P. Green, 2002: The evolution of oceanic and atmospheric anomalies in the northeast Pacific during the El Niño and La Niña events of 1995-2001. *Progress in Oceanography*, **54**, 459-491.
- Tournay, R. C., 2008: Long-range statistical forecasting of Korean summer precipitation. Master's thesis, Dept. of Meteorology, Naval Postgraduate School, Monterey, California, 121pp.
- Turek, A., 2008: Smart climatology applications for undersea warfare. M. S. thesis, Dept. of Meteorology, Naval Postgraduate School, Monterey, California, 95 pp.
- Twigg, K. L., 2007: A smart climatology of evaporation duct height and surface radar propagation in the Indian Ocean. M. S. thesis, Dept. of Meteorology, Naval Postgraduate School, Monterey, California, 135 pp.
- Walker, G., 1924: Correlation in seasonal variations of weather IX: A further weather study of world weather. *Memoirs of the Royal Meteorological Society*, **24**, 275-322.
- Walker, G., and E. Bliss, 1932: World Weather V. *Memoirs of the Royal Meteorological Society*, **4**, 53-84.

- Webster, P. J., A. M. Moore, J. P. Loschnigg, and R. R. Leben, 1999: Coupled ocean-atmosphere dynamics in the Indian Ocean during 1997-98. *Nature, London, England*, **401**, 356-360.
- Wilks, D. S., 2006: *Statistical Methods in the Atmospheric Sciences*. 2nd ed. Academic Press, 627 pp.
- Wolter, K., and M.S. Timlin, 1993: Monitoring ENSO in COADS with a seasonally adjusted principal component index. *Proc. of the 17th Climate Diagnostics Workshop*, Norman, OK, NOAA/N MC/CAC, NSSL, Oklahoma Clim. Survey, CIMMS and the School of Meteor., Univ. of Oklahoma, 52-57.
- Wolter, K., and M. S. Timlin, 1998: Measuring the strength of ENSO events — how does 1997/98 rank? *Weather*, **53**, 315-324.

INITIAL DISTRIBUTION LIST

1. Defense Technical Information Center
Ft. Belvoir, Virginia
2. Dudley Knox Library
Naval Postgraduate School
Monterey, California
3. Dr. Tom Murphree
Meteorology Department, Code MR/Me
Naval Postgraduate School
Monterey, California
4. Mr. Paul Frederickson
Meteorology Department, Code MR/Fd
Naval Postgraduate School
Monterey, California